



# Accelerating 23,000 hours of Ground Test Backsputtered Carbon on a Magnetically Shielded Hall Thruster

Robert B. Lobbia,<sup>\*</sup> James E. Polk,<sup>†</sup> Richard R. Hofer,<sup>‡</sup> and Vernon H. Chaplin<sup>§</sup>

*Jet Propulsion Laboratory, California Institute of Technology, Pasadena, CA 91109*

and

Benjamin A. Jorns<sup>\*\*</sup>

*University of Michigan, Ann Arbor, MI 48109*

As part of an effort to assess the effect of ground-test back-sputtered chamber material during a long duration Hall thruster life test, the Accelerated Carbon Deposition Campaign (ACDC) test was conducted. This 410 hour long accelerated test was specifically devised in preparation for a 23,000 hour qualification test of the HERMeS (Hall Effect Rocket with Magnetic Shielding) thruster in a vacuum chamber (VF-5) lined with graphite where the total back-sputtered carbon anticipated is a 40  $\mu\text{m}$  thick layer. The ACDC back-sputter rate was accelerated by approximately 54 times the nominal VF-5 HERMeS rate by the placement of 1 m by 1 m square panel of graphite 0.5 m downstream from the exit plane of a magnetically shielded Hall thruster, the H6MS, operated at 300 V 6 kW. While dramatic decreases in the ceramic insulating wall surface resistance (3.3 k $\Omega$  to 36  $\Omega$  mean change) and thruster body to anode/cathode/keeper resistances (200 G $\Omega$  to 2.9 M $\Omega$  mean change) were observed, the nominal thruster performance—thrust and efficiency—remained unchanged. Throughout the 0 to 40  $\mu\text{m}$  carbon deposition, the thruster visually darkened (initially white BN walls ended matte black) and discharge oscillations exhibited an amplitude increase of +46%. Relatively frequent (8 events per JPL-hour) “carbon flares” occurred that necessitated the continual operation of the cathode keeper to prevent the thruster from shutting down during some (approximately 2%) of these transients that briefly induced up to more than 375 A of discharge current. This shutdown rate of 1 shutdown every 5.9 JPL-hours corresponds to a predicted shutdown every 14 days during the planned long duration test in the VF-5 facility at the NASA Glenn Research Center. While the nominal 300-V operation of the thruster was unaffected by the 40- $\mu\text{m}$  of back-sputtered carbon, the use of just this a single 300-V thruster discharge voltage throughout the entire deposition test led to intense carbon flaring upon later attempts to throttle to higher voltages. Higher-voltage post-deposition operation was only attempted briefly (<10 seconds) and then abandoned out of concern for the hardware, which may have been fine once the flares subsided. The test was concluded voluntarily once the quartz crystal microbalance (QCM) near the thruster registered 40  $\mu\text{m}$  of back-sputtered carbon.

---

<sup>\*</sup> Engineer, JPL Electric Propulsion Group, Senior Member AIAA, robert.b.lobbia@jpl.nasa.gov.

<sup>†</sup> Principle Engineer, JPL Electric Propulsion Group, Associate Fellow AIAA.

<sup>‡</sup> Group Supervisor, JPL Electric Propulsion Group, Associate Fellow AIAA.

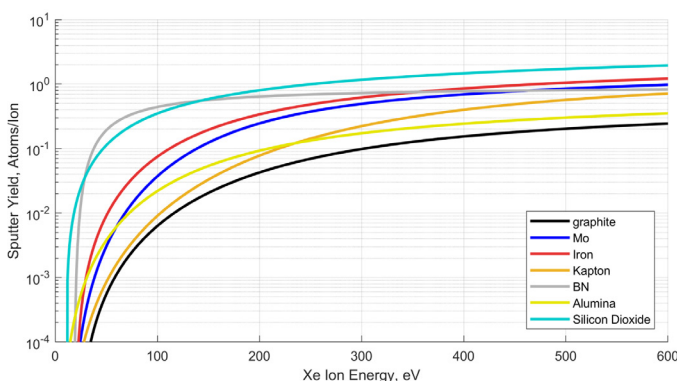
<sup>§</sup> Engineer, JPL Electric Propulsion Group, Member AIAA.

<sup>\*\*</sup> Formerly Engineer in the JPL Electric Propulsion Group, presently Assistant Prof. at Univ. of Michigan, Senior Member AIAA.

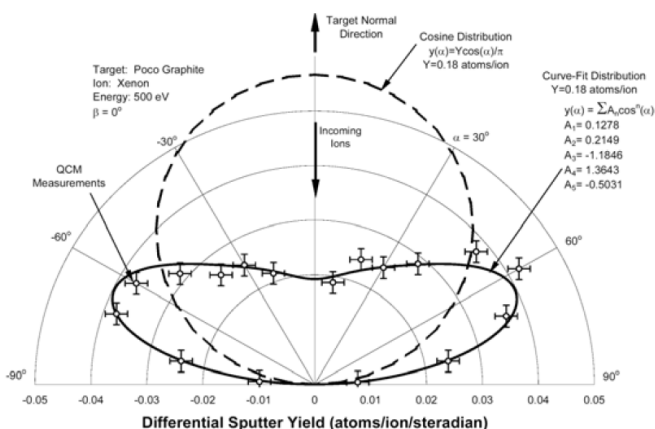
## I. Introduction

LONG duration (>20 kh) ground test campaigns are necessary to qualify the lifetime requirement of electric propulsion thrusters for deep-space missions [1]. However, the ground test environment is an imperfect representation of deep-space differing with: background pressures >3 orders of magnitude higher, a plume fully encased in a conductive walled chamber, and chamber material back sputtering onto the thruster. This later difference has challenged past long duration ion thruster tests [2,3] and is now an issue under investigation for extremely long life magnetically shielded Hall thrusters under development.

The HERMeS thruster in development for future NASA mission represents the first NASA designed Hall thruster to enter flight production. At a 12.5 kW nominal power level, the HERMeS thruster also represents the largest Hall thruster developed for flight. Finally, with magnetic shielding and a mission required lifetime in excess of 23,000 hours, HERMeS will be the longest life Hall thruster designed to date. These technology achievements are enabling for many NASA missions, but as with all major spacecraft components, rigorous ground testing is essential to ensure the thruster is fully qualified for the flight environment and mission requirements. This ACDC test of the H6MS thruster is a central part of the effort to successfully qualify the 12.5 kW HERMeS thruster for flight by ensuring a magnetically shielded thruster can endure a full life-test in a ground test facility. The ground testing of magnetically shielded thrusters is known to coat the thruster discharge channel with back-sputtered carbon from the facility walls [5]. Once a magnetically shielded thruster is coated with back-sputtered carbon most exterior surfaces will be electrically conductive; the impact of this on thruster performance, dynamics, and operational characteristics is not known. Since the current baseline discharge chamber configuration for HERMeS is ceramic and is not conductive, the ACDC test was motivated to understand and assess the effects of back-sputtered carbon in preparation for the long-duration (23,000 h) HERMeS life qualification test.



(a)



(b)

**Figure 1. (a) Sputter yield for various materials using Eckstein and Bohdansky fitted models in target-atoms/Xe<sup>+</sup> ion. (b) Differential sputter yield copied from Ref. [4] for graphite with normal incidence +500 Xe<sup>+</sup> ions.**

performance and behavior was reassessed to quantify any changes.

The first and final phases (0, A, and C) were relatively brief tests (approximately 2 days each) that involved thruster bakeouts and performance measurements at up to three throttle points. Phase B testing was considerably longer spanning from 19-May 2017 through 29-June 2017 (41 days), accumulating a total of 410 hours of thruster operation

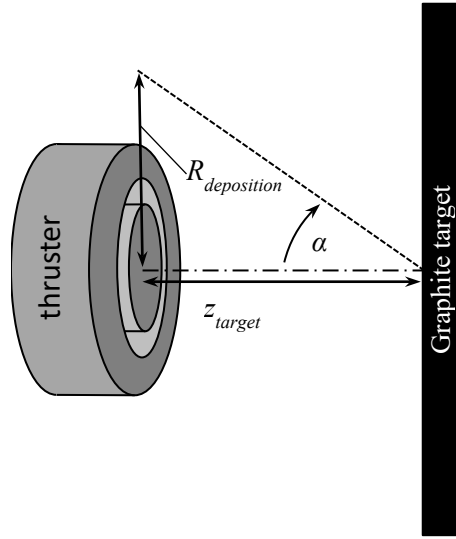
The HERMeS program began with the fabrication and testing of the engineering model TDU (Technology Development Unit) thrusters followed by the protoflight model ETU (Engineering Test Unit) thrusters currently in fabrication by Aerojet Rocketdyne as of July 2019.

## II. Setup and Approach

### A. Accelerated Carbon Deposition Test Sequence

To meet the objectives of this effort, four test phases were conducted beginning with accelerated deposition pathfinding in Phase 0. The H6MS thruster performance and behavior was then baselined in Phase A. The full 40- $\mu$ m of carbon deposition was then completed in Phase B. Finally, in Phase C, the thruster

(42% duty cycle), and 40.1  $\mu\text{m}$  of back-sputtered carbon. The experimental setup for phases A, B, and C was identical except that during phase B, a square 1 m by 1 m graphite target plate was placed 0.5 m downstream of the H6MS exit plane.



### 1. Accelerated Carbon Deposition Pathfinding: ACDC Phase 0

To assess the feasibility of accelerating the carbon back-sputter rate by using a carbon graphite plate downstream of the magnetically shielded H6MS Hall thruster, several pathfinding tests were conducted during ACDC Phase 0. Typically, it is desired to minimize a facility back-sputter rate to create a more flight-like test environment. However, ground testing of electric propulsion devices necessitates a finite back-sputter rate due to the proximity of vacuum facility walls. Graphite is often used to line the facility walls in contact with electric thruster plumes due to its high xenon plasma sputtering resistance as seen in the sputter yield Eckstein and Bohdanky fitted data shown in Figure 1(a) [6,7].

From these sputter yield curves the erosion rate of a target (e.g. beam dump) may be estimated. The placement of a planar graphite target a relatively short distance,  $z_{target2thruster}$ , downstream from the thruster is expected to accelerate the carbon back-sputter received by the thruster as depicted in Figure 2.

**Figure 2. Diagram of proposed back-sputter acceleration configuration.**

To estimate the back-sputter rate seen by a thruster, the angular distribution of these sputtered carbon atoms must be taken into account. Using fits to differential sputter yield data (typical data shown in Figure

1(b)) from Ref. [4], the amount of back-sputtered carbon atoms from a target bombarded by beam current,  $I_{beam}$ , at an energy,  $E_{beam}$ , that is received by the thruster within a known angle of view,  $\alpha$ , of the target center may be estimated.

$$\dot{h}_{deposition} \approx Y_{target-to-thruster}(\alpha, E_{beam}) \cdot I_{beam} \cdot \left[ \frac{FW_c m_n}{e \rho_c A_{deposition}} \right]$$

$$Y_{target-to-thruster}(\alpha, E_{beam}) = 2\pi \int_0^\alpha y(\theta, E_{beam}) \sin(\theta) d\theta \quad (1)$$

$$y(\theta, E_{beam}) = Y_{total}(E_{beam}) \cos(\theta) / \pi, \quad \text{cosine sputter distribution}$$

$$y(\theta, E_{beam}) = \sum_{n=1}^5 A_n \cos^n(\theta), \quad \text{experimentally fit sputter distribution [4]}$$

The back-sputter rate,  $\dot{h}_{deposition}$ , in Eq. (1) has been converted to meters of carbon per second using the target material properties (density,  $\rho_c$ , atomic mass,  $FW_c$ , neutron mass,  $m_n$ , and electron charge,  $e$ ) and the area including the thruster face and QCM that are within  $\pm\alpha = \pm \text{atan}(R_{deposition}/z_{target})$  receiving the deposition,  $A_{deposition} = \pi R_{deposition}^2$ .

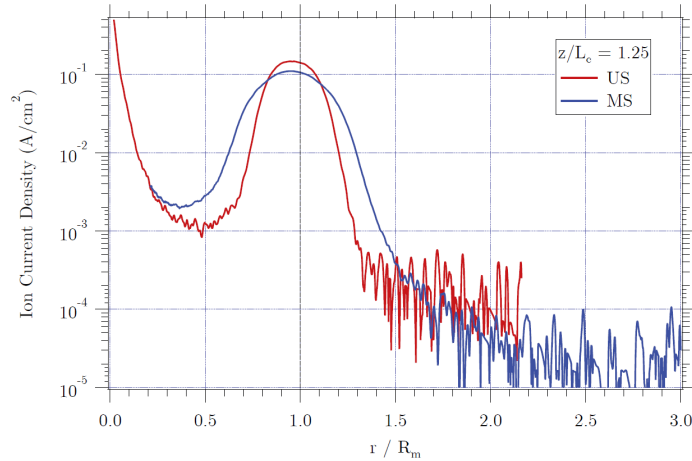


**Figure 3. Near-field ion current density data for 300-V 20-A H6MS (blue trace) from Ref. [8], collected approximately 1 cm downstream of the thruster exit plane.**

$$\dot{h}_{deposition-theory} \approx 97.6 \mu\text{m}/\text{kh}, \text{ 300-V 20-A H6MS with 0.5-m target distance} \quad (2)$$

**Table 1. Theoretical and Experimental back-sputter rates for H6MS operation from 1.5 kW to 9 kW with carbon targets 0.5 m, 1.2 m, and (nominal Owens chamber) 5.3 m downstream.**

In ACDC test Phase 0, a 1-m by 1-m graphite target was placed at several locations downstream and the back-sputter rates measured using a QCM near the thruster. These data (theory vs. experiment, Figure 4 and Table 1) successfully validated the method of back-sputter acceleration and showed the expected linear relation to discharge power.

Z <sub>target</sub> (m)	Discharge Power (kW)	Theoretical Back-sputter ( $\mu\text{m}/\text{kh}$ )	Experimental Back-sputter ( $\mu\text{m}/\text{kh}$ )	Difference (%)
0.5	1.5	24.4	18.3	25.0%
0.5	3.0	48.8	44.6	8.6%
0.5	4.5	73.2	73.1	0.1%
0.5	6.0	97.6	96.5	1.1%
1.2	1.5	6.67	6.60	0.9%
1.2	3.0	13.3	13.4	-0.5%
1.2	4.5	20.0	20.2	-1.1%
1.2	6.0	26.7	26.7	-0.2%
1.2	9.0	40.0	44.5	-11.2%
5.3	6.0	1.45	0.91	36.7%
5.3	9.0	2.17	2.40	-10.7%
<b>Average  Diff.:</b>				<b>8.7%</b>

Using H6MS near-field Faraday probe data from Ref. [8] (shown in Figure 3) for  $I_{beam}=17.4$  A, the fitted differential sputter yield coefficients for 300-V normal incidence ( $A_1$  to  $A_5 = -0.0051395$  0.33484 -1.0821 1.2623 -0.498 atoms/ion), and  $R_{deposition} = 0.45$  m, the back-sputter rate was estimated using Eq. (1):

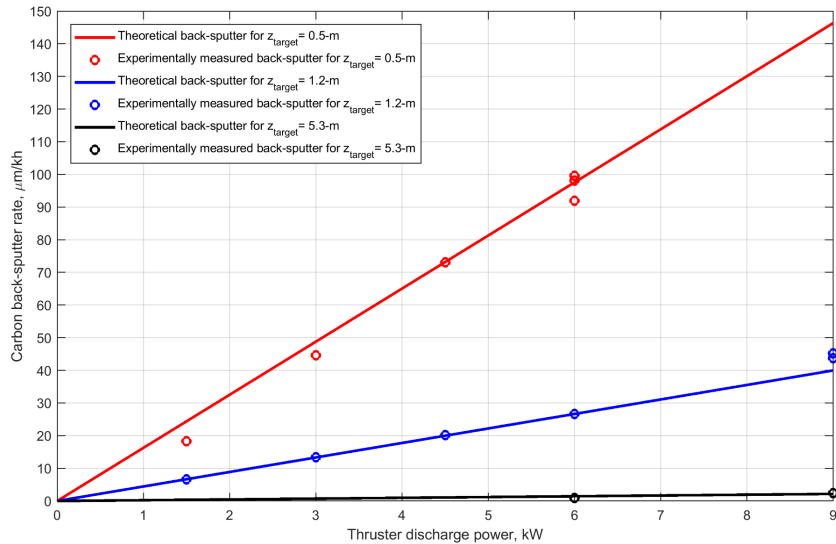


**Figure 4. Theoretical (lines) and experimental (circles) back-sputter rates for the H6MS in Figure 2 configuration, with  $z_{\text{target}} = 0.5$  m (red), 1.2 m (blue), and 5.3 m (black). The nominal JPL Owens facility beam dump is located 5.3 m downstream.**

radiate up to about  $\sim 170$  W to the thruster. Actual observations during ACDC Phase B match these predictions with an average 0.5 m downstream target average steady-state temperature of  $384^\circ\text{C}$  for H6MS operation at 6 kW.

## 2. Thruster Baseline Performance: ACDC Phase A

While the operational characteristics and performance of the H6MS have been assessed in prior works [8], it was deemed necessary to obtain a new set of measurements using the specific ACDC test setup and diagnostics to facilitate a tightly controlled experimental set of data before and after the planned  $40\ \mu\text{m}$  of carbon deposition. The full list of diagnostics acquired in Phase A is provided in Section II.G. The setup of this phase is also detailed in Section II.E and it comprises the standard configuration for typical Hall thruster ground testing in the JPL Owens facility. The carbon panel, when located at 0.5 m during Phase B, was observed to increase the thrust by about 2.5%, visually alter the plume profile, increase the thruster temperature by  $\sim 10\%$ , and increase oscillations by 70.5%. Conditions fully characterized during Phase A included 300V 6kW, 300V 9kW, and 600V 9kW. Prior to characterization measurements of thrust and other telemetry, the thruster was fully baked out and operated for  $\geq 2$  hours at full power (6 kW).

## 3. Thruster Deposition of $40\ \mu\text{m-C}$ : ACDC Phase B

The ACDC Phase B involved the operation of the thruster at the optimized back-sputter accelerated configuration until the full  $40\ \mu\text{m}$  of back-sputtered carbon was recorded by the QCM. The ACDC Pathfinding Phase 0 helped identify that higher discharge powers (6 kW and 9 kW) and a closer graphite target location led to maximum back-sputter rates. A fixed graphite target location 0.5 m downstream was selected for the Phase B deposition. At the beginning of Phase B, both 6 kW and 9 kW operation of the H6MS was conducted to determine the highest power throttle point that the thruster, test setup, and facility could maintain in a stable manner. Higher power and higher voltage operation had the benefit of a more rapid Phase B deposition time as well as reduced xenon consumption. While the H6MS had been successfully operated at steady state for over 113 hours at 9 kW (800 V 11.25 A) in prior efforts [5], the close proximity of the graphite target 0.5 m downstream from the thruster was expected to add additional thermal loading to the cryogenic pumping system, thruster, and test setup. During the first hour of Phase B operation at 9 kW, the center of the graphite target 0.5 m downstream was glowing bright red at  $>736^\circ\text{C}$  (and was rising at  $17^\circ\text{C}/\text{hour}$ ) when the thruster body current blew a DMM fuse (which was rapidly repaired), disrupted digital communication to the several instruments in the setup, and ultimately led to the 1<sup>st</sup> unexpected shutdown of the ACDC testing.

Since the graphite target support structure was built from 6105-T5 aluminum 80/20 components that have a melting temperature of  $\approx 624^\circ\text{C}$ , and due to the larger electromagnetic spikes and instrument pickup/sensitivity associated with

This simplified model agreed remarkably well (average difference of 8.7%) with the experimental data which demonstrated up to a 106x increased back-sputter rate (target 0.5 m downstream) compared to the base rate of the JPL Owens facility (beam dump 5.3 m downstream). The back-sputter rate could have likely been increased further by moving the target closer than 0.5 m, however concern regarding thermal effects (plate radiating thermally back to thruster), plume perturbation effects, and deposition non-uniformity effects limited the target distance to 0.5 m. At this location, the graphite target was predicted (using the Stefan–Boltzmann law) with a 6 kW discharge to reach an average temperature of  $358^\circ\text{C}$  and back-

higher voltage operation, the 600 V 9 kW operation was abandoned and Phase B continued with only 300 V 6 kW. This decision helped guarantee thermal and electrical stability of the setup at the minor expense of a slightly longer test campaign.

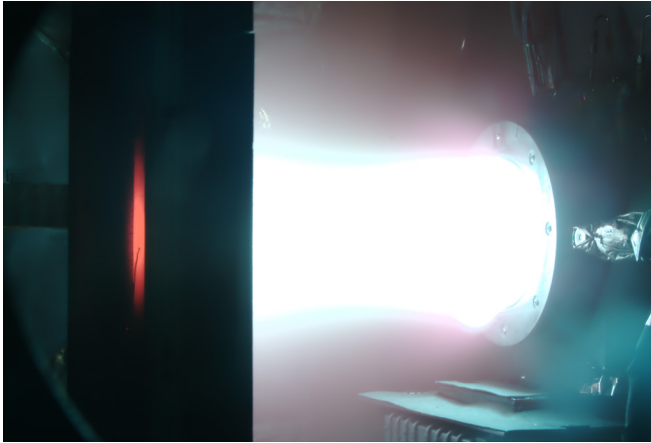


**Figure 5. Glowing red graphite target panel blasted by 600 V 9 kW H6MS discharge on 25-May-2018 (50 mm, f/10, 2 s, ISO-200 exposure).**

#### 4. Thruster Re-baseline Performance: ACDC Phase C

After the deposition of the 40  $\mu\text{m}$  carbon back-sputter upon the H6MS, the facility was returned to atmospheric pressure briefly for the removal of graphite target and re-pumped down to high-vacuum for one final performance characterization test. The presence of the graphite panel perturbs the plume, causes increased thrust, and increases oscillation dynamics, thus removal enables nominal H6MS operation with the exact setup used in ACDC Phase A. Any changes then observed between Phase A and C data are directly attributed to the 40  $\mu\text{m}$  carbon back-sputtered layer.

### B. H6MS Thruster

The H6MS thruster is a magnetically shielded version of the H6 a 6 kW laboratory Hall thruster created to conduct studies investigating fundamental Hall thruster discharge physics. The H6 thruster was the product of joint design and testing efforts by JPL, The University of Michigan, and the Air Force Research Laboratory with three units originally fabricated in 2007 [9]. The magnetically shielded version of the H6 was developed [8] with several design modifications based on modeling and simulation results from JPL Hall2De physics based thruster plasma modeling tool [10]. The H6MS nominal performance at 300 V and 6 kW is 62.4% total efficiency, 2000 s specific impulse, 384 mN thrust, and a lifetime limited only by the cathode selection (>100,000 h possible [11]) and pole cover thickness (>50,000 h possible with 10 mm thick graphite covers [12]). A short duration, 113 h, wear test had already been conducted with the H6MS [5], as well as a test with graphite wall covers [13]. These heritage efforts provided confidence that the longer duration ACDC H6MS test was unlikely to experience unexpected operational issues.

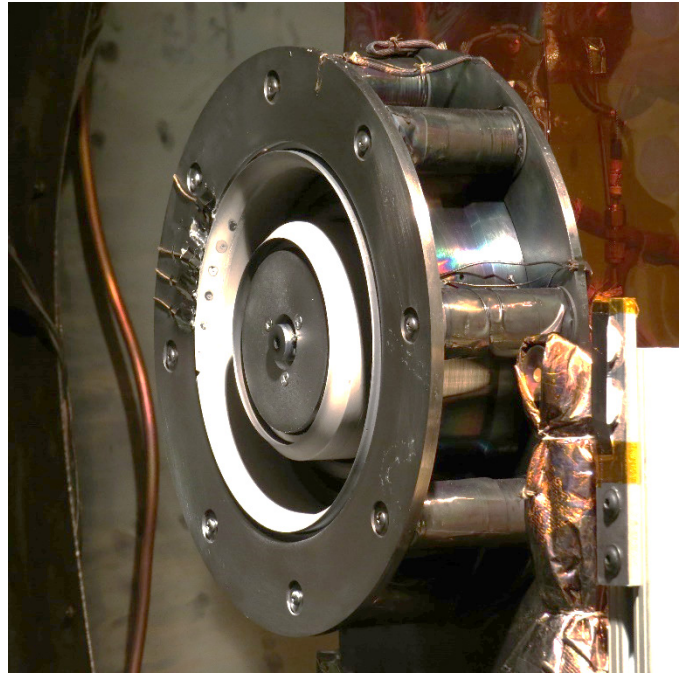


**Figure 6. Photograph of H6MS with in-situ wall probes prior to start of ACDC Phase 0 testing, Oct 2016.**

The H6MS has removable rings on the outer sections of the inner and outer discharge channel walls (nearest the exit plane) that leave physical gaps between the discharge chamber and rings. The HEMReS TDU thruster chamber, however, has one continuous piece of ceramic. There was a possibility that these physical gaps would prevent a continuous conductive layer from forming during carbon deposition. In order to better approximate the TDU configuration, Ceramabond© was used to bridge the gaps between ceramic pieces and then—after 48 h of air curing—

sanded flush with discharge chamber surfaces. The remaining accessible exposed surfaces (e.g. not covered by the anode) of the discharge channel walls were also lightly cleaned abrasively with scotch-bright pads to remove most pre-existing carbon deposition.

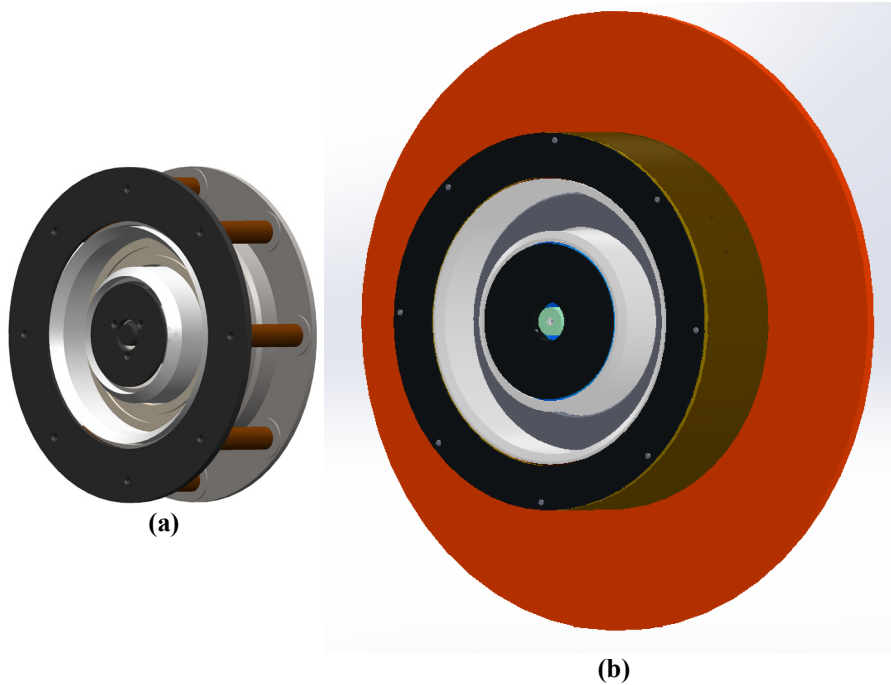


**Figure 7. Angled views of the (a) H6MS and (b) TDU CAD models.**

thruster body is electrically isolated using 12 insulating plastic washers on the rear spool mount mating plate. The location of these insulating washers behind the TDU radiator provides shadow-shielding from most of the downstream facility carbon back-sputter sources.

### C. H6MS vs. HEMReS channel geometry

The H6MS possesses other similarities to the TDU and ETU thrusters aside from magnetic shielding. Both thrusters employ ceramic discharge channel walls: boron nitride for the H6MS and borosilicate for both TDU-2 and ETU-1. Prior to the advent of magnetic shielding, Hall thruster plasma-wall interactions led to the use of insulating materials with low secondary electron emission coefficients [14], to obtain high efficiency performance and stability. Magnetic shielding in Hall thrusters pushes the plasma away from the walls and lessens wall interactions considerably, to the extent that discharge channel wall material selection is less restrictive, enabling efficient thruster designs with metallic and conducting discharge channel walls [13,15]. Based on these prior efforts, the conductive state of the discharge channel walls was not deemed to pose a risk to thruster operation throughout the ACDC testing. The H6MS and HERMeS thrusters both utilize ceramic walls and the plasma contacting gaps (illustrated in Figure 8) of relevance are all similar in magnitude. Both the H6MS and HERMeS designs shadow-shield the base of the anode to discharge channel interface to eliminate line-of-sight from the ionization zone to this region. This should result in minimal carbon back-sputter deposition at this region, potentially maintaining electrical isolation even while the remaining portions of the channel walls are coated with a facility back-sputtered conductive layer of carbon. However, it is still possible for larger flakes of carbon to spall off from other portions of the thruster and bridge the anode to channel wall gaps. The other—and more potentially problematic gaps—are the areas between the outside edges of the discharge channel walls and the magnetic field components of the thruster body. Both the H6MS, TDU, and ETU designs have similarly sized gaps between the channel and the body of the thruster, but the TDU and ETU designs add shadow-shielding of the surfaces below interface. The entire H6MS discharge channel interface with the thruster body has direct line-of-sight to the plasma plume and facility and is expected to receive more carbon back-sputter during the ACDC test than the HEMReS thruster would experience during a 23,000 h qualification test. In this manner, the ACDC test with the H6MS offers a worst-case scenario for studying the effects of carbon back-sputter from long-duration ground testing.

For all phases of ACDC testing, the thruster was mounted to a thrust stand and the thruster body and mounting bracket were electrically tied to the cathode common which was isolated from the grounded vacuum facility walls. A thin sheet of mica between the base of the thruster mounting bracket and the thrust stand mounting stem provided this electrical isolation. A careful attempt to fully shadow-shield this interface with Kapton® sheets was made during the setup of the thruster to limit the back-sputtered carbon that might have otherwise shorted the H6MS thruster body to facility ground. In the HERMeS TDU design, the

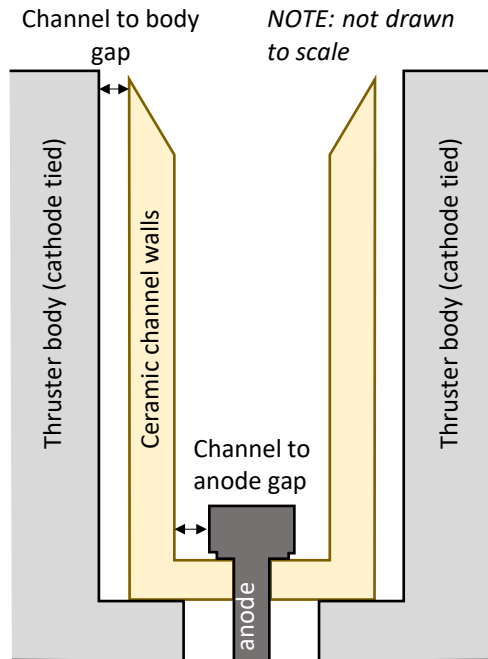


**Figure 8. Layout (not drawn to scale) of H6MS discharge channel cross sectional view. The noted gaps are all similar in magnitude for the H6MS, TDU-2, and ETU thrusters, but the design details are different.**

Experiments with magnetically shielded thrusters have yielded wall potential measurements that hover  $\approx 1 \times T_e$  (electron temperature in eV) within the anode potential [8,16]. If the channels walls become conductive (e.g. via carbon deposition), then the entire ceramic channel wall is effectively at anode potential. Thus, isolation between the anode and the discharge channel is relatively unimportant (since they are nearly the same voltage in operation). However, the isolation between the discharge channel and the thruster body is critically important because the thruster bodies are both electrically tied to the cathode potential and these gaps maintain the full anode-to-cathode voltage across them in operation. If body to channel walls lost significant electrical isolation (e.g. developed a low-resistance short due to carbon back-sputtered deposition), then power,  $P_{film} = V_{azc}^2 / R_{carbon}$ , would be dissipated through this resistance which could lead to thruster failure from catastrophic localized heating or the inability for the thruster to maintain a plasma discharge. It is also possible that the thruster power supply might be able to clear or clean off this carbon via localized flaring of these carbon buildups.

#### D. Thruster High-Impedance Isolation Testing

It is standard practice to perform high-potential isolation testing of all thruster power cabling upon installation of Hall thrusters to assess both the thruster health and fidelity of the harnessing in the setup. The generation of large amounts of carbon back-sputter was expected to cause a decrease in various isolation resistances throughout the deposition process, thus periodic high-potential isolation testing was conducted throughout all ACDC test phases,

especially after significant events including unexpected shutdowns and test phase transitions.

The technique of high-potential testing involves the use of a high-voltage (e.g. 1,000 V) across two electrical test points (e.g. anode and cathode) and the measurement of the steady-state leakage current between the test points. The ratio of the test voltage to the leakage current is then the isolation resistance at that potential. This method of resistance measurement differs from conventional digital multi-meters (DMMs) in that the test voltage is much higher. For example, the Fluke 87 DMM used for isolation resistance measurements (prior to high-potential testing), employed a test voltage from 450 mV to 1.3 V. The benefit of higher voltage isolation testing is that the resolvable maximum resistance is usually much higher ( $G\Omega$  to  $T\Omega$ ) and that it can be more representative of actual operational conditions. Since the anode to body voltage (in a body tied to cathode configuration) is equal to the full thruster discharge voltage during operation, it makes sense to apply this voltage when measuring the anode to body isolation resistance. High-potential testing also helps identify test points that may be isolated at low voltages but close proximity leads to dielectric breakdown and shorting at higher voltages. For this test campaign, all reported high-potential measurements are acquired with the thruster at high-vacuum ( $\leq 1 \mu\text{torr-Xe}$ ) conditions for consistency.

The high-impedance testing procedure used in the ACDC testing notionally matched that used with the HERMeS TDU-2 thruster except for additional wall probe resistance and isolation measurements. A summary of the high-potential isolation testing procedure is described next. (1) At the facility thruster power feedthrough panel, disconnect all lines that lead to power supplies and sensing circuitry. (2) Using a DMM in calibration, complete the resistance measurements specified by the procedure. Using a calibrated high-potential isolation testing meter, carefully apply (for 1 minute) the specified test voltages specified for each measurement. Caution is taken during the high-potential testing to protect the user (by not handling the connection during testing) and to protect the hardware (by not testing at voltages above those listed for each measurement). (4) After high-potential testing, the DMM measurements are retested since the high-voltage isolation testing occasionally clears minor low-resistance shorts. (5) A precision 6.5 digit DMM with 4-wire resistance measurement capability is then used to conduct wall probe resistance and isolation tests. (6) Finally, all thruster connections to the power supplies and sensing circuits are returned to their normal configuration.

## E. JPL Owens Vacuum Chamber

The JPL Owens test facility (Figure 9) is a 3-m diameter, 10-m long cylindrical vacuum chamber that has been used to conduct the 30 kh life test of the 2.3 kW NSTAR ion thruster [17] as well as Hall thruster testing (HEMReS, XR-5, SPT-140, etc.) at EP power levels up to 20 kW.



Figure 9. JPL Owens vacuum test facility exterior view.

The high-vacuum pumping system utilizes three 48” CVI cryopumps and nine custom LN<sub>2</sub> shrouded “cryosail” [18] plate pumps. The facility base pressure for ACDC testing was  $2\text{-}3 \times 10^{-7}$  torr-Xe and the measured pumping rate was 250,000 liters-Xe/s. Corrected xenon pressure measurements were collected in accordance with the current electric propulsion standard [19] using Stabil-Ion gauges. During 300 V 6 kW H6MS thruster operation, the pressure was  $1.1\text{-}1.5 \times 10^{-5}$  torr-Xe. All downstream chamber surfaces—including the walls, ceiling, floor, and baffled beam dump—are covered with graphite panels (see Figure 10) to reduce the nominal back-sputter rate (during ACDC Phases A and C) for 300-V 6-kW and 600-V 9-kW H6MS operation, to  $0.91 \mu\text{m/kh}$  and  $2.4 \mu\text{m/kh}$  respectively.

The overall layout of ACDC test setup inside the Owens vacuum chamber is summarized in Figure 11.

## F. Thruster Electrical and Flow Configuration

The electric thruster power for this test campaign was provided by standard laboratory power supplies and a discharge filter as shown in Figure 12. Recent TDU-2 12.5 kW Hall thruster experiments with higher and lower effective harness inductance (achieved by adding high-inductance coils or an in-vacuum capacitor respectively) have shown invariance to pole erosion [12], ion acceleration [20], and performance.

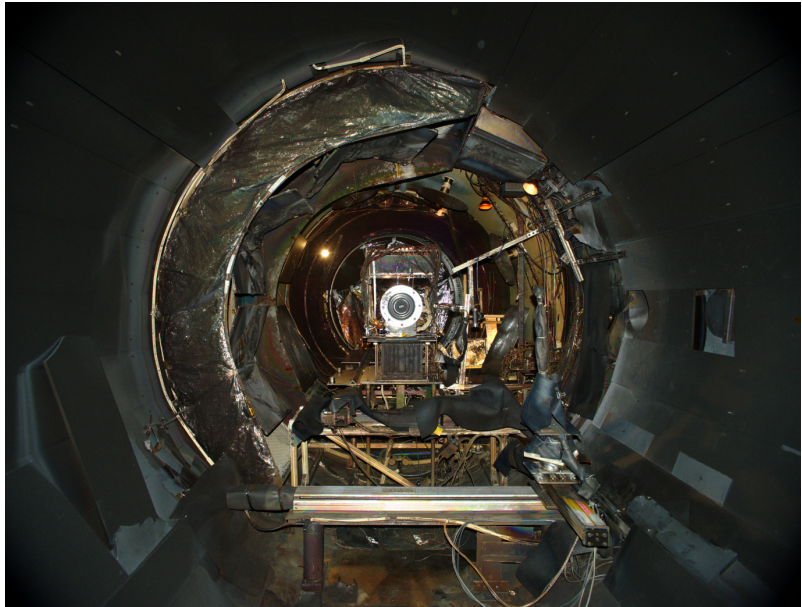
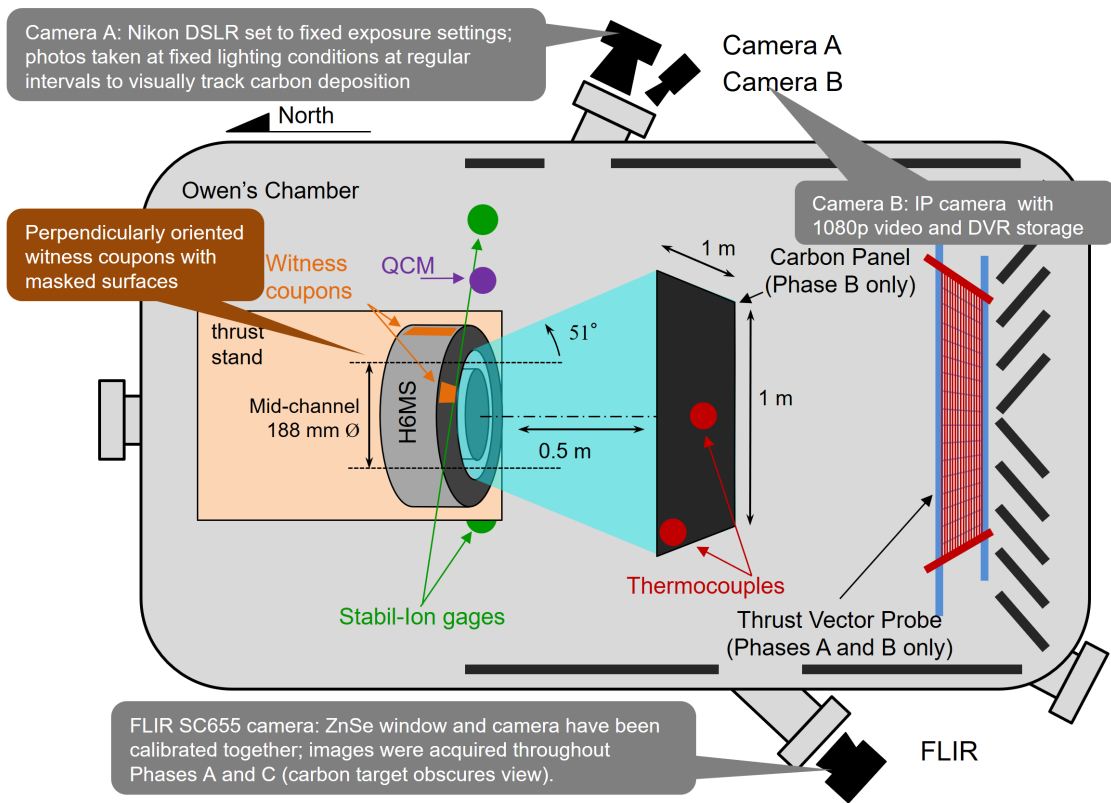
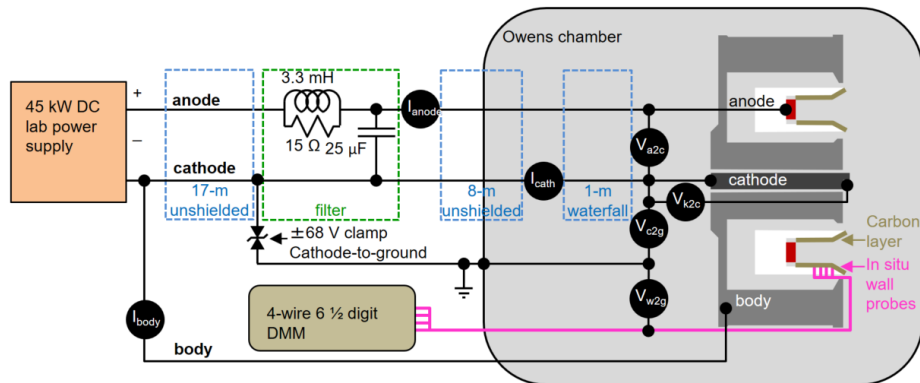


Figure 10. JPL Owens vacuum test facility interior view with H6MS prior to start of ACDC Phase A testing (e.g. before installation of 1 m by 1 m graphite target 0.5 m downstream from thruster).



**Figure 11. Schematic of ACDC test setup with H6MS in Owens chamber and several diagnostics. Phase B setup is shown with carbon blast panel,**

However, for the ACDC testing covered in this report, the optional coils and in-vacuum capacitor were not in use and the nominal 8  $\mu\text{H}$  harness inductance existed. The H6MS was configured in a body-tied to cathode common configuration and high-speed (120 Hz – 20 MHz) discharge current signals were sampled for each of the anode, cathode, and body lines as depicted in Figure 12. The 45-kW DC laboratory power supply for the main discharge was a Magna-Power TSD1000-45 with a maximum output of 1000 V and 45 A. During nominal 300 V 20 A (6 kW) operation of the H6MS, the discharge current limit was set to 30 A and the magnets were set to 4.00-A inner and 3.31-A outer currents.



**Figure 12. Electrical configuration for the operation of H6MS, throughout ACDC testing.**

Flow to the anode and cathode is provided by standard (Brooks and UNIT) mass flow controllers. These flow controllers were calibrated to within  $\pm 1\%$  at the beginning and end of the ACDC test campaign. Propulsion grade xenon (99.9995% pure) propellant was used and point of use purity testing was performed on 19-APR-2016 for the Owens flow system, confirming this purity.

## G. Diagnostics

### 1. Channel Wall Resistance Testing

Spatially resolved discharge channel resistance measurements were performed at the beginning of Phase A (with less than  $0.9 \mu\text{m}$  of carbon deposition) and after the completion of Phase C (after  $40.1 \mu\text{m}$  of carbon deposition). A four probe resistance measurement technique was used to determine the deposited carbon film wall resistance,  $R_w$ , at a series of 16 axially separated points along both the inner and outer discharge channel walls from the anode to the exit plane downstream. These four probes were arranged as shown in Figure 13 and a  $6\frac{1}{2}$  digit DMM (Siglent SDM3065X) was used in 4-wire resistance mode.

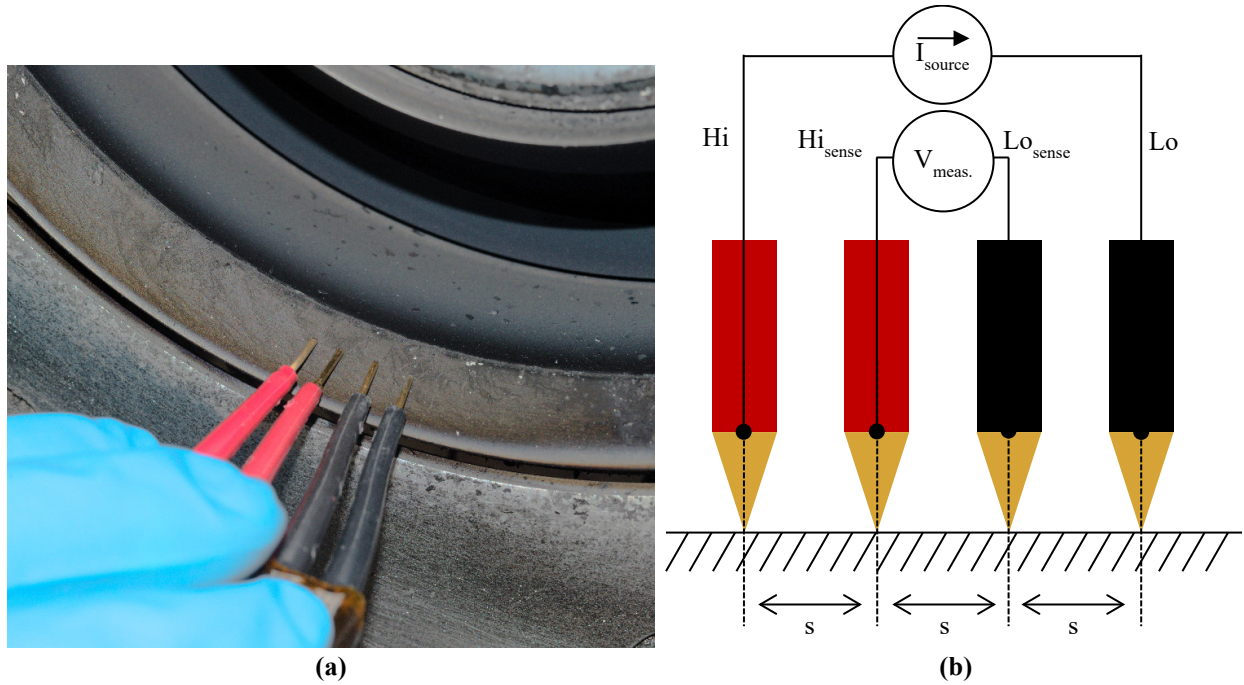


**Figure 13. Four probe measurement (b) of axially resolved back-sputtered carbon film resistance coating the H6MS discharge channel walls (a).**

For probes separated by an equal distance,  $s$ , the differential resistivity may be integrated and simplified for thin films thicknesses,  $t$ , much smaller than the probe separation. Equation (3) presents this theory that assumes a large sheet of constant thickness which is not exactly the case with the ACDC back-sputter deposited carbon film of variable thickness. However, the theory is expected to provide decent approximate agreement with the ACDC test since the carbon film thickness (or effective sheet resistance) varies slowly or even negligibly in the local area of the 4-point probe measurement location.

$$R_w = \frac{\rho_c}{\pi \cdot t} \ln \left( \frac{\sinh(t/s)}{\sinh(t/2s)} \right) \approx \frac{\rho_c \ln(2)}{\pi \cdot t} \text{ for } s \gg t \quad (3)$$

The electrical resistivity of the graphite film,  $\rho_c \approx 700 \mu\Omega\text{-m}$ , deposited on the discharge channel wall is taken as an average of in-plane and out-of-plane graphite resistivity [21].

### 2. In-situ Channel Wall Resistance Diagnostic

In an effort to measure the evolution of the discharge channel wall resistance during the carbon back-sputter deposition, a series of in-situ wall probes were installed on the outer discharge channel as seen in Figure 14.

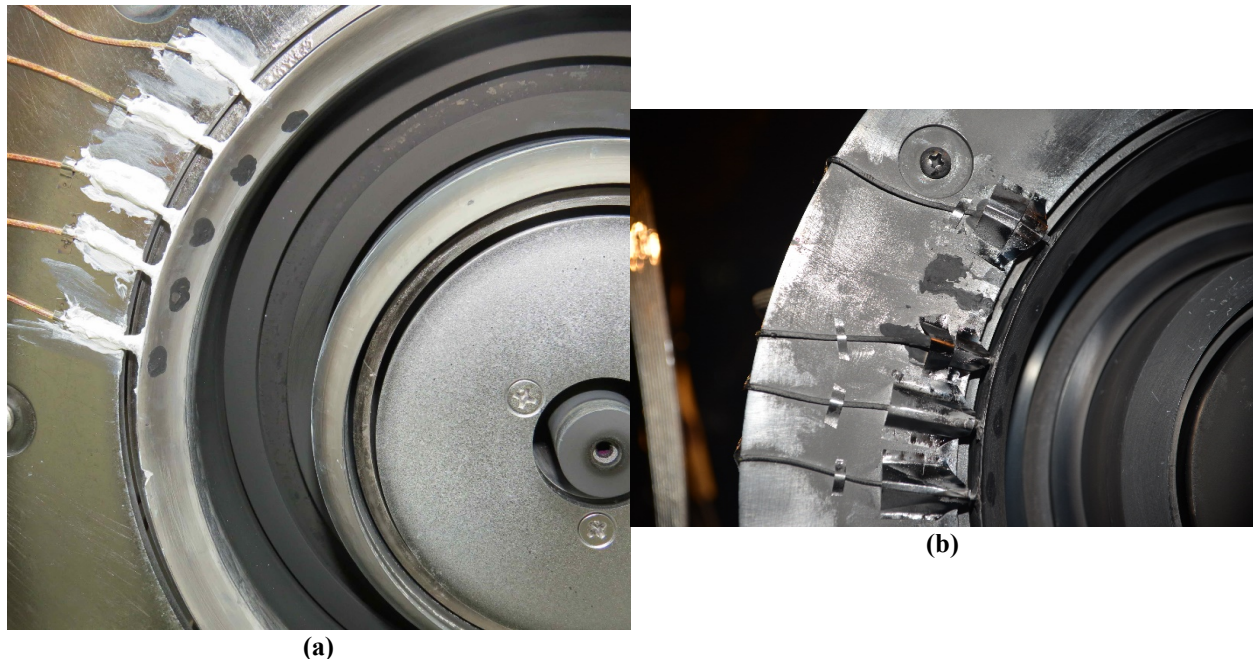


**Figure 14. (a) Five in-situ wall resistance probes were initially mounted to the outer discharge channel of the H6Ms during Phase 0, shown prior to installation of shadow shielding covers over white Ceramabond paste. (b) Photograph of four shadow-shielded in-situ wall probes at the start of Phase A testing.**

The in-situ wall probe electrodes consisted of tungsten rods inserted through the BN ring to be flush with plasma-wetted surface. Probe wires were 18 gauge fiberglass insulated thermocouple (TC) wire with connections that went through a set of high-voltage thrust stand waterfall wires to connection points outside the chamber. Connections from TC wires to the tungsten probes were made via spot welding, then insulated with Ceramabond 690, and finally shadow shielded to prevent unintentional shorting of the discharge channel to the body. In order to make electrical contact with deposited carbon layer, Aquadag (colloidal graphite) was mixed with deionized water using a 1:1 ratio and applied to the probe and surrounding surface area and cured at 100°C for one hour. Conductivity from Aquadag layer to probe tips was verified for each wall probe ( $< 50 \Omega$ ). Five probes were initially installed during Phase 0, but one probe detached, and the remaining four probes were used during Phases A, B, and C. Surface layer conductivity between probes was verified at the start of Phase 0 with two-point probing technique to range from 0.5 M $\Omega$  to 2 M $\Omega$  initially. Four-point probing was subsequently used in testing to measure in-situ back-sputtered film resistance.

### 3. Thrust Stand

An inverted pendulum thrust stand [8,17,22–25] was used during all ACDC test phases to measure the H6MS thrust. A water+glycol chiller supplied coolant flow to the thrust stand copper wall plates to maintain the thrust stand temperature at 20°C  $\pm$  0.1°C. The thrust stand was operated in displacement mode with the thrust directly proportional to the displacement of a linear variable differential transformer (LVDT) sensor. LabVIEW was used to apply closed loop control of the thrust stand inclination angle and active damping was applied with an SRS SIM960 controller using the LVDT signal and an electromagnetic damper coil. Thrust stand calibrations were performed after thrust measurements by lowering known masses with a motorized pulley system. All thruster power cabling, TCs, and propellant flow lines are coupled to the thruster with highly flexible arrangements to maintain a linear spring constant in addition to the physical spring used to maintain the inverted thruster platform position. The major source of uncertainty is thermal drift and this was minimized by shutting the thruster off (to obtain a “thrust stand zero”) and using the near-immediate change in displacement for the computation of thrust. Both the magnets and the flow are also extinguished rapidly with pneumatic valves inside the vacuum facility. During post-processing, the instantaneous inclination is also used to correct the LVDT signal using inclination calibration data. The total stacked uncertainty for the measurement of thrust was estimated at  $\pm 1.4\%$ .

#### 4. QCM

To measure the cumulative amount of carbon deposition throughout the ACDC testing a temperature controlled quartz crystal microbalance (QCM, Inficon XTM/2) was placed next to the H6MS as shown in Figure 15.

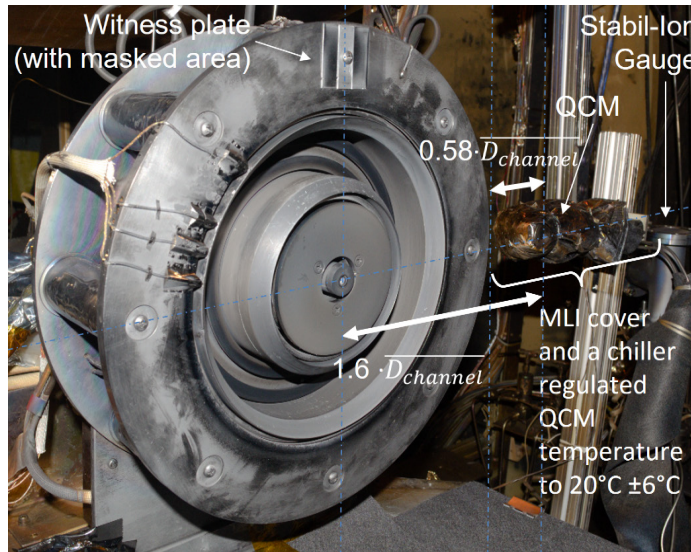


**Figure 15. H6MS installed in the Owens chamber at the start of Phase A testing showing QCM location as well as front facing witness plate.**

While it was desirable to place the QCM as close to the thruster as possible, there was concern that the elevated thruster temperature would overheat the QCM. The QCM sides were covered with multi-layer insulation (MLI) and a chiller was used in an attempt to maintain the QCM temperature at 20°C. While the thruster radiated heat was regulated to 18.0°C ±0.6°C during Phases A and C, the carbon blast target, used in Phase B, added significant heat to the QCM and deteriorated regulation to 20.0°C ±6°C. Under 6 kW H6MS operation, the carbon

target center temperature was 584°C and the edges were 184°C. The allowable temperature range for the QCM is 0°C to 50°C with recommended operation below 30°C. A more stable temperature is helpful to reduce thermal stiffness changes to the resonant deposition mass plate frequency and may also help prevent spalling of deposited material due to differences in thermal expansion coefficients.

The QCM manual states a deposited thickness measurement accuracy of ±0.5% (assuming the deposition material density is known). Prior H6MS experiments at JPL [26] have found carbon back-sputter rates of 3.8 μm/kh ±0.4 μm/kh using this QCM, and 4.0 μm/kh ±1.0 μm/kh using witness plates and a Nanovea profilometer during shorter 150 hour test campaigns. The uncertainty in the deposited density is expected to be small since Molecular Raman analysis of witness plates have revealed amorphous carbon as the main constituent [26]. For the presented ACDC data, the uncertainty in the average Phase B deposition rate is:

$$\text{deposition rate uncertainty, } \delta \dot{h} = 40 \mu\text{m} \cdot (\pm 0.5\%) / 0.413 \text{ kh} = \pm 0.5 \mu\text{m/kh} \quad (4)$$

#### 5. Thruster Instrumentation: Low-speed Telemetry (Hz, >160 channels)

During thruster operation in the JPL Owens test facility, standard low-speed (Hz) thruster telemetry were recorded and monitored throughout all ACDC test Phases.

- sense lines on DC power supplies: discharge, inner-/outer-magnets, cathode heater/keeper
- cathode to ground voltage
- body current
- 3x facility pressure Stabil-Ion gauges
- 4x in-situ wall probes for deposition film 4-wire resistance measurement
- 24x cryogenic vacuum pump temperatures (10 μA cryo diodes)
- cooling water temperatures
- propellant flow rates (anode and cathode)
- thrust vector probe currents (32 discrete signals)
- 25x type-K thermocouples (TC accuracy ±3°C)
- OPTO22-based logging with optical isolation
- FLIR 655 + telephoto lens + ZnSn viewport
- SLR (Nikon D600) and IP (1080p with DVR) cameras

The low-speed telemetry included all the calibrated sense lines on the DC power supplies (main discharge, inner magnet, outer magnet, cathode heater and cathode keeper), cathode to ground voltage, body current, facility pressure, cryogenic vacuum pump temperatures, cooling water temperatures, propellant flow rates (anode and cathode), thrust vector probe currents, and more (over 160 channels in all). Frequent DSLR high-resolution (24 MP) photographs were also collected during thruster operation and non-operation using a Nikon D600 and Micro-Nikkor 105 mm f/2.8 lens with exposure matched settings. A network digital video recording system also ran continuously through all ACDC test Phases collecting 1080p video.

#### 6. Thruster Instrumentation: High-speed Telemetry (kHz-MHz, 7-channels)

During thruster operation in the JPL Owens test facility high-speed (kHz-MHz) thruster telemetry were recorded and monitored throughout all ACDC test Phases.

- eight-channel 12-bit Teledyne LeCroy HDO8000 series oscilloscope
- CH1: anode current,  $I_a(t)$
- CH2: cathode current,  $I_c(t)$
- CH3: anode to cathode voltage,  $V_{a2c}(t)$
- CH4: cathode to ground voltage,  $V_{c2g}(t)$
- CH5: keeper to cathode voltage,  $V_{k2c}(t)$
- CH6: wall-probe to ground voltage,  $V_{wp}(t)$
- CH7: body current,  $I_b(t)$
- currents via Pearson Electronics model 41X current transformers (120 Hz-20 MHz)
- voltages via active high-voltage differential probes (PICO TA04X, DC-70 MHz)
- signal statistics (peak-to-peak, mean, standard deviation, etc.) logged every 2 seconds
- full scope traces (0.5-s windows at 100 MHz) every ~hour

The high-speed thruster telemetry was routed to an eight channel 12-bit Teledyne LeCroy HDO8000 series oscilloscope. Measured signals included anode current ( $I_a$ ), cathode current ( $I_c$ ), body current ( $I_b$ ), anode to cathode voltage ( $V_{a2c}$ ), cathode to ground voltage ( $V_{c2g}$ ), keeper to cathode voltage ( $V_{k2c}$ ), and wall probe to ground voltage ( $V_{wp}$ ). High-speed ( $\geq 20$  MHz bandwidth) current measurements were performed using Pearson Electronics model 410 and 411 current transformers while high-speed ( $\geq 70$  MHz bandwidth) voltage measurements were performed with active high-voltage differential probes (PICO TA043 and TA044). The signal statistics (peak-to-peak, mean, standard deviation, etc.) were continuously logged (once every 2 seconds) while full scope traces (0.5 second windows at 100 MHz) were collected every hour or every thruster condition change.

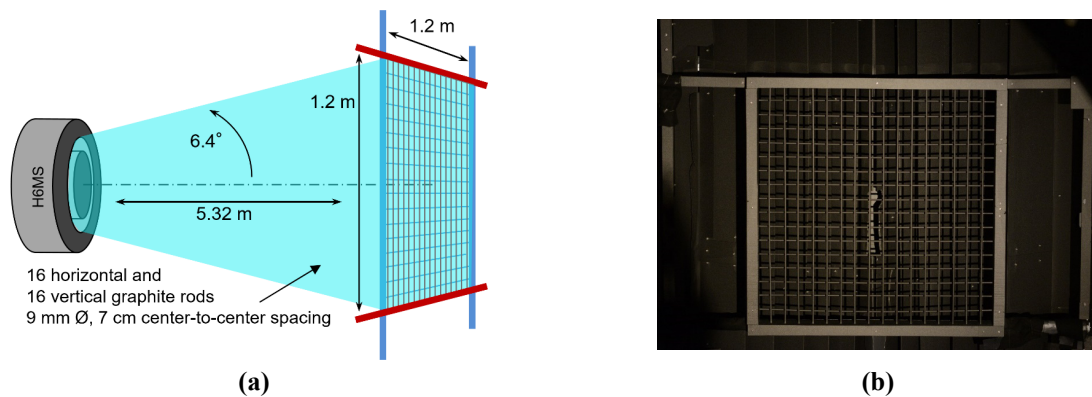


**Figure 16. (a) Schematic of JPL thrust vector probe and H6MS thruster. (b) Photograph of thrust vector probe array in front of Owens chamber beam dump.**

#### 7. Thrust Vector Probe

A collection of calibrated 16 horizontal and 16 vertical graphite rods (each 1.2 m long and 9 mm in diameter) are positioned in front of the main beam dump 5.3 m downstream from the H6MS thruster and are used to measure the instantaneous thrust vector,  $\theta_{thrust}$  (Figure 16) during Phases A and C. This thrust vector (TV) probe has been used successfully at JPL with flight electric thruster environmental test campaigns [27–29]. The carbon blast target used during phase B obscures the TV probe preventing the collection of  $\theta_{thrust}$  data during the accelerated carbon

deposition. Each rod is biased 20 V below the facility ground to collect beam ions and the horizontal and vertical ion beam centroids are located using Gaussian fits, as shown below and in Figure 17:

$$I_{h,v-beam}(x) = I_{h,v-fit} \exp\left(\frac{-(x - x_{h,v-fit})^2}{c_{hfit}}\right)$$

$$\theta_{beam} = \arctan\left(\frac{\sqrt{x_{hfit}^2 + y_{vfit}^2}}{Z = 5.32m}\right) \quad (5)$$

The ion beam centroid is also the exhausted propellant momentum centroid and thus the beam angle is equivalent to the thrust angle:

$$\theta_{thrust} = \theta_{beam} \quad (6)$$

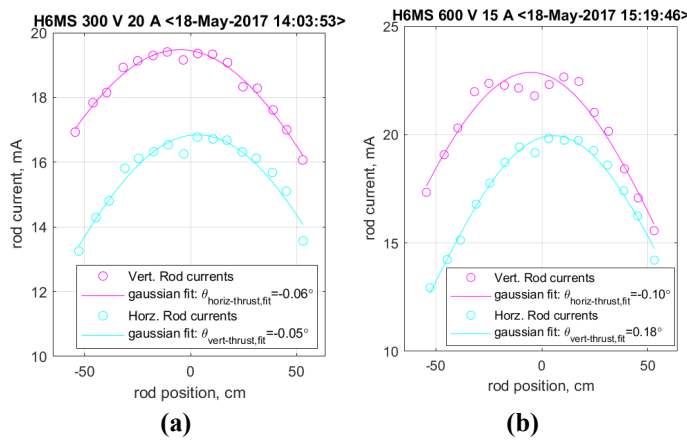


**Figure 17. Single points of thrust vector probe raw ion beam current centroid fitting for H6MS operation at (a) 300 V 6 kW and (b) 600 V 9 kW during Phase A.**

A custom laser alignment jig has been fabricated for the TDU-2 thruster (with perpendicularity calibrated to  $\pm 0.01^\circ$ ) to enable absolute calibration of the thrust vector angle with respect to the thruster centerline with an overall accuracy of approximately  $\pm 0.03^\circ$ . Testing with an additional alignment laser mounted to the base of the TDU-2 mounting bracket has shown facility and thermal drifts on the order of  $\pm 0.01^\circ$ . For ACDC H6MS testing, absolute TV probe alignment was not performed, and only thrust vector angle changes relative to the starting TV angle are presented.

### 8. Thermocouples and Thermography

During the ACDC test, 25 type-K thermocouples (TCs) were continuously monitored, but only four of these TC were mounted to the thruster as labeled in Table 2. The TCs have a nominal accuracy of  $\pm 2.2^\circ\text{C}$  or  $\pm 0.75\%$  (whichever is larger), but they were recorded by an OPTO22 based data-logger with an accuracy of  $\pm 3^\circ\text{C}$ .

**Table 2. Thermocouple locations (25x) for ACDC testing.**

TC Name and Location	TC Name and Location
H6MS inner screen (TS-A)	Graphite shield TC
H6MS front outer pole middle (TS-B)	Axial Motor Temp
H6MS front inner pole (TS-C)	CVI T <sub>water</sub> inlet
H6MS rear outer pole inner (TS-D)	CVI1 T <sub>water</sub> outlet
Carbon-blast-panel center	CVI2 T <sub>water</sub> outlet
Carbon-blast-panel edge	CVI3 T <sub>water</sub> outlet
QCM temperature	Beam Dump TC1-TC8
Damper coil (Front of Spool) TC 15	
Damper coil (On Upstream Coil) TC 07	
Shroud TC 11	
Shroud TC 12	

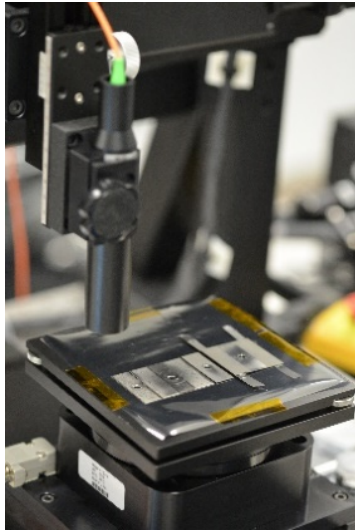


**Figure 18. Nanovea profilometer setup used to measure carbon deposition thicknesses.**

and has a vertical static noise of 1.7 nm. A series of positioning stages move the sample through a desired set of x-y coordinates.

A FLIR SC655 microbolometer infrared camera was set up to image the front face of the thruster (including the discharge channel ceramic which does not have any TCs) during the ACDC test Phases A and C. The ZnSe viewport and FLIR camera were calibrated together using a reference blackbody source and provide a temperature measurement accuracy of  $\pm 2^\circ\text{C}$  or  $\pm 2\%$  (whichever is larger) not including surface emissivity uncertainty.

#### 9. Profilometry Measurements

The profilometer system used to analyze the carbon deposition samples was a Nanovea unit (see Figure 18) that uses a non-contact white-light chromatic confocal technique to measure sample surface height. The Nanovea scanner can measure maximum vertical angles of  $87^\circ$

### III. Results

#### A. Pathfinding Experiments: Carbon Blast Panel Deposition Optimization

Initial pathfinding experiments in late 2016 helped identify and demonstrate the feasibility of the optimal setup for accelerating the carbon back-sputter rate. These Phase 0 tests have already been discussed in Section II.A.0, with the identification of 9 kW H6MS operation and a carbon target distance of 0.5 m downstream to maximize the back-sputter rate as shown in Figure 4. Thus, 600 V 9 kW H6MS operation was used along with a fixed 0.5 m carbon target position at the start of Phase B, the accelerated carbon deposition. However, facility stability issues, an unexpected thruster shutdown, and an overheated carbon target temperature (see Figure 5 and Section II.A.3) occurred at this condition and 300 V 6 kW operation (0.5 m target) was subsequently used for the entire 40  $\mu\text{m}$  of carbon deposition. The H6MS accelerated and nominal Owens chamber carbon back-sputter rates are presented in Table 3 along with TDU-2 and GRC VF-5 data:

**Table 3. Carbon back-sputter rates for various thrusters, facilities, and setups.**

Thruster and Power	Facility and Configuration	Carbon back-sputter rate
H6MS 6-kW	Nominal JPL Owens Chamber (Phase A and C)	0.91 $\mu\text{m}/\text{kh}$
H6MS 9-kW	Nominal JPL Owens Chamber (Phase A and C)	2.4 $\mu\text{m}/\text{kh}$
H6MS 6-kW	Accelerated Carbon Deposition (0.5 m target) JPL Owens Chamber	98.0 $\mu\text{m}/\text{kh}$
TDU-2 12.5-kW	Nominal GRC VF-5 (from Ref. [30])	1.8 $\mu\text{m}/\text{kh}$
TDU-2 12.5-kW	Nominal JPL Owens Chamber (during SLA test [12])	4.4 $\mu\text{m}/\text{kh}$

Throughout the accelerated carbon deposition Phase B, the back-sputtered film thickness measured by the QCM was recorded and these data are plotted against operational hours in Figure 19.

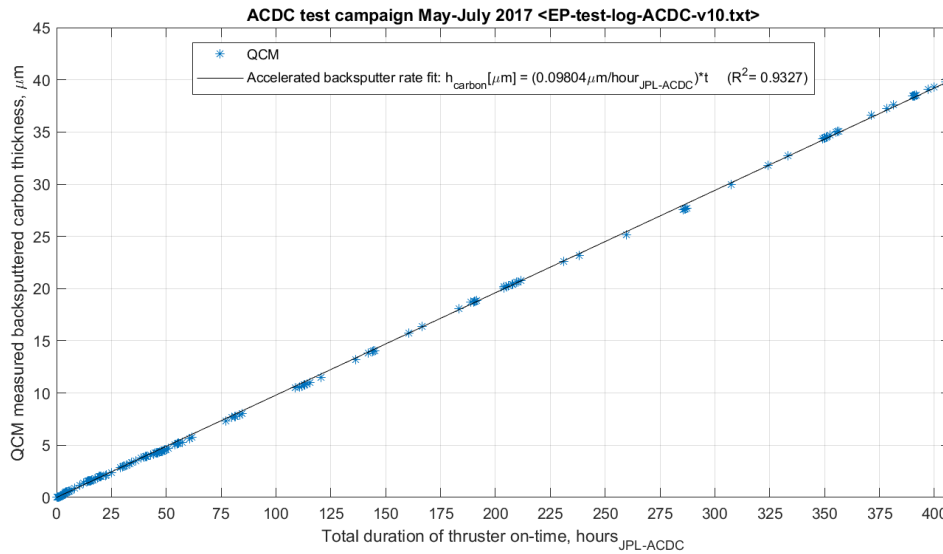


**Figure 19. QCM measurements of back-sputtered carbon film thickness as a function of total H6MS on-time during accelerated carbon deposition (Phase B) with curve fitted overall rate of 98.0  $\mu\text{m}/\text{kh}$ .**

A linear least-squares regression fit to these data provide an effective Phase B accelerated back-sputter rate of 98.0  $\mu\text{m}/\text{kh}$ :

$$\text{back - sputtered carbon thickness, } h(t) = 98.0 \frac{\mu\text{m}}{\text{kh}} \cdot (t[\text{kh}_{ACDC}]) \quad (7)$$

Equation (7) is used in later analysis to determine the instantaneous carbon deposition thickness. This allows for plotting all relevant test parameters as a function of back-sputtered carbon thickness. Analyzing thruster data in this manner helps liberate the results from thruster, power level, facility, and configuration dependences (as seen in Table 3) since carbon thickness is the true independent variable of the ACDC test.

## B. Photographic Carbon Deposition Observations

A Nikon DSLR camera was used to collect photographs with matched exposure settings throughout the carbon deposition process. A series of 16 photographs taken at various times during Phase B is presented in Figure 20.

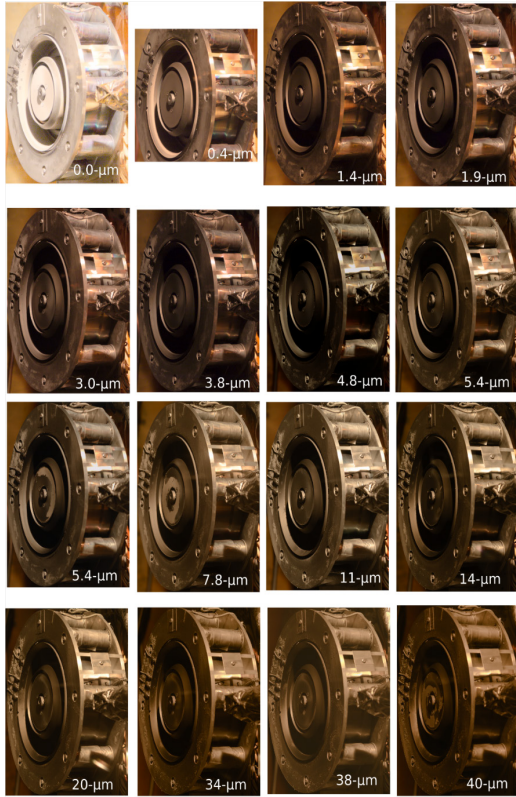


**Figure 20. Photographic progression of back-sputtered carbon deposition on the H6MS with matched exposures.**



**Figure 21. “Black lights” created by Phase B of the ACDC test campaign.**

While it was planned to use the same camera aperture, exposure, and ISO sensitivity for the entire Phase B deposition, the unanticipated degree of viewport and internal light bulb darkening (see “black-lights” created in Figure 21) necessitated increased exposure times (up to 16 times longer or +4 EV) as the test progressed. Using the RAW (12-bit 3-channel RGB) \*.NEF images, the exposures were fully matched in post-processing. While the thruster was readily visible to the camera and the naked-eye when unpowered and the internal chamber lights active at the start of the ACDC test, a strong external light source was later needed to “see” the unpowered thruster and enable the camera to autofocus.

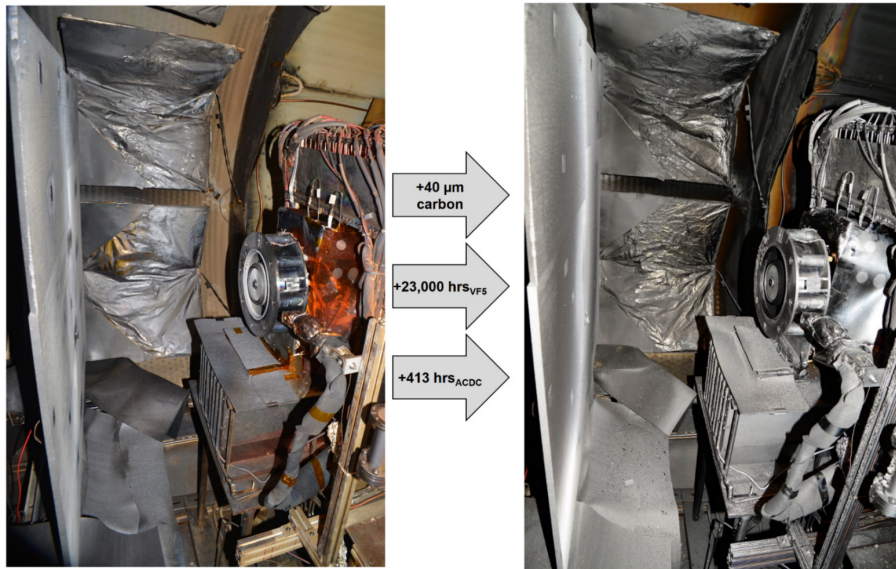


**Figure 22. Photographs of carbon blast panel and H6MS at start of Phase B (0 μm-carbon) and at conclusion of Phase B (40 μm-carbon) corresponding to 23,000 hours of equivalent runtime in the NASA VF-5 chamber.**

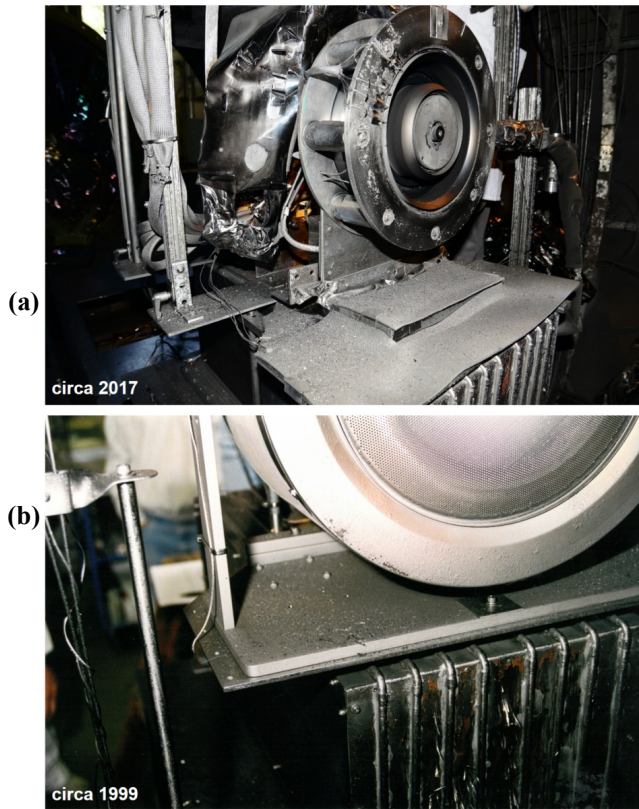


**Figure 23. Photographic of post-deposition (a) H6MS thruster from this ACDC test (23,000 h<sub>equiv.</sub>) and (b) NSTAR thruster after 30,352 h (see Ref. [2]) as mounted to the same Owens chamber thrust stand.**

As the thruster was coated in 40- $\mu\text{m}$  of back-sputtered carbon, the facility was also coated as shown in Figure 22, Figure 23, and Figure 24. After the deposition, the photographs reveal a nearly black-and-white scene as carbon coated all surfaces with line-of-sight to the carbon blast panel. In Figure 23, the post-deposition H6MS is photographically compared to the NSTAR ion thruster after the Extended Life Test of 30,352 h in the same Owens test chamber and on the same thrust stand. Remarkably similar carbon deposition features such as peeling, flakes, and dust are observed in both tests providing qualitative evidence that the accelerated deposition process used in the ACDC test produced representative carbon back-sputter of a non-accelerated test.

**C. Thruster Temperatures, Voltages, and Current throughout Deposition**

The H6MS thruster operated throughout the full 40  $\mu\text{m}$  of carbon deposition with no noticeable changes in peak operating temperatures or other common thruster parameters such as cathode to ground voltage. Figure 25 and Figure 26 show all thruster temperatures as well as thruster power, discharge current (“Jd”), keeper current (“Jck”), cathode to ground voltage (“Vg”), and anode flow rate (mg/s). Figure 25 uses a timestamped horizontal axis while Figure 26 filters the data and only plots the cumulative on-time hours run since the start of the Phase B deposition.

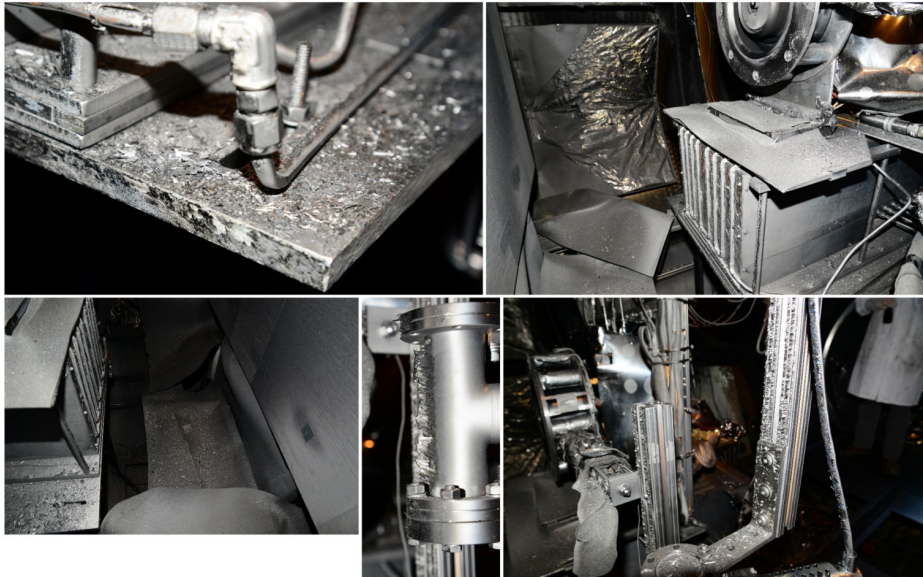


**Figure 24. Various photographs of facility after the full 40  $\mu\text{m}$  of back-sputtered carbon was achieved.**

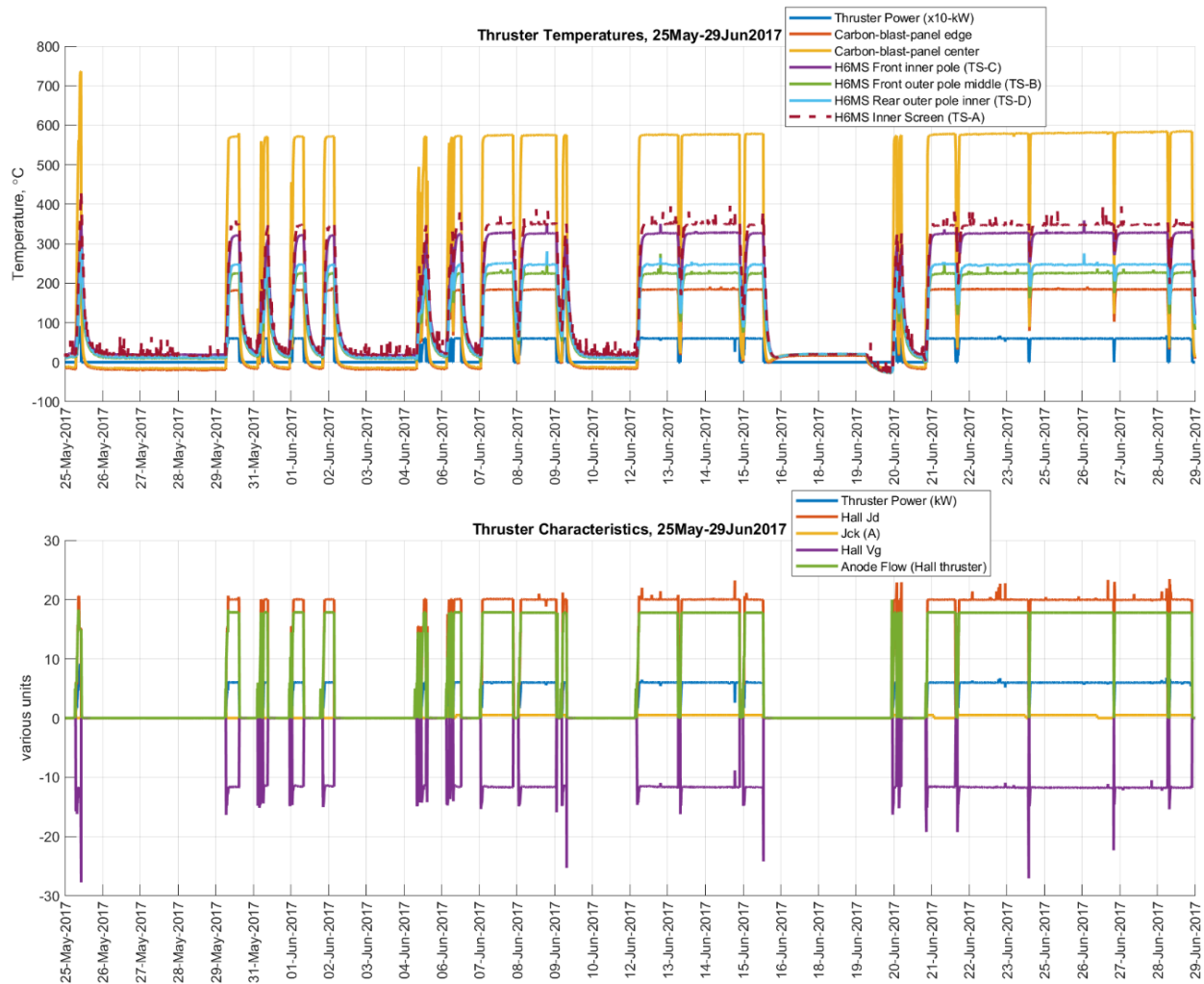


**Figure 25. Thruster temperatures (upper traces), voltages (volts), currents (amperes), power, and anode flow (mg-Xe/s) plotted using a timestamped horizontal axis.**

Examining the data in Figure 26, the portions of all signals during steady-state operation of the thruster are all collinear or invariant with time or the amount of carbon deposition from 0 to 40  $\mu\text{m}$ . There about two dozen thruster startups that are visible in any of the temperature signals. Also visible in the thruster temperature data, are occasional +10-20°C spikes that may represent minor shifts in thruster component mating interfaces or the TC interface.

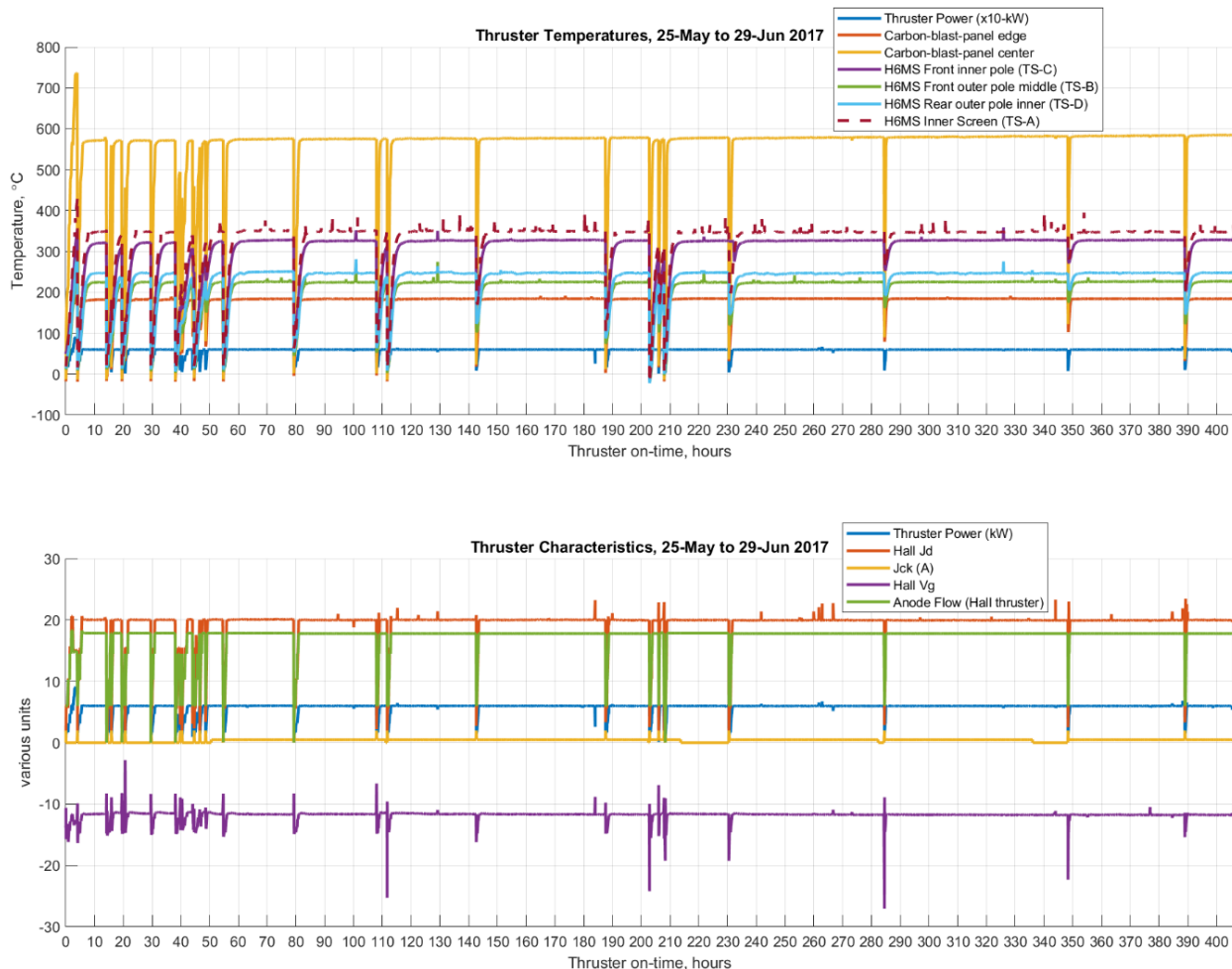


**Figure 26. Thruster temperatures (upper traces), voltages (volts), currents (amperes), power, and anode flow (mg-Xe/s) plotted using cumulative on-time hours since the start of Phase B deposition.**

The discharge current was controlled indirectly using the anode flow rate, but the flow rate was essentially held constant at  $17.8 \text{ mg-Xe/s} \pm 0.1 \text{ mg-Xe/s}^{\dagger\dagger}$  throughout the entire deposition process (ignoring bakeouts and startups). Even with the constant flow rate, occasional small spikes (1-2 A) in discharge current were observed that were caused by xenon “snow” (condensed xenon ice crystals) falling off the cryogenic pumping surfaces. The facility pressure throughout the entire deposition process is plotted in Figure 27. These data show a multitude of small pressure spikes  $+1\text{-}5 \text{ } \mu\text{torr-Xe}$  as well a couple larger pressure spikes that triggered automated thruster shutdowns. Aside from these spikes, the facility pressure varied from  $9\text{-}14 \text{ } \mu\text{torr-Xe}$  throughout the entire deposition campaign. One facility “regen” (regeneration where cryo-surfaces are warmed and facility re-pumped down) was performed 204 hours into thruster on-time as is visible in the decreased initial operational pressure at this time in Figure 27.

<sup>††</sup> While the setpoint changes were  $\pm 0.1 \text{ mg-Xe/s}$ , the MFC accuracy was actually  $\pm 0.18 \text{ mg-Xe/s}$ .

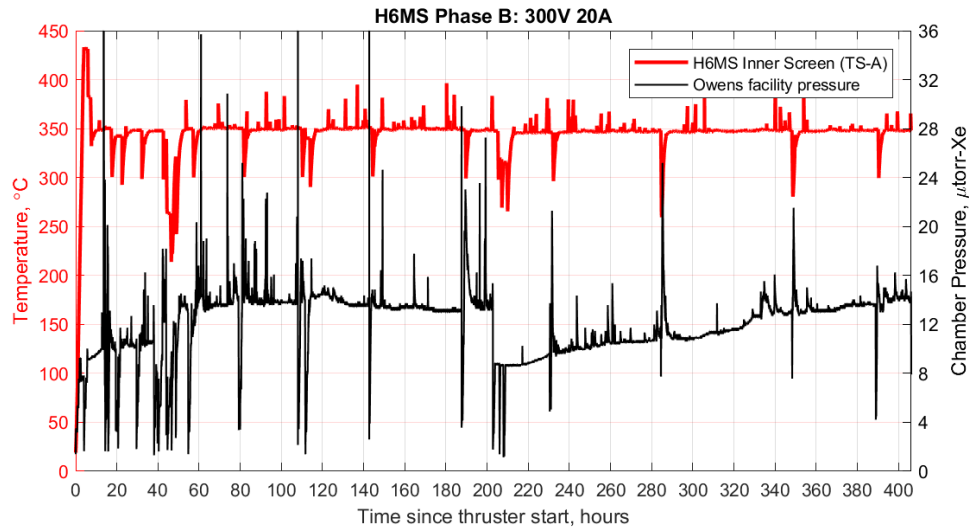


**Figure 27. Thruster inner screen temperatures (“red”) and facility pressure (“black”), showing occasional pressure spikes. A facility regen occurred at 204 hours into the thruster on-time.**

#### D. Thruster Oscillation Dynamics throughout Deposition

Along with the steady-state thruster telemetry, high-speed thruster oscillation dynamics were collected throughout the 40  $\mu\text{m}$  of carbon deposition. These data were collected as described in Section II.G.6. A custom LabVIEW script queried the oscilloscope once every 2 seconds for the peak-to-peak, standard deviation, and average value of all signals and logged these continually throughout the deposition process. Each set of statistics was computed from a 100 ms wide window of data with a DC to 70 MHz bandwidth. During the deposition process, carbon flare and spark events were routinely observed visually and in the high-speed thruster telemetry signals. Further discussion and analysis of these events is in Section III.0. While these events are important to understand, they complicate tracking the trends of the thruster oscillation dynamics throughout the deposition. Thus, the peak-to-peak and standard deviation data are filtered in post-processing to remove most spark and flare events. In this manner, the thruster oscillation data are more natural or nominal<sup>‡‡</sup> and any changes in dynamics arising from the growing layer of back-sputtered carbon can be readily identified. Figure 28 and Figure 29 track the history of the discharge current (anode, cathode, and body) peak-to-peak and standard deviation amplitudes respectively. Figure 30 and Figure 31 track the history of the thruster voltages (anode-to-cathode, cathode-to-ground, and keeper-to-cathode) peak-to-peak and standard deviation amplitudes respectively.

<sup>‡‡</sup> The off-nominal presence of the graphite blast panel just 0.5 m downstream perturbs the plume and causes slightly increased amplitude oscillations as shall be discussed later.

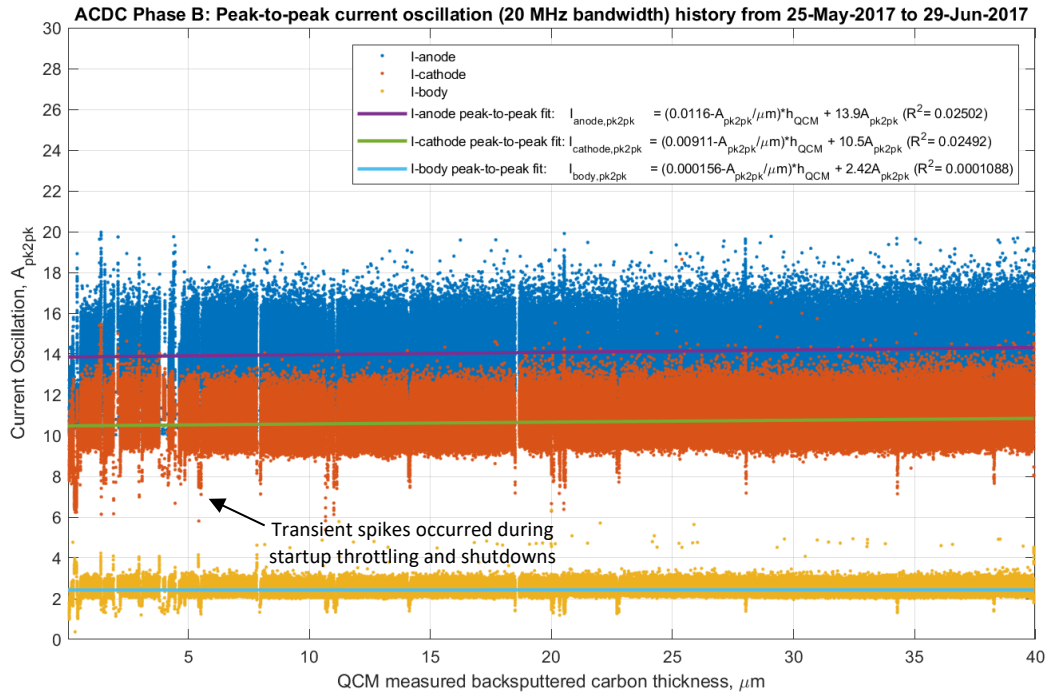


**Figure 28. Thruster discharge peak-to-peak variations (bandwidth 120 Hz – 20 MHz) from 0-μm to 40-μm for anode (“blue”), cathode (“orange”), and body (“gold”) current oscillations with curve fits.**

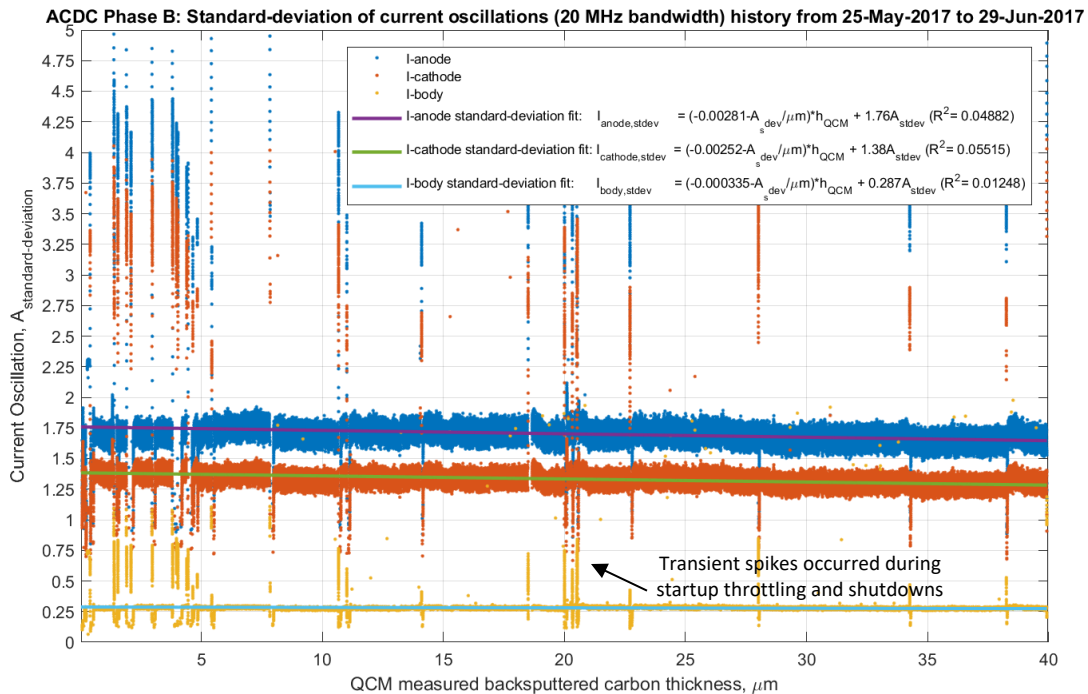


**Figure 29. Thruster discharge standard deviation variations (bandwidth 120 Hz – 20 MHz) from 0-μm to 40-μm for anode (“blue”), cathode (“orange”), and body (“gold”) current oscillations with curve fits.**

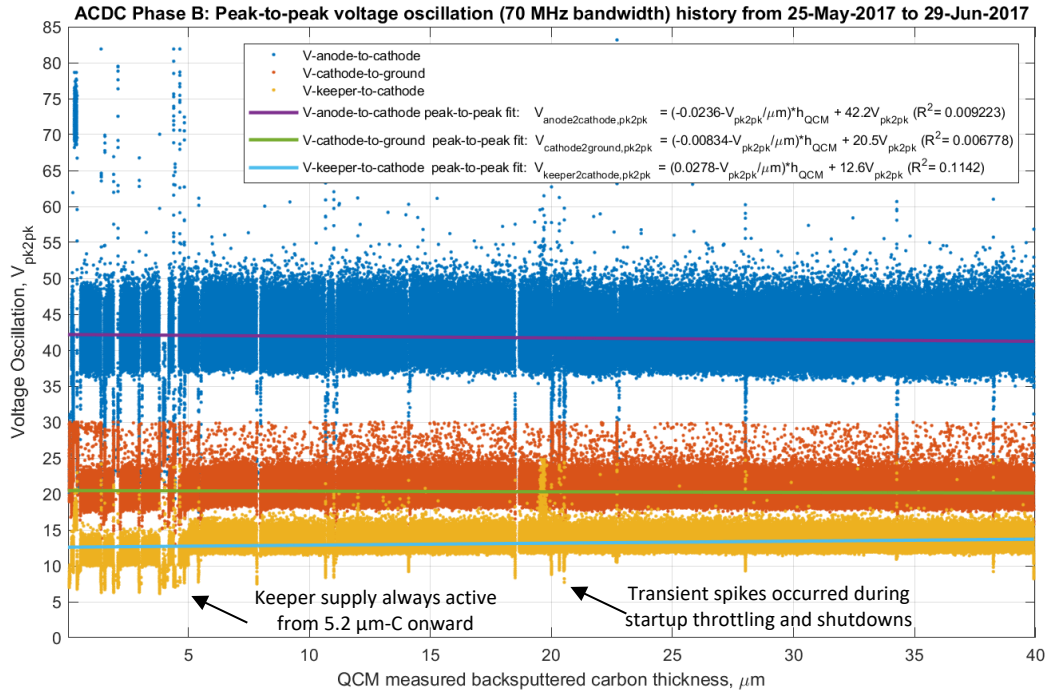


**Figure 30. Thruster discharge peak-to-peak variations (bandwidth DC - 70 MHz) from 0- $\mu\text{m}$  to 40- $\mu\text{m}$  for anode to cathode (“blue”), cathode to ground (“orange”), and keeper to cathode (“gold”) voltage oscillations with curve fits.**

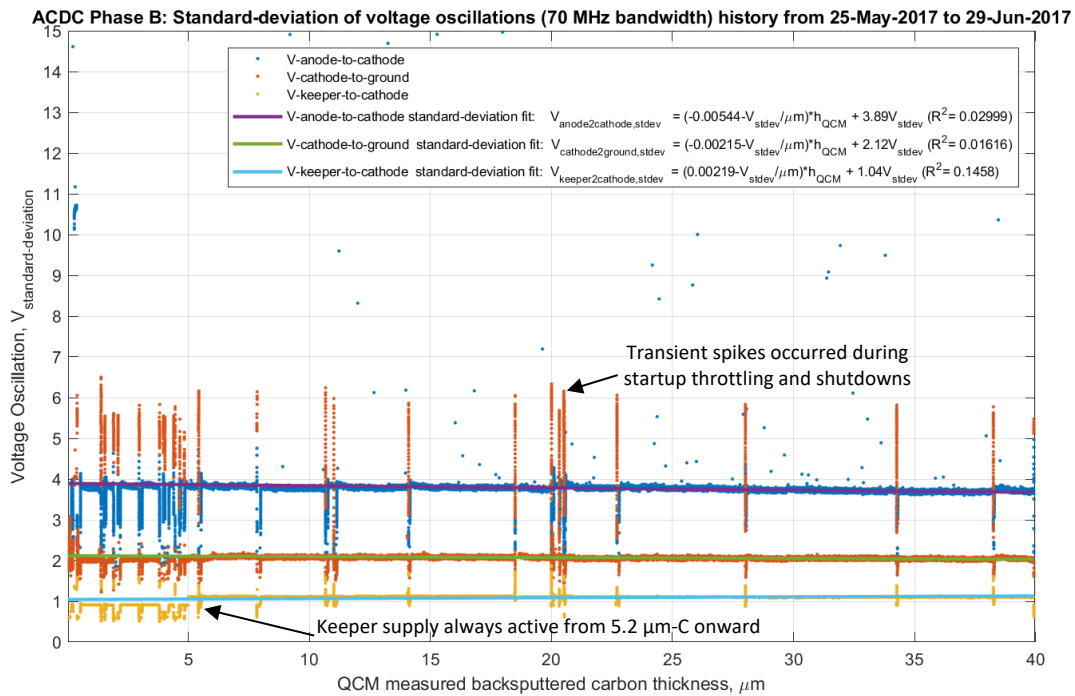


**Figure 31. Thruster discharge standard deviation variations (bandwidth DC - 70 MHz) from 0- $\mu\text{m}$  to 40- $\mu\text{m}$  for anode to cathode (“blue”), cathode to ground (“orange”), and keeper to cathode (“gold”) voltage oscillations with curve fits.**

These data have all been plotted with respect to the QCM measured carbon deposition by using Eq. (7) to help universalize the results. Various notes have been added to these plots such as the continuous activation of the keeper from 5.2  $\mu\text{m-C}$  onward and the spikes caused by the  $\sim 24$  thruster restarts. Curve fits were applied to all the oscillation data in Figure 28 through Figure 31 but no statistically significant trends were observed. *Thus, the oscillation amplitudes are invariant throughout the entire Phase B deposition process.*

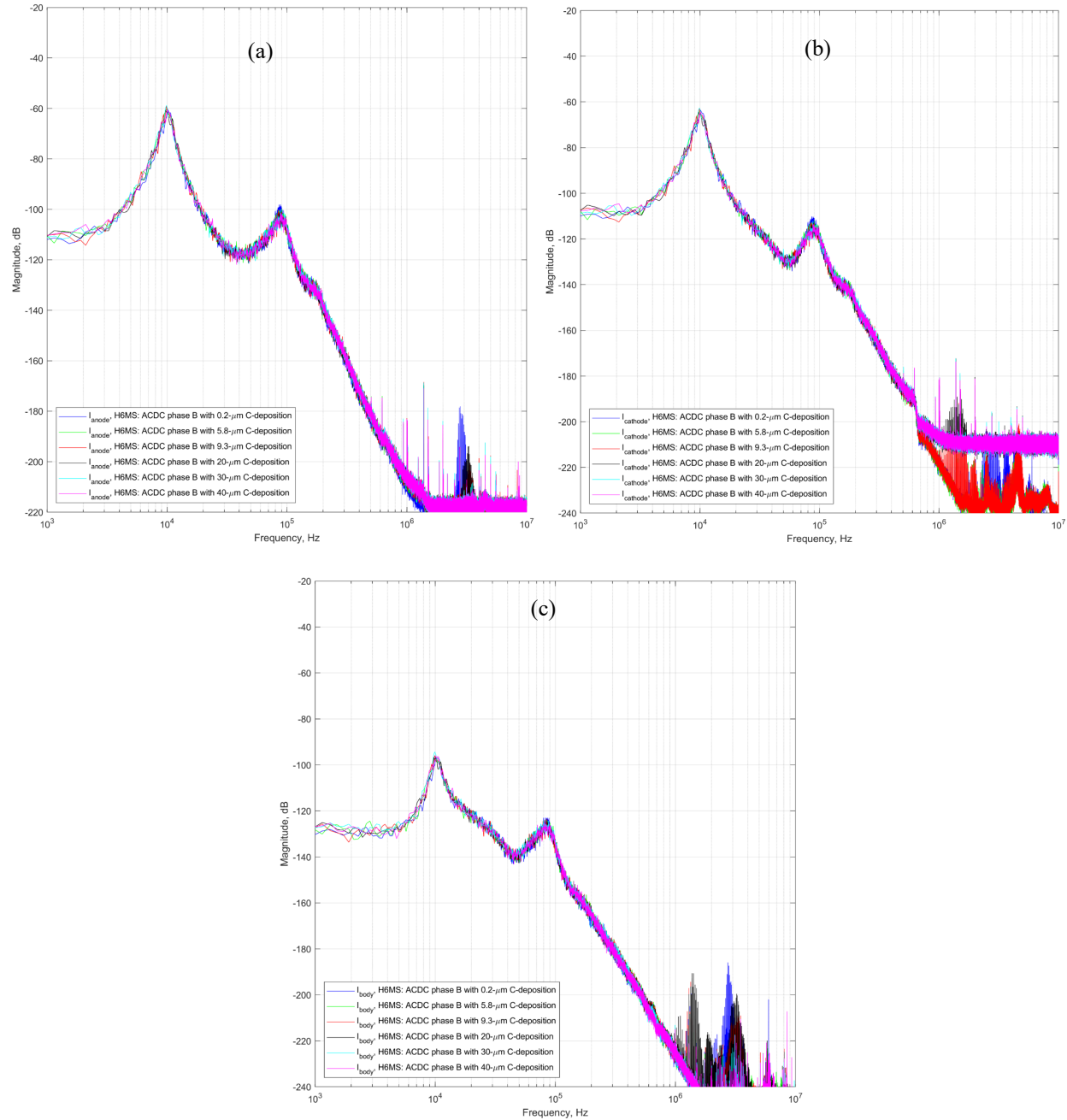


**Figure 32. Power spectral density plots of the (a) anode current,  $I_a$ , (b) cathode current,  $I_c$ , and (c) body current,  $I_b$ , throughout Phase B for  $\sim 0.2 \mu\text{m}$  (“blue”),  $5.8 \mu\text{m}$  (“green”),  $9.3 \mu\text{m}$  (“red”),  $20 \mu\text{m}$  (“black”),  $30 \mu\text{m}$  (“cyan”), and  $40 \mu\text{m}$  (“magenta”) of carbon deposition. Note: the graphite blast panel is directly  $0.5 \text{ m}$  downstream of the H6MS for the data. Also, the scope input range for the cathode current was increased for the  $20\text{-}30 \mu\text{m}$  data resulting in a higher noise floor evident in the spectral flat-lining above  $600 \text{ kHz}$ .**

While these plotted data have had most of the carbon flare and spark event filtered out, one may instead use the unfiltered high-speed signal statistics to assess the carbon flare/spark event rate. A total of 3,228 apparent carbon flare/spark events were thus observed during the 407.4 hours<sub>ACDC</sub> of Phase B operation corresponding to 8 flare/spark events per hour<sub>ACDC</sub>, or equivalently one flare/spark event every 7.6 minutes of ACDC Phase B testing. Early in the Phase B testing larger spark events led to unexpected thruster shutdowns. This was remedied by using the keeper at all times. Using the measured flare/spark event rate and the initial shutdown rate it appears that 2% of the identified flare/spark events would lead to unexpected shutdowns (unless the keeper was active). *Based on this, for the upcoming Long Duration Wear Test (LDWT) in VF-5, the anticipated rate of unexpected thruster shutdowns is once every 14 days.*

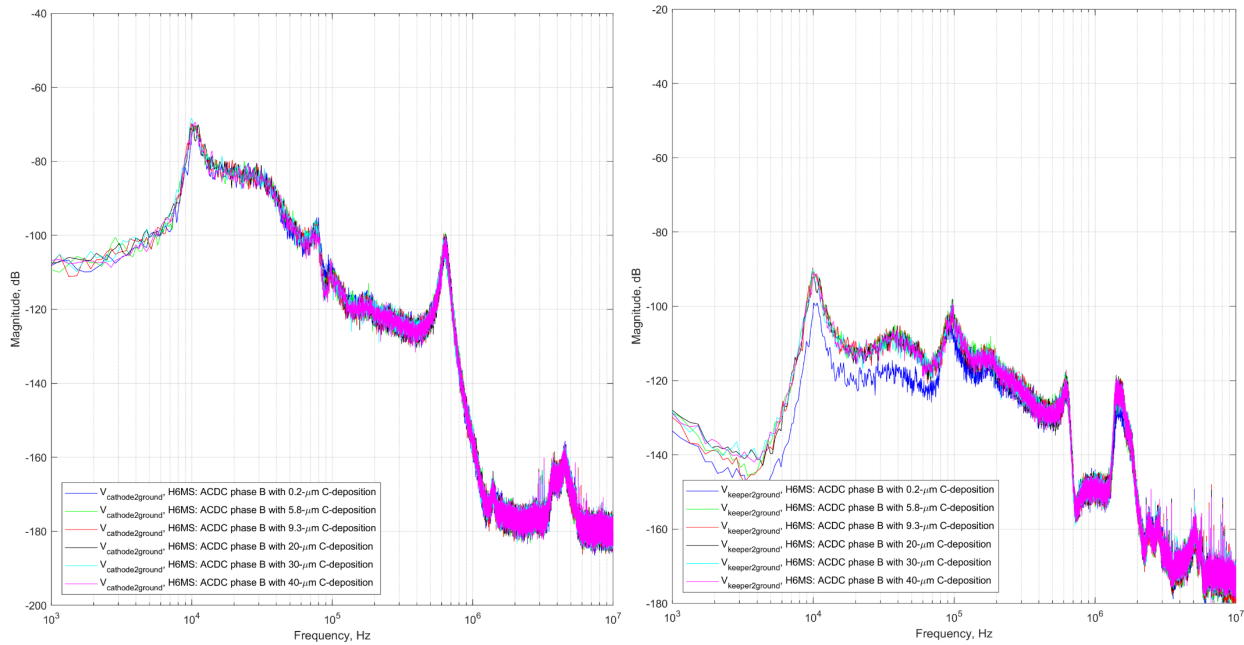


**Figure 33. Power spectral density plots of the (left) cathode to ground voltage,  $V_{c2g}$ , and (right) keeper to cathode voltage,  $V_{k2c}$ , throughout Phase B for  $\sim 0.2 \mu\text{m}$  (“blue”),  $5.8 \mu\text{m}$  (“green”),  $9.3 \mu\text{m}$  (“red”),  $20 \mu\text{m}$  (“black”),  $30 \mu\text{m}$  (“cyan”), and  $40 \mu\text{m}$  (“magenta”) of carbon deposition. Note: the graphite blast panel is directly  $0.5 \text{ m}$  downstream of the H6MS for the data**

In addition to the high-speed signal amplitude statistics, full scope traces were also collected at regular intervals throughout the carbon deposition. Figure 32 and Figure 33 show the power spectral densities at six different carbon deposition thicknesses spanning the full test campaign. All signal dynamics (except the keeper-to-cathode) are invariant during the deposition process. The only outlier is the first keeper-to-cathode spectrum for  $0.2 \mu\text{m}$  which was acquired with the keeper turned off (which is nominal for the H6MS). The remaining keeper-to-cathode traces had the keeper active with a  $0.5 \text{ A}$  discharge to prevent the thruster from shutting down unexpectedly during large spark events. The repeatability of the thruster dynamics with carbon deposition thicknesses from  $0.2 \mu\text{m}$  to  $40 \mu\text{m}$  is impressive and further demonstrates the effectiveness of magnetic shielding in liberating the thruster from plasma-wall interactions.

### E. Thruster Impedance Variation during Deposition

The high-potential isolation of the thruster underwent large variations throughout the  $40 \mu\text{m}$  deposition, trending downward many orders of magnitude with no noticeable effect on the behavior of the thruster. Isolation of the thruster body to various thruster components is presented in Figure 34, while additional anode isolations are plotted in Figure 35.

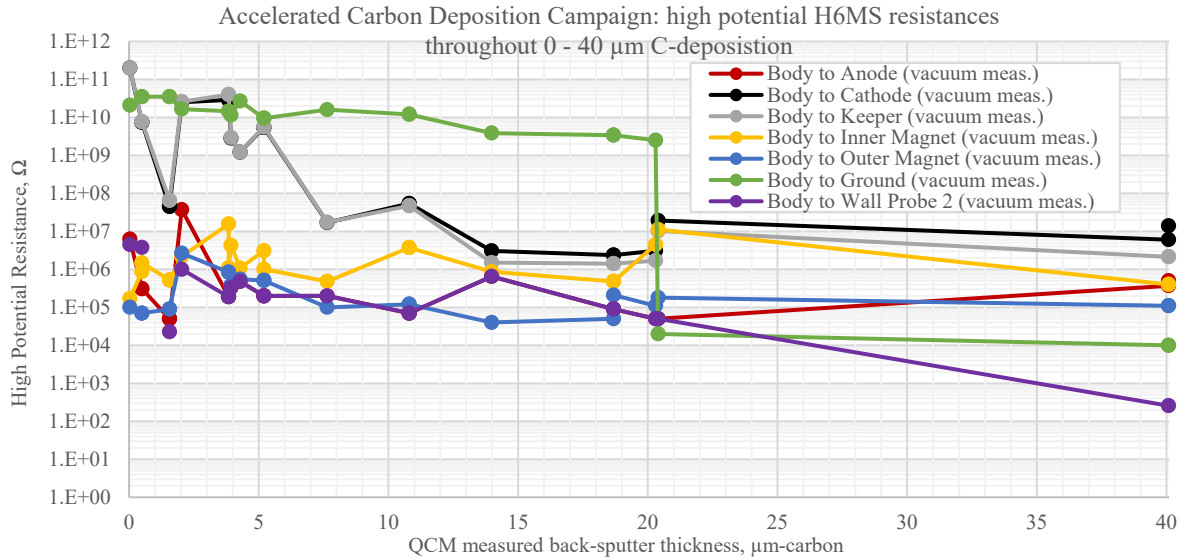


**Figure 34. Thruster high-potential measurements with respect to thruster body throughout Phase B testing as back-sputtered carbon thickness increased from  $<1 \mu\text{m}$  to  $40 \mu\text{m}$ . Note: while thruster was operated in body-tied to cathode configuration, the body and cathode were temporarily disconnected while performing these high-voltage isolation measurements**

Scatter in these data is due to sloughing off of carbon during thermal cycles, flare or spark events in-test, as well as the high-potential testing clearing/aggravating carbon film contacts. While most isolation resistances drop rather precipitously (by up to over six orders of magnitude), they do not appear to affect nominal thruster operation with—for example—the maximum power dissipated with an anode-to-body isolation of  $50 \text{ k}\Omega$  (the minimum measured isolation) is  $< 2 \text{ W}$ , or  $0.03\%$  of the discharge power. To help keep these data consistent, only vacuum high-impedance measurements are included.<sup>§§</sup>

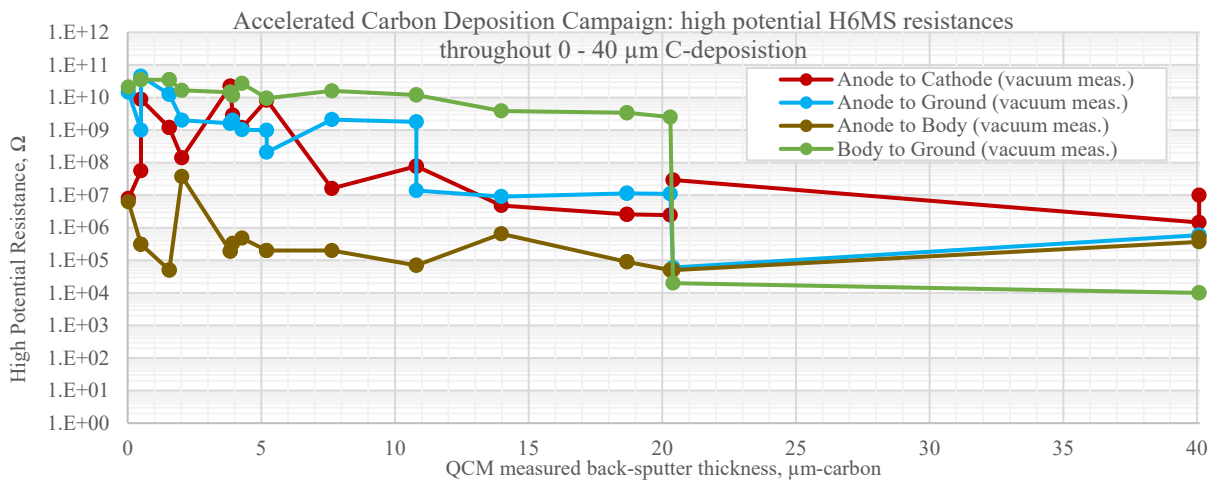


**Figure 35. Thruster high-potential measurements with respect various surfaces throughout Phase B testing as back-sputtered carbon thickness increased from  $<1 \mu\text{m}$  to  $40 \mu\text{m}$ . Note: while thruster was operated in body-tied to cathode configuration, the body and cathode were temporarily disconnected while performing these high-voltage isolation measurements**

<sup>§§</sup> While the pressure was high-vacuum  $\leq 1 \times 10^{-6}$  torr for these data, the thruster temperature varied (from  $-15^\circ\text{C}$  to  $+430^\circ\text{C}$ ).

## F. In-situ Wall Resistance Probes

The in-situ wall probes discussed in Section II.G.2, behaved intermittently during the ACDC testing occasionally appearing to detach and reattach electrically from the back-sputtered carbon coating the wall region local to each probe. This resulted in inconsistent wall voltage measurements throughout the campaign as depicted in Figure 36. For the first 14  $\mu\text{m}$  of carbon deposition Wall Probe 1 (WP1) was connected to the high-speed scope. It was noted in-test that the WP1 connection to the thruster channel was permanently lost, thus after 14  $\mu\text{m}$ , WP2 was connected instead. The original intent for the in-situ wall probes was to perform accurate 4-wire resistance measurements throughout the carbon deposition, but the erratic behavior prevented these measurements. The secondary use of the wall probes was the collection of the floating wall potential data as seen in Figure 36. These measurements were performed while the thruster was active and they clearly show that the wall probes—when connected to the local discharge channel wall graphite—floated up a bias near the operational discharge voltage.

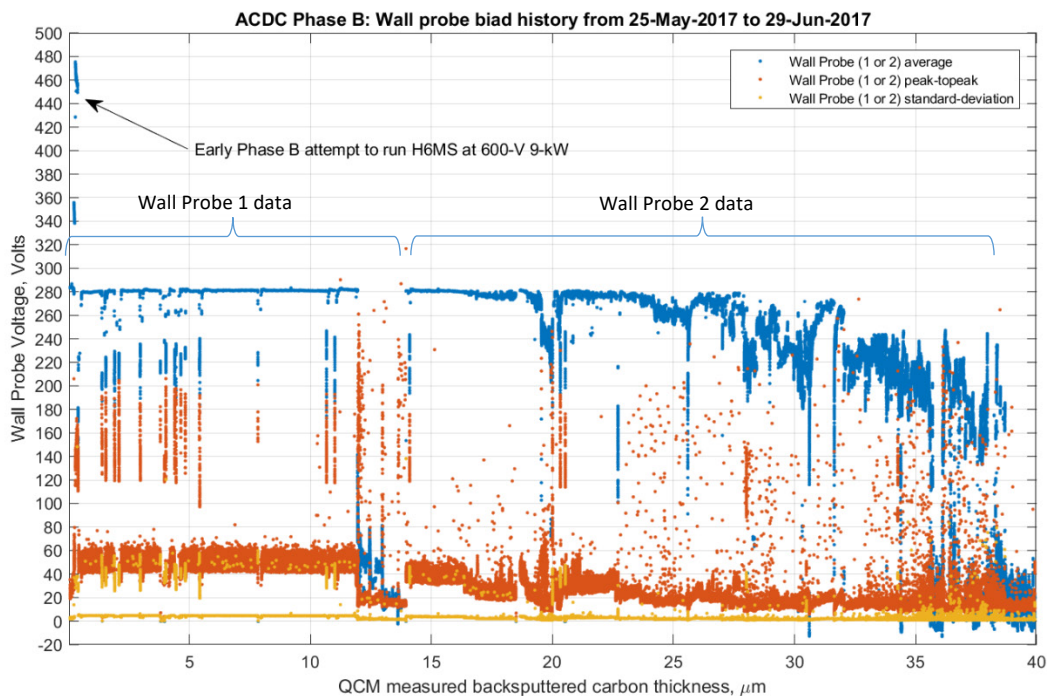


**Figure 36. Thruster in-situ wall probe data (bandwidth DC - 70 MHz) from 0- $\mu\text{m}$  to 40- $\mu\text{m}$  including time-average voltage (“blue”), peak-to-peak voltage (“orange”), and standard deviation voltage (“gold”).**

Since the in-situ wall probe bias was measured with respect to facility ground (using an active high-voltage differential 100x probe, PICO TA044), it is accurate to compare it to the anode-to-ground voltage,  $V_{a2g}$ , as shown in Eq. (8).

$$V_{WP} \approx 281 \text{ V} \pm 6 \text{ V}$$

$$V_{a2g} = V_{a2c} + V_{c2g} \approx 300 \text{ V} + (-11.5 \text{ V}) = 288.5 \text{ V} \pm 1 \text{ V} \quad (8)$$

$$\text{thus, } V_{WP} \approx V_{a2g}$$

This result, that the discharge channel walls float to the anode potential (within  $1 \times T_e$ ), has been observed with magnetically shielded thrusters [8,16] and is crucial to the theory of effective magnetic shielding in Hall thrusters.

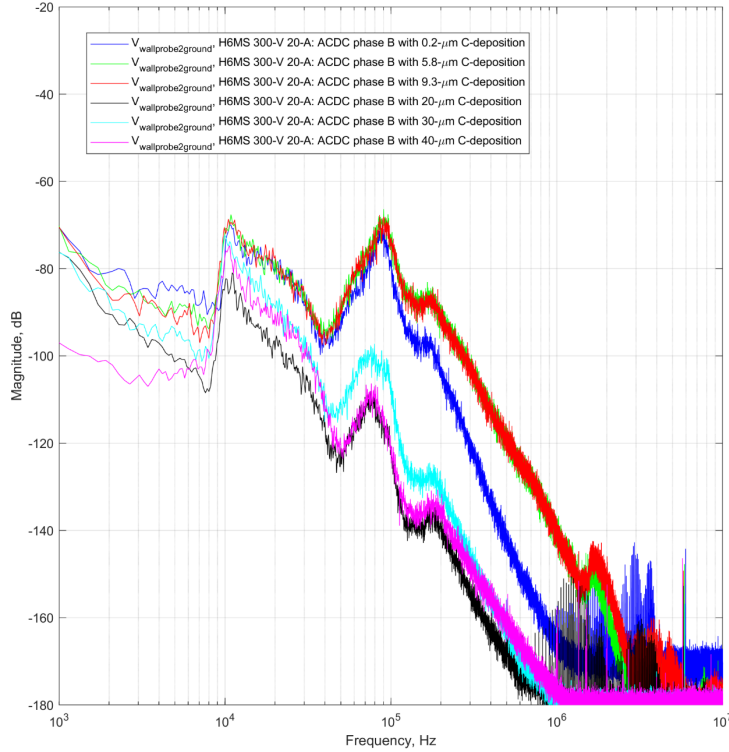


**Figure 37. In-situ wall probe oscillation spectra at various times during the Phase deposition from 0.2- $\mu\text{m}$  to 40- $\mu\text{m}$ .**

resolved inner and outer channel wall surface resistance measurements were conducted. Figure 38 presents these axially resolved surface resistance measurements. The axially averaged wall resistances for the 0  $\mu\text{m}$ , <1  $\mu\text{m}$ , and 40  $\mu\text{m}$  carbon deposition are presented in Eq. (9).

$$\text{Pre-Phase 0: } \overline{R_{0\mu\text{m}}} \approx 1 \text{ M}\Omega \pm ? \text{ M}\Omega$$

$$\text{Pre-Phase A: } \overline{R_{<1\mu\text{m}}} = 3.3 \text{ k}\Omega \pm 0.3 \text{ k}\Omega \quad (9)$$

$$\text{Post-Phase C: } \overline{R_{40\mu\text{m}}} = 36 \text{ }\Omega \pm 4 \text{ }\Omega$$

The initial pre-Phase-0 0- $\mu\text{m}$  data were collected with a coarser axial grid, with a different (un-calibrated) 4-wire resistance measurement unit, and using an incorrect probe ordering thus the accuracy of these data is unknown. While the uncertainty of the 4-wire sensing instrument used for the pre-Phase A and post-Phase C measurements was  $<\pm 0.0001\%$  the repeatability of these hand measurements was assessed by measuring the standard deviation of >30 measurements. The standard deviation was typically 10% of the mean value and this was used to estimate the pre-Phase A and post-Phase C resistance measurement uncertainty. Computing the local ratios of resistance change from <1  $\mu\text{m}$  to 40  $\mu\text{m}$  in Figure 38, and averaging all axial locations yields the average reduction surface resistance shown in Eq. (10).

$$\text{Inner ring } \overline{(R_{<1\mu\text{m}}/R_{40\mu\text{m}})} = 243 \quad (10)$$

$$\text{Outer ring } \overline{(R_{<1\mu\text{m}}/R_{40\mu\text{m}})} = 177$$

While accurate data at 0  $\mu\text{m}$  is not available, the existing data suggests the ratio may be nearly 300x larger than the Eq. (10) reductions or:  $\overline{(R_{0\mu\text{m}}/R_{40\mu\text{m}})} \approx 63,000$ . This suggests an exponential relationship between the surface resistance and the thickness of carbon deposition early in the deposition process.

In Figure 37, a collection of in-situ wall probe oscillation spectra are collected throughout the Phase B deposition from 0.2- $\mu\text{m}$  to 40- $\mu\text{m}$ . The magnitudes of the traces drop throughout the deposition due to the gradual loss of electrical contact from the wall probe electrode and the local graphite coating of the discharge channel. The two dominant mode frequencies of 10.3 kHz and 88 kHz match the two dominant modes seen in the other high-speed thruster telemetry during Phase B including: anode current, cathode current, body current, anode-to-cathode potential, and the keeper-to-cathode potential.

### G. Resistance along Channel Walls

Prior to the start of both the ACDC Phase 0 and Phase A testing, sets of axially resolved inner and outer channel wall surface resistance measurements were conducted using the 4-wire sensing method detailed in Section II.G.1. While the pre-Phase 0 measurements were taken after abrasively cleaning carbon off the BN channel walls, the initial pre-Phase A measurements are for the H6MS rings after the short 14 hour Phase 0 ACDC tests (Oct. 2016) with less than 1  $\mu\text{m}$  of accumulated carbon deposition. After the completion of the ACDC Phase C testing, another set of axially

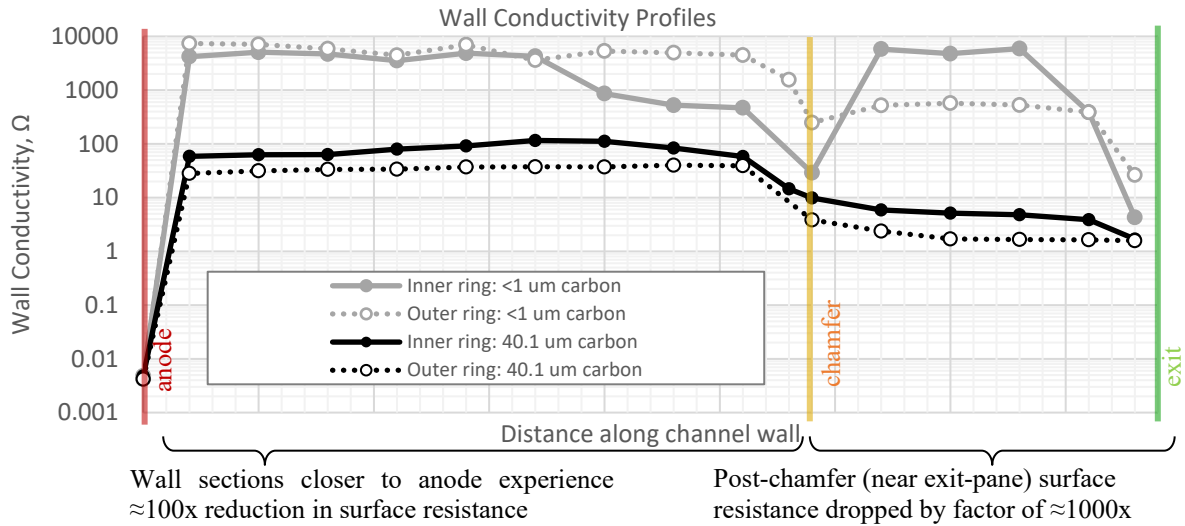


**Figure 38. Axially resolved discharge channel surface resistance measurements performed prior to Phase A testing (“light grey” traces for  $<1 \mu\text{m-C}$ ) and following Phase C testing (“black” traces for  $40 \mu\text{m-C}$ ). Inner channel measurement are plotted with solid lines while outer channel measurements use dashed lines.**

While the initial surface resistance decay during the carbon deposition is exponential, it is expected that the thicker layer of  $40 \mu\text{m}$  obtained at the conclusion of the ACDC testing behaves according to the linear theory presented in Eq. (3). Using this theory and with the surface resistance data from Figure 38, rough estimates of axially resolved deposited carbon layer thickness can be obtained as shown in Figure 39. The simple theory applied to obtain these estimates likely adds significant uncertainty and these data should be take only as qualitatively accurate.

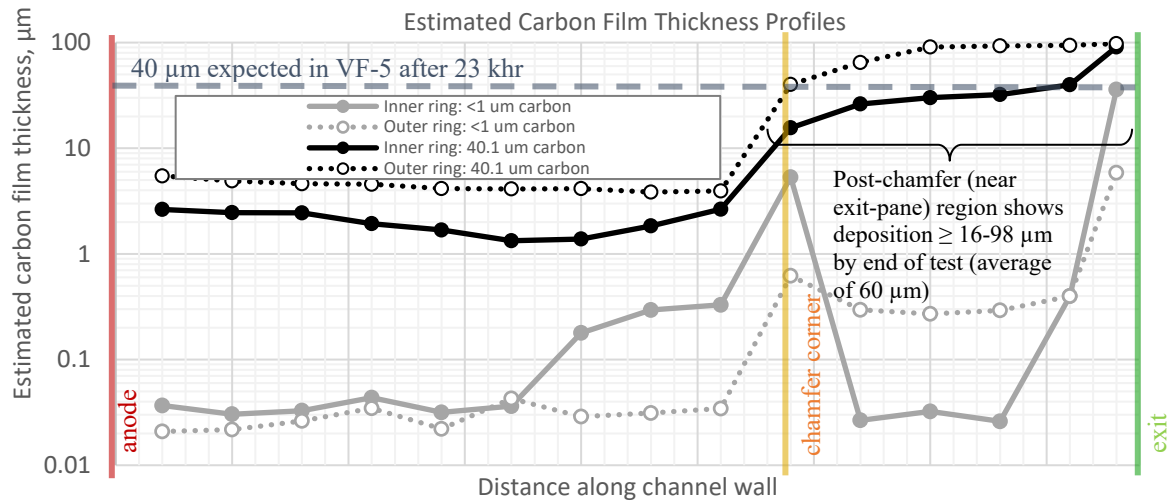


**Figure 39. Axially resolved estimates of deposited carbon layer thickness prior to Phase A testing (“light grey” traces for  $<1 \mu\text{m-C}$ ) and following Phase C testing (“black” traces for  $40 \mu\text{m-C}$ ). Inner channel data are plotted with solid lines while outer channel data are plotted with dashed lines. These estimates are based surface resistance measurements and the linear theory in Eq. (3).**

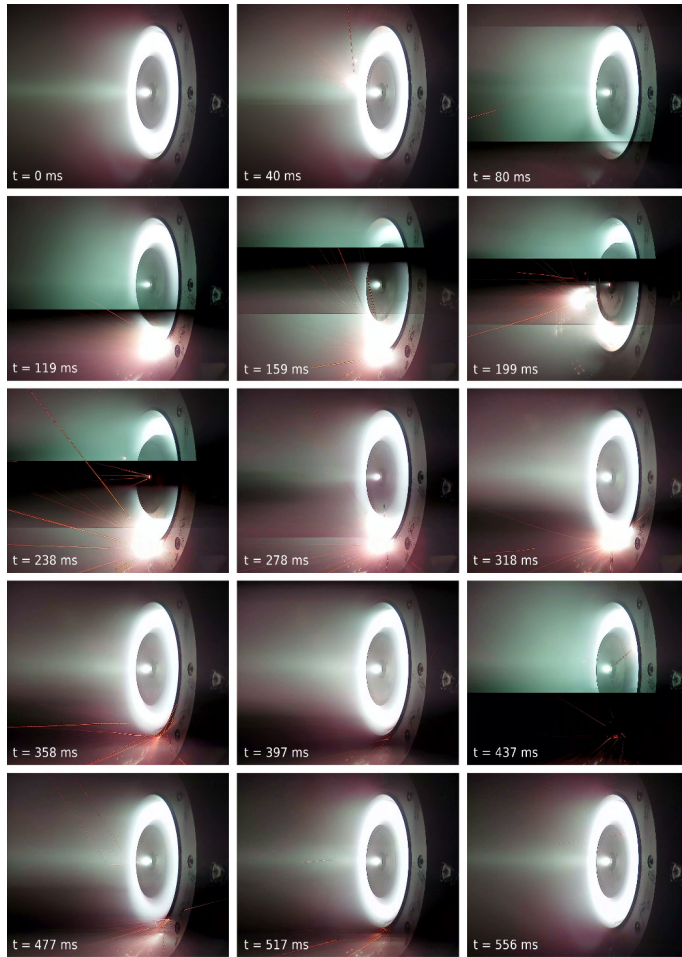


**Figure 40. Series of video frames capturing a spark event (horizontal banding from H.264 video compression).**

of the discharge channel and outer screen gap—a location that gravity would naturally concentrate flakes and particulate matter detaching from other portions of the thruster.

It was noticed that there was a relative abundance of flare and spark events during the first ~15 minutes of thruster operation from cold temperatures. Presumably, small bits of freshly spalled carbon (due to thermal coefficient mismatches) were being “cleared” during this time. The operation of the keeper enabled the thruster to remain lit throughout these events. To better understand the transients these events invoked upon the discharge power supplies, the oscilloscope was set to trigger on voltage dropouts during a cold thruster start. Figure 41 shows the measured transients during one of these spark event triggered sequences. It took several attempts to correctly capture unsaturated high-speed telemetry since the observed signal magnitudes of 400 A and >600 V were unexpected from a 300 V 20 A discharge. The full 100 ms window of scope data shows at least four spark events occurred in regular succession (one event every ~30 ms), which was related to the power supply transient load response specification of 2 ms for a 50% load change and other “discharging” and “recharging” time-constants discussed next. Zooming in on the first event, Figure 41(b) and Figure 42, the dropout for the nominal 300 V discharge voltage is seen to be associated with the first of three large current spikes to >200 A. The 25  $\mu\text{F}$  discharge filter capacitor drains quite rapidly due to the lack of a downstream thruster output ballast resistor, and is 1/e discharged in  $(25 \mu\text{F}) \cdot (0.17 \Omega) \approx 4 \mu\text{s}$ , using the approximate harness resistance. The discharge filter capacitor 1/e recharge time is set by the power supply side ballast resistor to  $(25 \mu\text{F}) \cdot (15 \Omega) = 380 \mu\text{s}$ . The power supply internal output capacitor was 152  $\mu\text{F}$  and 1/e discharges in 2.3 ms (hence the 2 ms response time specification) before folding from voltage control mode to current control mode. The effective 1/e decay time for current stored in the inductor is  $\tau = L/R = 220 \mu\text{s}$ . Thus, the following sequence of events were observed:

## H. Carbon Flares and Spark Events

Early in the deposition process during Phase B, brief carbon “flare” and “spark” events were observed visually (and in other telemetry) at regular intervals. Small single streamers or “flares” of carbon dust were observed about once every minute. Larger events—that initially led to unexpected shutdowns—occurred about once every 5.9 hours (average interval of first 10 unexpected shutdowns). This frequent rate of unexpected shutdowns prompted the activation of the cathode keeper (at a low-level 0.5 A) in an effort to sustain the plasma discharge during these transient events. *Indeed, after activating the keeper, no additional unexpected thruster shutdowns occurred throughout the remainder of the 413 hours of thruster operation.*

A video sequence of a larger carbon spark event is presented in Figure 40. This event involved multiple sparks at multiple locations near the outer edge of the discharge channel and the outer pole piece (at body or cathode potential).

Since the in-situ wall probe data showed that the carbon coated discharge channel floated up to the anode potential (see Eq. (8)) the full anode-to-cathode voltage potential existed in this gap where the sparking was localized. As magnetically shielded Hall thrusters, the H6MS and HERMeS thrusters share many similarities including a similar discharge channel edge to body gap sizes (see Figure 8). While the event in Figure 40 starts near the location of wall probes, the majority of the sparks (t = 119 ms to 517 ms) occur near the base

1. The first current spike (starting at  $t = -585 \mu\text{s}$ ) drains the discharge filter capacitor in 4  $\mu\text{s}$ .
2. The power supply starts recharging the discharge filter capacitor by slowly dropping its output voltage as the power supply internal output capacitor is discharged.
3. The flux in the inductor (and possibly thruster Hall current) as well as the power supply output capacitor sustain the first three 80  $\mu\text{s}$  wide  $>200 \text{ A}$  current spikes.
4. The third  $\sim 5 \text{ ms}$  wide 180 A current spike from 550  $\mu\text{s}$  to 5550  $\mu\text{s}$  puts the power supply into current control mode while the thruster (in conjunction with the keeper) enters a low voltage ( $\sim 100 \text{ V}$ ) glow discharge.
5. The power supply recovers (re-enters voltage control mode) once its internal capacitor, the discharge filter capacitor, the discharge filter inductor, and the Hall thruster Hall current are fully re-charged at about 20 ms.
6. The system inductance causes a slight voltage overshoot past 300 V that appears to initiate another spark event at 28 ms and the cycle repeats.

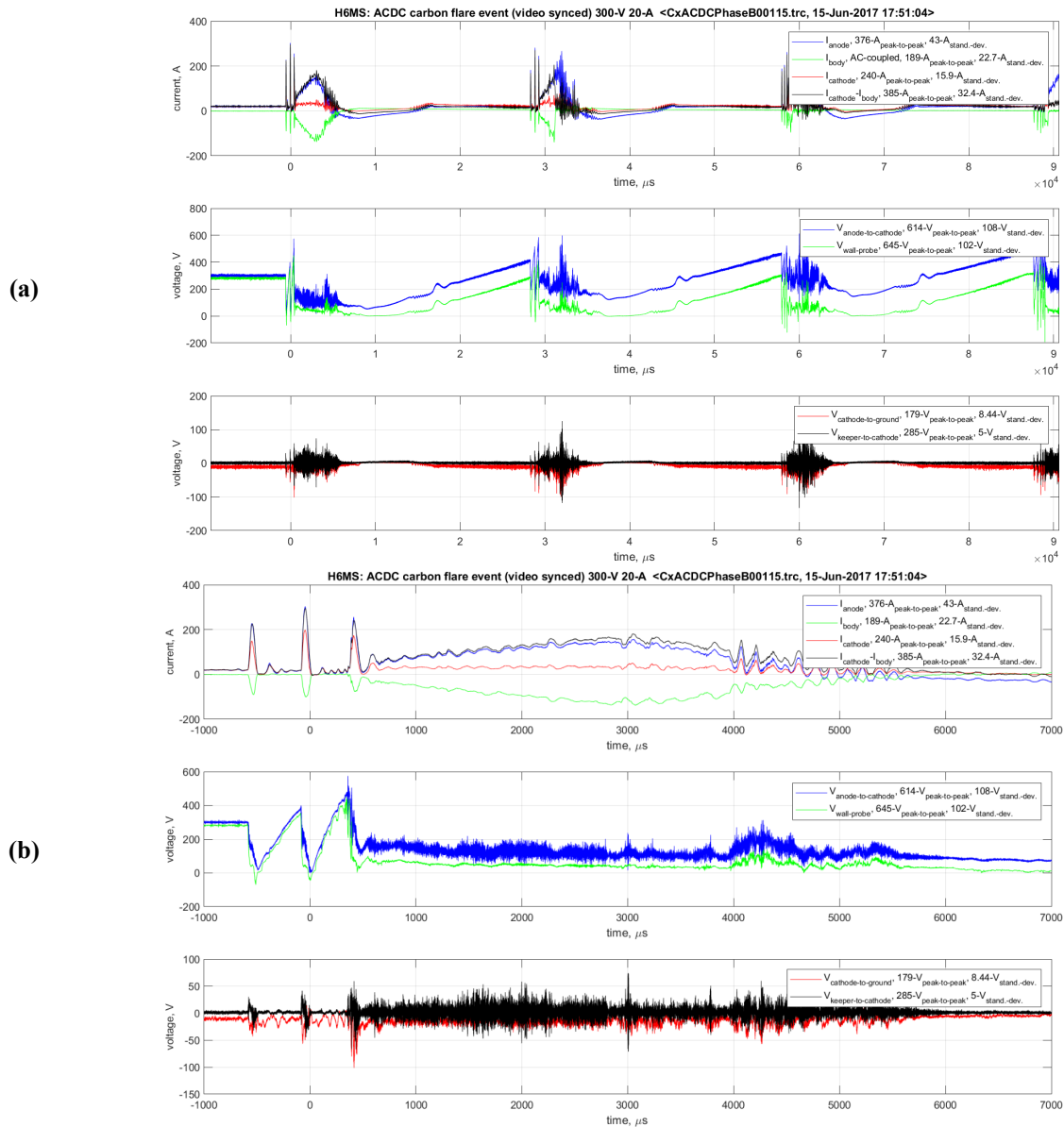


**Figure 41. High-speed discharge signals during spark event(s) showing +376 A and +614 V spikes in discharge current and voltage for the nominal 300 V 20 A operation point during which this event occurred. Upper set of traces (a) are for full 100 ms window of data collected while lower traces (b) are zoomed in view of 8 ms surrounding first packet of transient features.**

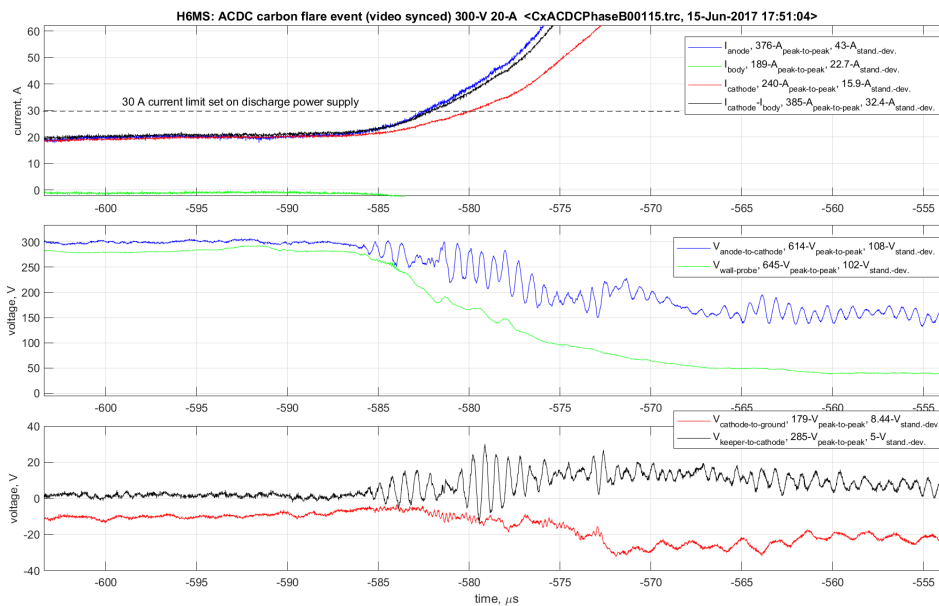


**Figure 42. Zoomed in view of Figure 41(b) show 50  $\mu\text{s}$  span surrounding the beginning of the discharge voltage dropout (as internal power supply output capacitor is drained) and current spike.**

The magnitude of these spark events is astonishing considering the large current amplitudes approaching 400 A (or nearly 20x the nominal discharge current) and they are even more impressive when considering the instantaneous power as presented in Figure 43. The instantaneous power is computed from the product of the high-speed discharge current and voltage telemetry sampled at the thruster (using voltage sense lines for the anode to cathode voltage).\*\*\* While the H6MS thruster operates at a nominal power level of 6 kW, spark events lead to a cascade of very high-power—greater than 100 kW—transient spikes. The highest power (>100 kW) features are approximately 100  $\mu\text{s}$  wide and correspond to 10 Joules of energy (or more). A zoomed-in view of the set of power spikes near the 60 ms spark is given in Figure 44. This view shows that the broader hump in power lasts about 3 ms with an average power of 32.7 kW; this feature consumes 94.9 Joules of energy.

\*\*\* The length of the cabling (approximately 9 meters) limits the bandwidth of these instantaneous power calculations to <5.8 MHz (quarter wavelength limit); thus, features narrower than 0.17  $\mu\text{s}$  are not accurate without further correction.

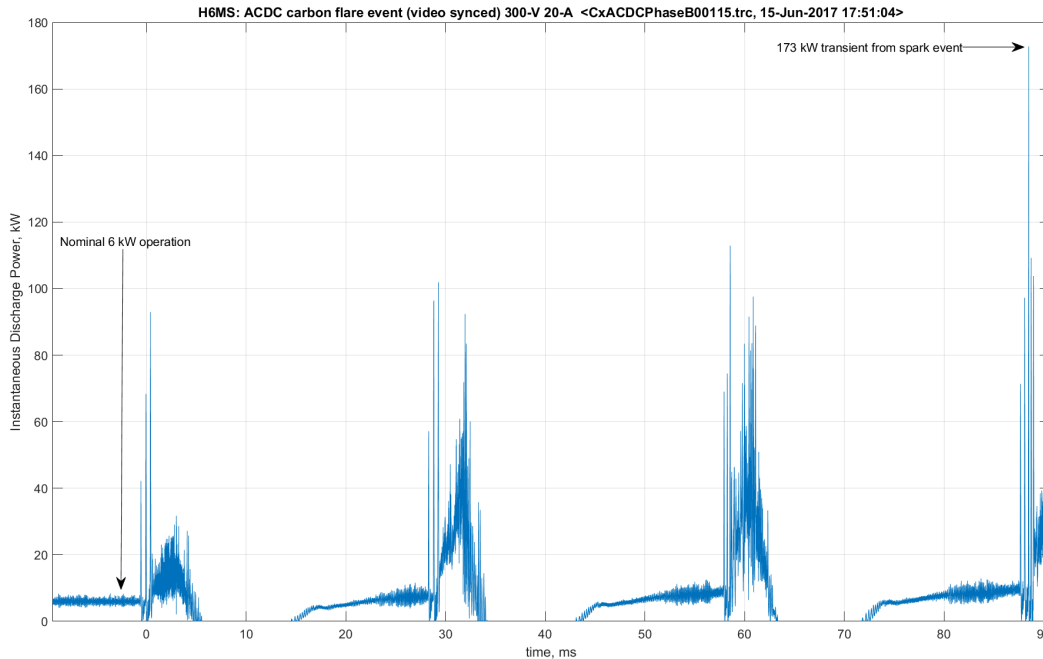


**Figure 43. Instantaneous thruster discharge power computed as the product of the time-resolved discharge current and voltage sense signals showing nominal 6 kW operation at  $t < 0$  ms and transient power spikes up to 173 kW (with peak width 108  $\mu$ s or energy  $\sim 19$  Joules/spike) during a large series of spark events.**

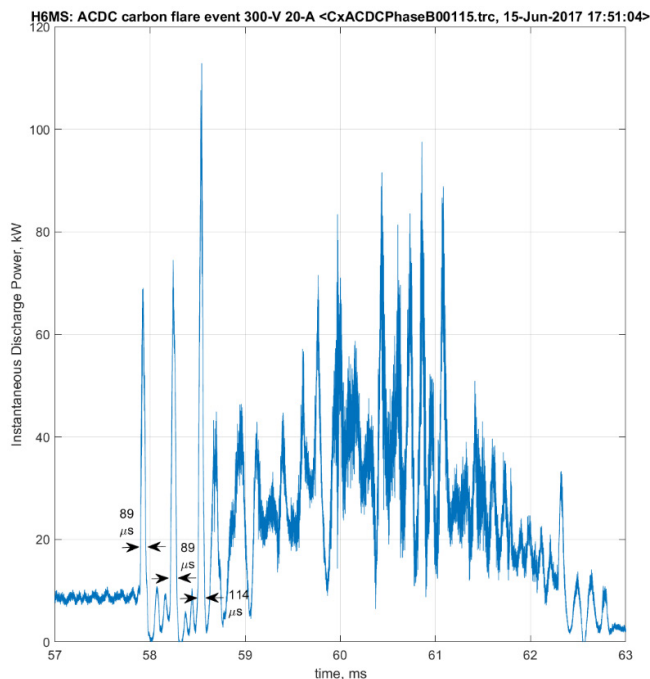


**Figure 44. Zoomed view of instantaneous thruster discharge power during series of spikes near 60 ms spark events.**

### I. Flake Vaporization via Spark Event Energy

Assuming the observed spark energies measured in the prior section led to direct Joule heating of thin carbon flakes, one may estimate the likelihood of flake ablation or vaporization. Using the enthalpy of formation of gaseous atoms from their standard state as,  $\Delta H_{carbon-vap.} = 716.7 \text{ kJ/mole}$  for carbon graphite [31], an arbitrary flake thickness of 40  $\mu\text{m}$  measuring 1 mm x 1 mm (typical for some flakes seen), the required energy for graphite flake vaporization/atomization is shown in Eq. (11).

Since most of the multitude of power spikes in the measured spark event instantaneous power plots deliver more energy than this, *it is thus probable that these sparks are indeed graphite flake "clearing" events.* Using Eq. (11), and the observed spark energies, flakes ranging from  $< 60 \mu\text{m}$  up to 575  $\mu\text{m}$  thick could have been plausibly vaporized by this mechanism.

$$\Delta E_{40-\mu\text{m flake-vaporization}} = \frac{\Delta H_{\text{carbon-vap.}}}{FM_c} (\rho_c h_{\text{flake}} l_{\text{flake}} w_{\text{flake}}) \quad (11)$$

$$\Delta E_{40-\mu\text{m flake-vaporization}} \approx 6 \text{ Joules}$$

**Table 4. Coefficients of thermal expansion for graphite and various thruster materials.**

Material	Coefficient of Thermal Expansion [m/(m·K)]
Graphite	$6.0 \times 10^{-6}$
Iron	$12 \times 10^{-6}$
Boron nitride	$1.0 \times 10^{-6}$

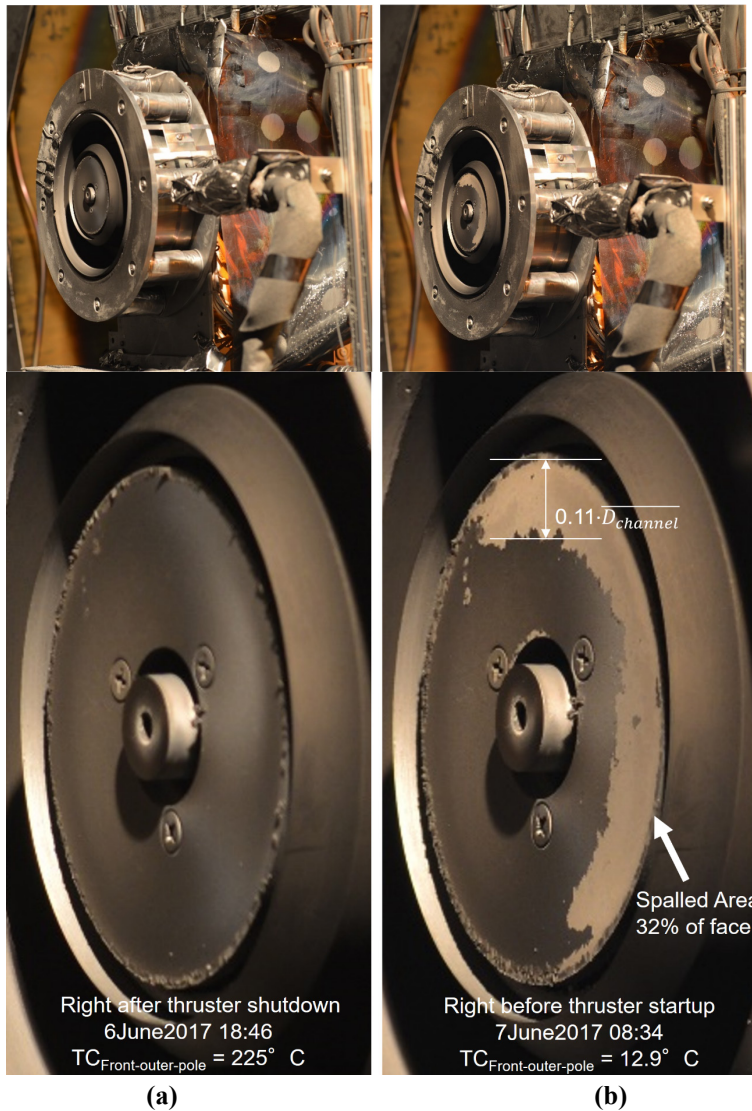


**Figure 45. Spalling observed as a result of thruster cooling off from (a) +225°C shortly after shutdown to (b) +12.9°C the following day (thruster was inactive and cooled overnight).**

piece thermally induced expansion and contraction (12 times larger than that of BN) led to routine shedding or spalling of deposited carbon layers.

### J. Carbon Spalling

Not all carbon flake detachment events led to instant fireworks, as thermal expansion driven carbon flake detachment or “spalling” was also observed while the thruster was unpowered. An example spalling event observed during an overnight thruster cool-down is shown in Figure 45. This figure compares a photograph taken shortly after shutdown (thruster outer pole = 225°C) to one taken 13.8 hours later when the thruster outer pole was 12.9°C. As the thruster cooled, approximately 1/3<sup>rd</sup> of the back-sputter deposited carbon coating the inner pole piece face spalled off. The coefficients of thermal expansion for graphite and relevant thruster materials are shown in Table 4.

It seems most likely that the large coefficient of thermal expansion for the iron pole piece (twice that of graphite) led to the spalling. The discharge channel wall material, Boron nitride has a very low coefficient of thermal expansion (six times lower than graphite) and similar large spalling events were not observed on the discharge channel walls. The surface properties of the boron nitride are much different than those of iron so it may be “sticker” to the graphite as well. Post-test examinations of the thruster did show that tiny carbon flakes could be chipped off the discharge channel revealing pristine white BN beneath.

Thus it appears that the thermally stable size of the discharge channel throughout large temperature changes helped prevent spalling from the BN; whereas the iron pole

It should be noted at this point that the uniquely accelerated rate of carbon back-sputter attained in the ACDC testing exceeded the typical measured rates of pole erosion experienced by all magnetically shielded Hall thrusters developed to date. Direct inner front pole face erosion measurements have been performed for the H6MS at 300 V and 20 A [26] and shown along with the ACDC deposition rates in Eq. (12).

$$\begin{aligned} \dot{h}_{\text{carbon-deposition-nominal-JPL}} &= 0.91 \mu\text{m}/\text{kh} \\ \dot{h}_{\text{carbon-deposition-ACDC-phaseB}} &= 98 \mu\text{m}/\text{kh} \\ \dot{h}_{\text{carbon-pole-erosion}} &= 25 - 71 \mu\text{m}/\text{kh} \end{aligned} \tag{12}$$

Thus,

$$\dot{h}_{\text{carbon-deposition-ACDC-phaseB}} > \dot{h}_{\text{carbon-pole-erosion}}$$

The simple observation that carbon was deposited onto the inner pole cover (and experiences occasional spalling) confirms the equality in Eq. (12). In this manner, the ACDC testing is a more rigorous test to stress the thruster, power electronics, and facility to the effects carbon back-sputter (since more locations are coated than in a non-accelerated test). However, the elimination of pole erosion in the ACDC testing prevents this campaign from understanding pole erosion failure modes.

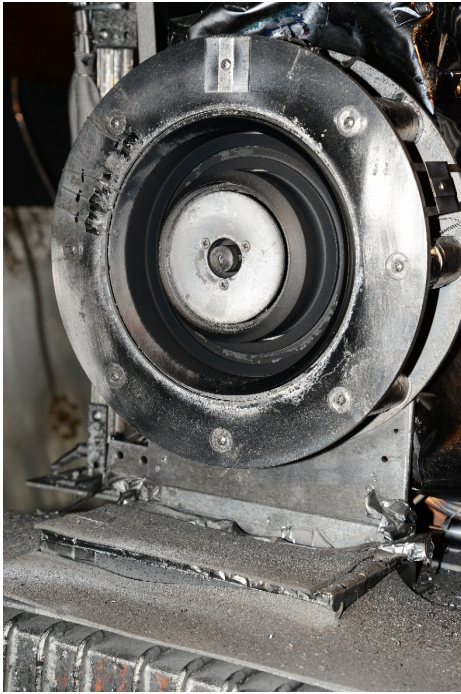


**Figure 46. Photograph of H6MS after final ACDC testing and 40  $\mu\text{m}$  of carbon deposition.**

electrical contact with the discharge channel carbon coating or if the wall probe cable(s) had independently shorted to the body (the fiberglass insulation was only rated for  $\sim 30$  V, not the 300 V operated at).

#### **K. Post-deposition Thruster Inspection & Short Causing Flake Resistance Measurements**

Upon conclusion of the final phase of ACDC testing, the H6MS thruster was carefully removed and relocated to the EP laboratory cleanroom (although the thruster was far from clean coated and covered in carbon layers, flakes, and dust). Detailed photographs were collected and several flakes were noted to exist between the discharge channel and the thruster body (see Figure 47 - Figure 51). Thus, before these and other sample flakes were collected (for analysis) the thruster was high-potential tested one additional time. As was suspected based on the observed flakes, a short of  $7.0 \text{ k}\Omega \pm 0.1 \text{ k}\Omega$  was found between the thruster body and the carbon coated discharge channel wall (average of multiple azimuthal locations using 4-wire sensing from channel surface to thruster body). This was not too surprising, since the thruster had been high-potential tested at the conclusion of the final Phase C of the ACDC testing while the thruster was still installed in the vacuum facility with the following wall probes resistances to body:  $R_{b2wp1} = 54.7 \text{ k}\Omega$ ,  $R_{b2wp2} = 3.0 \text{ k}\Omega$ ,  $R_{b2wp3} = 0.40 \text{ k}\Omega$ , and  $R_{b2wp4} = 45.8 \text{ k}\Omega$ . However, because the wall probes had acted erratically, it was not clear if they were in good



**Figure 47. (left) Close-up and location of “1:30” carbon flake found between discharge channel and outer screen (post-Phase C). (right) Close-up and location of “6:00” (“Ohio” shaped) carbon flake found between discharge channel and outer screen (post-Phase C).**

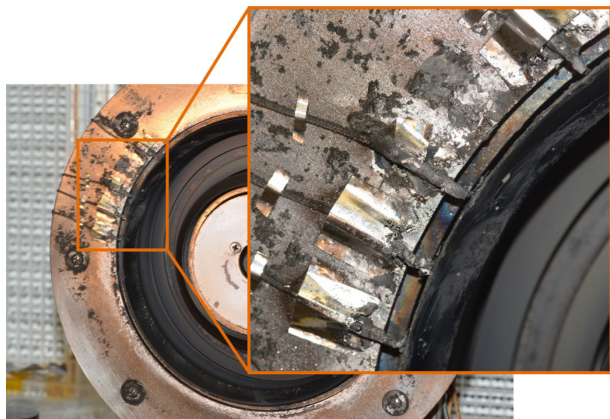


**Figure 48. Close-up of wall probes after 40 μm carbon deposition (post-Phase C).**

After photographing and high-potential testing the thruster, each of the preceding flakes/shorts (the 1:30 flake, the 6:00 “Ohio” flake, and the wall probes) were removed with the body to discharge channel wall resistance measured after each removal (final resistance was > 1.2 GΩ). By documenting the resistance after each flake/short was

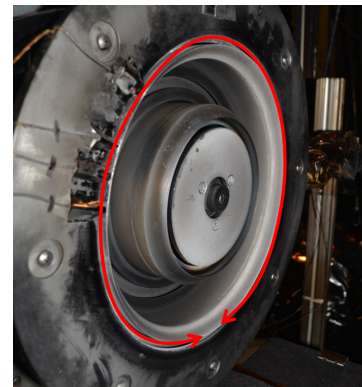


**Figure 49. Arrows showing where spalled carbon between outer screen and discharge will ultimately settle.**

removed, a system of three equations and three unknowns was readily solved for each flake/short resistance:

$$\begin{aligned}
 R_{1:30 \text{ flake}} &= 360 \text{ k}\Omega \pm 19 \text{ k}\Omega (\pm 3\sigma) \\
 R_{6:00 \text{ flake}} &= 9.1 \text{ k}\Omega \pm 0.1 \text{ k}\Omega (\pm 3\sigma) \\
 R_{\text{wallprobes2body}} &= 32.5 \text{ k}\Omega \pm 1.7 \text{ k}\Omega (\pm 3\sigma)
 \end{aligned}
 \tag{13}$$

The main source of the body to discharge channel shorting was the “Ohio” shaped flake at 6:00. This particular location is unique because it is where all spalled carbon material from the outer screen and discharge channel would naturally collect (via gravity) as illustrated in Figure 49. The HERMeS design has a similar gap here, but a lip is added to shadow-shield the screen and discharge channel gap.

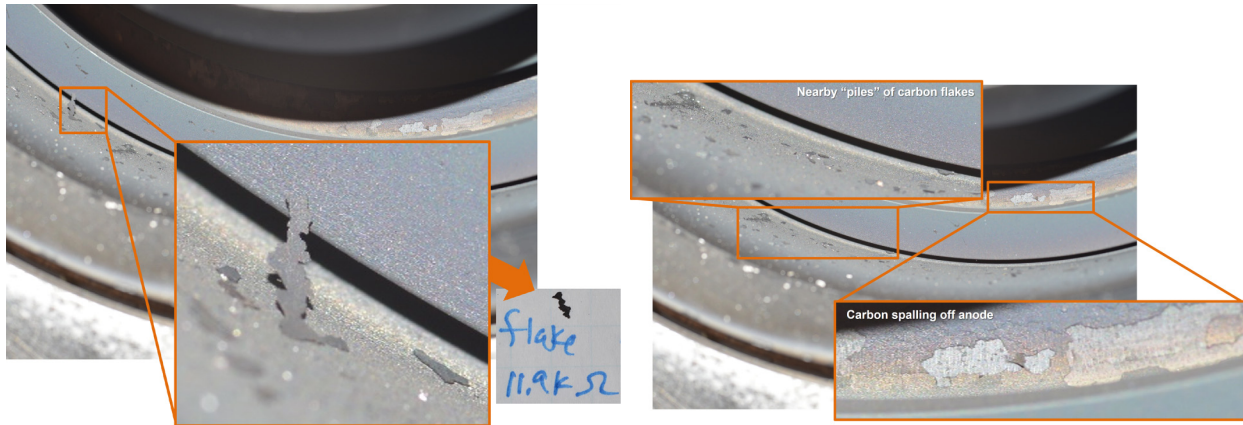


**Figure 50.** (left) Close-up and location of “7:30” (“Baja” California shaped) carbon flake found between discharge channel and anode (post-Phase C) that appeared after an attempted high-potential test between body and anode. (right) Piles of carbon flakes residing at base of the discharge channel and in close proximity to the anode along with spalling observed on the inner part of the anode flow distribution manifold (post-Phase C).

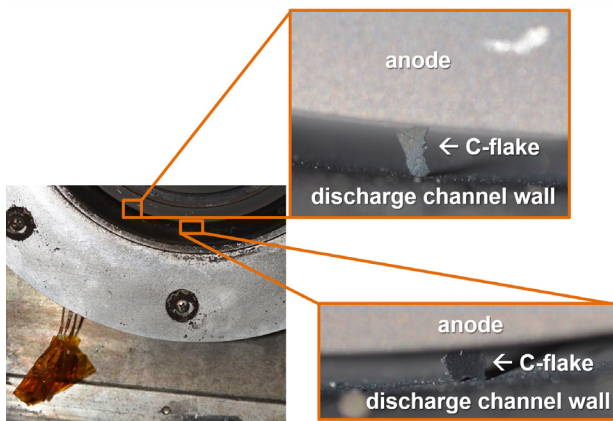


**Figure 51.** Close-ups and locations of additional carbon flakes found between discharge channel and anode (post-Phase C) that appeared after an attempted high-potential test between body and anode.

Another anomalous reading from the post-test examination high-potential test was that the anode was shorted to the body. During the attempted 1000 V test voltage a strange “fizzing” sound occurred and the test voltage quickly dropped to 6 V and an impedance of  $0\ \Omega$  to  $<3.8\ \text{k}\Omega$  (the high-potential impedance measurement mode cannot resolve low resistances properly). The high-potential impedance test prior to removing the thruster from the vacuum facility showed  $R_{\text{body2anode}} = 1.2\ \text{G}\Omega$ , so this short was unexpected. The three body to discharge channel shorts were now known to exist (and had not yet been removed) but the anode shorting was being caused by a “new” flake. Indeed, a new flake had appeared and was bridging the gap between the anode and the outer discharge channel wall (see Figure 50). This “Baja” California shaped carbon flake was not present in this location prior to the application of the 1000 V test voltage used for the impedance test—it was electrostatically lifted upwards from the “pile” (Figure 50) of nearby flakes! The flake was carefully removed

and collected for later profilometry analysis. Another high-potential impedance test was performed between the body and the anode with the same outcome: a “fizzing” sound, followed by test voltage drop from 1000 V to a few volts, and the appearance of new flakes shorting the anode to the discharge channel walls (Figure 51). These flakes were then manually removed and another high-potential impedance test was attempted only to repeat the creation of new shorts. This process was iterated about 8 times and eventually the “fizzing” sound continued for nearly 10 seconds while small white arcing events were seen to be occurring at the 6:00 base of the anode to discharge channel gap. After this prolonged “fizzing,” the test voltage climbed back up to 1000 V and the body to anode impedance gradually climbed from  $1.7\ \text{G}\Omega$  to  $5.7\ \text{G}\Omega$  while the 1 kV was applied for 15 minutes. While these anode to body shorts were surprising, they were really anode to discharge channel shorts (since the three body to discharge channel shorts were still in place) and this type of short would not have affected the thruster in-test since the plasma naturally sets the discharge channel to the anode voltage regardless. Additionally, the ability for the small high-potential test unit (maximum of 1 mA output current) to clear some of the smaller shorts was reassuring since it provides confidence that the much higher magnitude 400 A discharge spikes observed were capable of clearing larger flake-caused shorts.

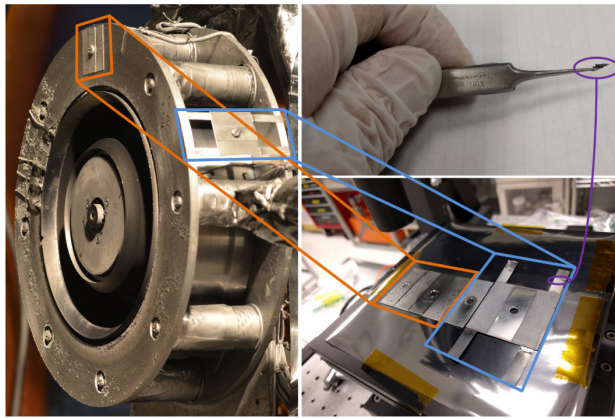


**Figure 52.** Photographs of axially facing and radially facing witness plate on thruster (left) and on profilometer scanning platform (lower-right). Several flakes of carbon detached from the witness plates during transfer from the thruster and a photo of one such flake is shown in the upper right (along with its approximate origin in the lower-right photo).

### L. Total Carbon Deposition and Detached Carbon Flake Profilometry Analysis

As the photographs in Section III.K exemplified, plenty of bits or flakes of carbon covered all flat surfaces, detaching via spalling events or through more dramatic flaring and sparking events. Witness plates attached to the thruster front face and side face were analyzed via profilometry measurements to determine the exact thickness of back-sputtered material at those on-thruster locations (Figure 52). While the QCM was used as the metric to determine when the full  $40\ \mu\text{m}$  of carbon back-sputter had been obtained, it was expected to receive slightly less back-sputter than the thruster due to the QCM location  $1.6$  mean channel diameters off-axis or  $0.58$  mean channel diameters outside the outer edge of the H6MS (Figure 15). In addition to the two witness plates, several samples of flakes were collected from the thruster and also evaluated using profilometry measurements.

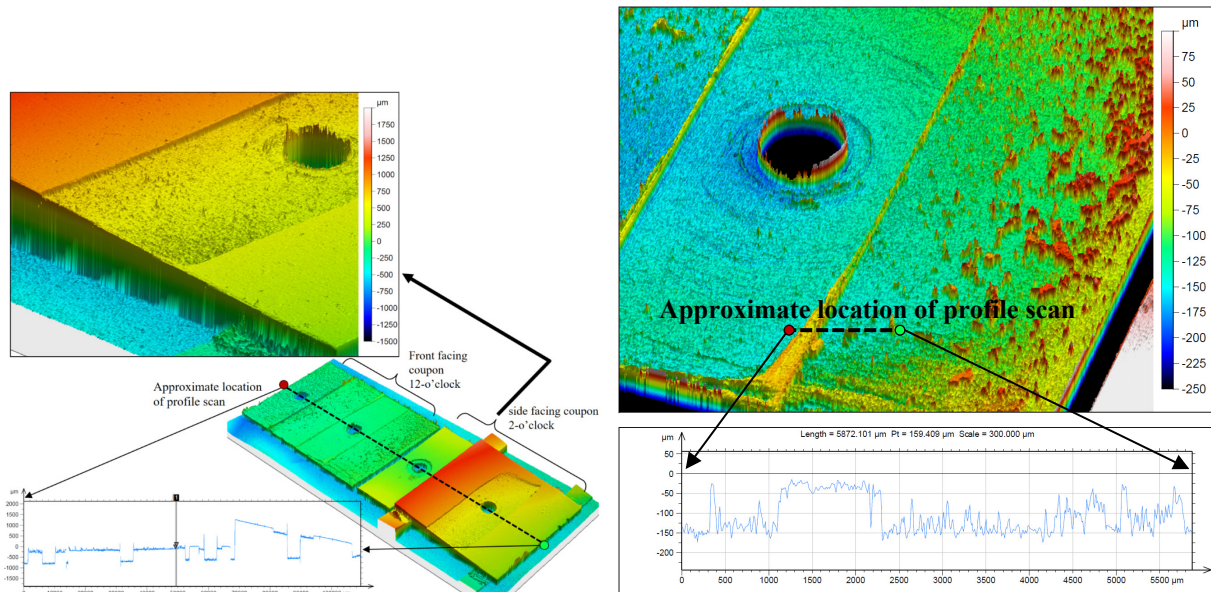


**Figure 53.** (Left) axially and radially facing witness plates profilometry scan data. Central band about bolt hole of square plates were covered with rectangular masks (to the left) during deposition, other areas were exposed showing features  $50\text{-}150\ \mu\text{m}$  in height. (Right) axially facing witness plate profilometry scan. Central column about bolt hole was covered with a mask during deposition, other areas were exposed showing features  $50\text{-}150\ \mu\text{m}$  in height.

The scanned topographies of the two witness plates (including removed masks) are shown in Figure 53. The side or radial plate provided the clearest measurement of thickness of the back-sputter deposited carbon as seen in the cliffs surrounding where the masked cover resided in. Using the linear profile scan shown, a carbon deposition ridge height of  $158\ \mu\text{m}$  is measured on the radially positioned witness plate. The axially positioned witness plate detail and linear profile are also shown in Figure 53 but the carbon deposition is “spotty,” and it is presumed that much of the carbon

that was coating this surface spalled off during thermal expansion changes experiences during testing. Both witness plates were fabricated from stainless steel shim plate which has a very similar coefficient of thermal expansion to iron. Even with the less distinct cliff feature, the remaining islands of carbon deposition show approximate thicknesses of 50-175  $\mu\text{m}$ . It is not understood why the carbon deposition on the radially facing witness plate remained intact while that on the axially facing plate mostly spalled off. Both plates were likely experiencing similar thermal transients<sup>†††</sup> and both received a similar amount of back sputtered carbon. Prior to ACDC testing, the fabricated witness plates were scanned using the same setup and they showed flatness to within a few  $\mu\text{m}$ .

During the post ACDC testing thruster examination, several flakes were collected and profilometry measurements were performed to help characterize the sizes of these “naturally” detached carbon flakes. These flakes were not “chiseled” or scraped off the thruster, they were all simply picked up using tweezers or brushes and are representative of flakes that did or could lead to shorts between various surfaces in-operation.

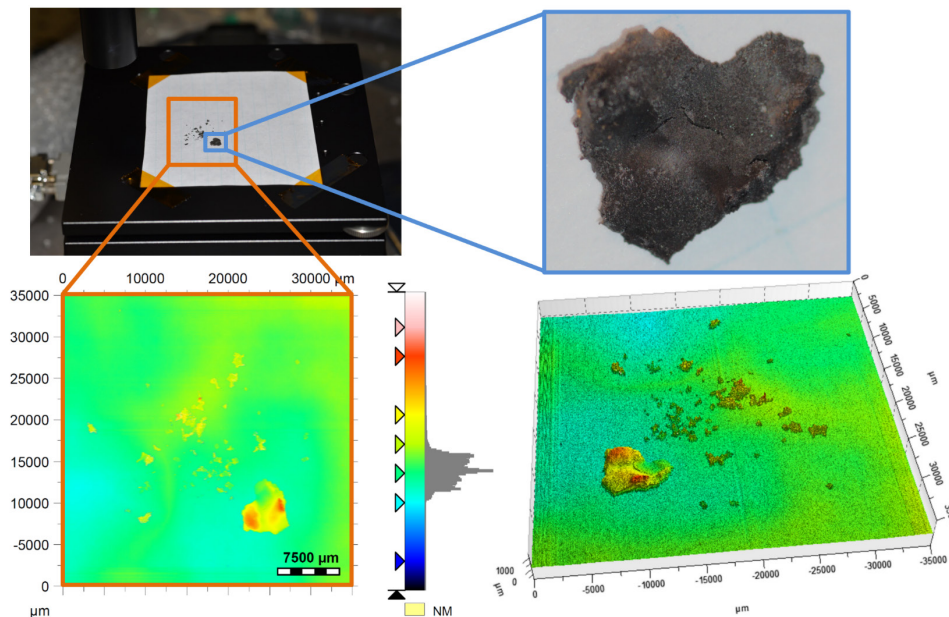


**Figure 54. Collected flakes from H6MS including “Ohio” shaped flake (upper right photo) that caused a 9.1 k $\Omega$  body to discharge channel short between the outer screen and the carbon coated channel wall.**

In Figure 54, a collection of flakes from the H6MS are shown photographically and as raw profilometry measured topographies. The “Ohio” flake (responsible for a 9.1 k $\Omega$  body to discharge channel short in the screen to channel gap) is part of this grouping and a close-up of this flake reveals a multilayered structure. A more complete profilometry analysis is shown in Figure 55 where surface height is shown to range from 0  $\mu\text{m}$  (the floor) to nearly 1000  $\mu\text{m}$ . However, this is not necessarily the thickness of the flake because the bottom of the flake is not flat. The “Ohio” flake was unique from the other flakes in that it was notably thicker than all the other flakes analyzed and it has noticeable mass while moving with tweezers. It may be that this particular flake has an origin not related to the ACDC direct deposition but became lodged where found during transport from the chamber. Regardless of the origin of the “Ohio” flake, it appears to have regions on the order of 500  $\mu\text{m}$  thick based on the upper peak height variations in the linear profile scan shown.

<sup>†††</sup> While the temperature of the radial plate was unknown, it was spot welded to the front pole piece where the other witness plate resided.

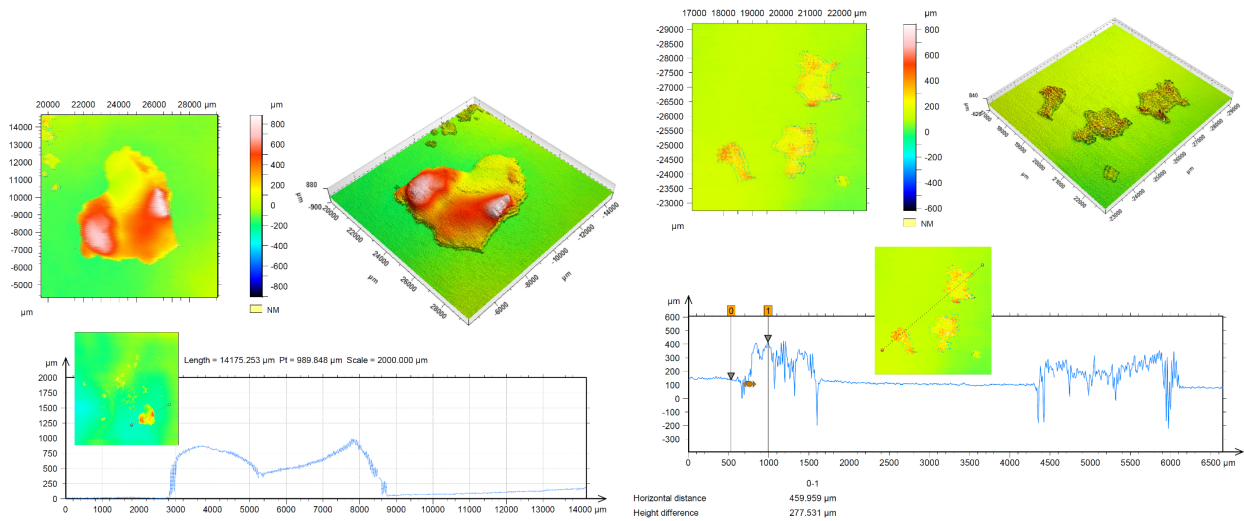


**Figure 55. Detailed profilometry analysis for the (left) “Ohio” flake and for the (right) quartet of flakes collected from the H6MS after the 40  $\mu\text{m}$  deposition.**

A quartet of flakes from the same collection in Figure 54 is analyzed in Figure 55. These particular flakes are most representative of all the detached flakes, since larger flakes were too fragile and rarely survived falling off the thruster without shattering. The linear profile scan shows varying carbon thicknesses ranging from about 175-250  $\mu\text{m}$  (average near 200  $\mu\text{m}$ ). While not as thick as the “Ohio” flake, these flakes are still much thicker than expected. Again, there is some uncertainty in the thickness, but because they are closer to the thickness of carbon measured by the witness plates, these carbon flake thicknesses are probably good estimates of the back-sputtered carbon received by the thruster.

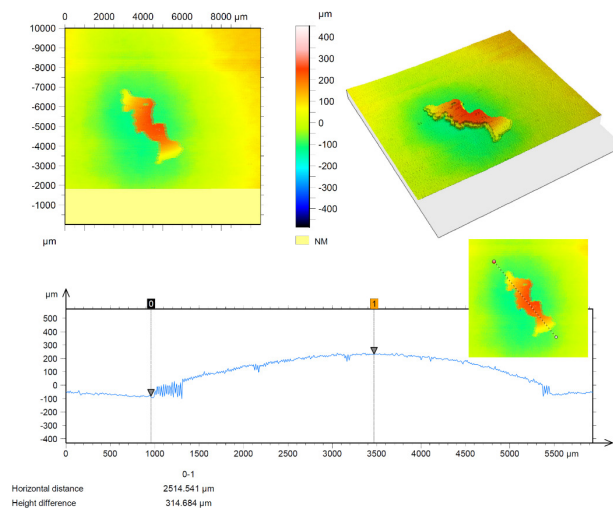


**Figure 56. Profilometry analysis of the “Baja” California shaped flake.**

However, the “Baja” flake most likely spalled or detached from the anode; Figure 50 showed visual evidence of this for other flakes.

#### IV. Thruster Performance and Characteristics Before and After Carbon Deposition

##### A. H6MS Thrust with 0- $\mu\text{m}$ and 40- $\mu\text{m}$ (23,000 h Equivalent) Carbon Deposition

The initial JPL performance measurements of the H6MS thruster were conducted in 2012 [8] and then repeated in throughout the ACDC testing. The early and last portions of the ACDC testing (Phases A and C) were performed with

the nominal configuration of JPL Owens facility using the same thrust stand as the 2012 testing and these data are collected in Table 5 and Figure 57 (red and black traces).

**Table 5. TDU-2 Performance measurements pre-RV/TVAC and post-RV/TVAC along with boron nitride and borosilicate comparison.**

	H6MS	Thrust	Efficiency (tot.)	Mass flowrate	$V_{\text{cathode2gnd}}$	Pressure	$I_a$ (A <sub>pk2pk</sub> )	$I_a$ (A <sub>std.dev.</sub> )
AIAA 2012-3788	300-V 6-kW	384.2 mN ±4 mN	62.4%	18.35 mg/s +7%CFF	-9.2 V	1.6×10 <sup>-5</sup> torr-Xe	-	1.0
ACDC: 0.0 μm-C	300-V 6-kW	380.8 mN ±4 mN	61.3%	18.30 mg/s +7%CFF	-9.8 V	1.1×10 <sup>-5</sup> torr-Xe	7.3	1.0
ACDC: 40.1 μm-C	300-V 6-kW	380.9 mN ±4 mN	61.8%	18.14 mg/s +7%CFF	-10.2 V	1.2×10 <sup>-5</sup> torr-Xe	12.6	1.5
ACDC: 0.0 μm-C	300-V 9-kW	549.5mN ±6 mN	62.4%	24.99 mg/s +7%CFF	-8.8 V	1.5×10 <sup>-5</sup> torr-Xe	13.6	1.6
ACDC: 40.1 μm-C	300-V 9-kW	547.8 mN ±6 mN	62.4%	24.84 mg/s +7%CFF	-8.8 V	1.5×10 <sup>-5</sup> torr-Xe	20.3	2.6

The key takeaway from these results is that the performance of the magnetically shielded H6MS is invariant with time and with back-sputtered carbon. This is quite remarkable since all thruster life tests to date (STP-100 [32], SPT-140 [33], BPT-4000/XR-5 [34]) have shown thrust losses typically ≥5% during life wear tests. Mass flowrates, chamber pressures, and cathode-to-ground voltages also remained unvaried before and after the carbon deposition. Changes in anode current discharge oscillation were observed however, and shall be discussed in a following section. While within the uncertainty, the H6MS data from 2012 shows slightly higher thrust (+3.4 mN or ≈+1%) compared to the ACDC baseline data, and this difference is attributed to use of the cathode-tied body configuration for the ACDC testing (the 2012 data had the body grounded). Experiments comparing the performance of different Hall thruster body electrical configurations have shown a very slight thrust loss on the order of ≈1% or less [35] for the cathode-tied body configuration compared to the body grounded configuration.

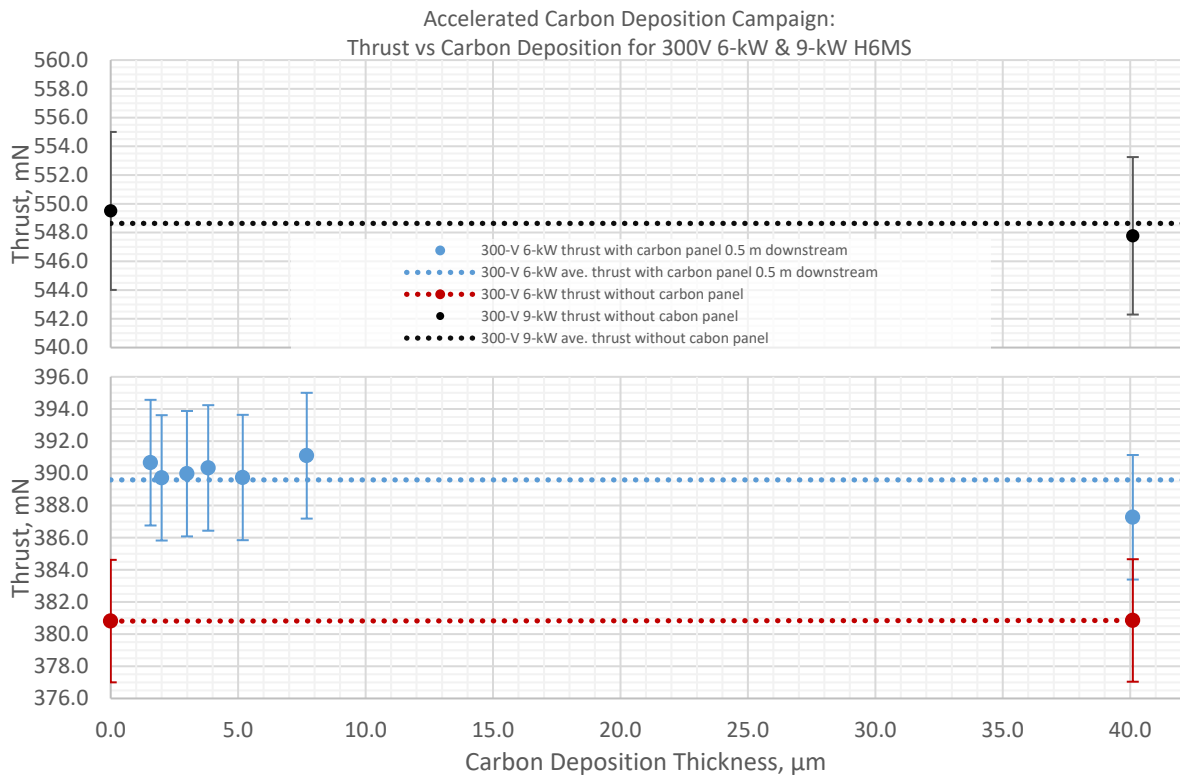


**Figure 57. Invariance in thrust measured throughout ACDC test campaign for 9 kW (upper plot, “black”) and 6 kW operation (lower plot) with (“blue”) and without (“red”) carbon blast panel.**

Performance data was also collected during the deposition process (Phase B) while the 1 m by 1 m graphite blast panel was 0.5 m downstream from the H6MS. It was expected that the thrust would be higher in this configuration due to increases localized re-ingestion of neutralized xenon propellant. As seen in Figure 57 (blue data), a small +8.8 mN (+2.3%) thrust increase was observed with the presence of the graphite panel. Despite this small change, the thrust throughout the deposition remains unchanged (within the uncertainty). A blown fuse on the thrust stand inclinometer motor prevented the acquisition of additional thrust data between 7.5 μm and 40 μm while the graphite panel was

installed, but this was repaired for the final measurement. During Phase B, the thruster was operated only at 300-V 6-kW (disregarding brief thruster startups).

Throughout the entire ACDC testing a total xenon propellant throughput of 28.3 kg was exhausted during the 413 hours of H6MS operation. This test effectively accelerated an equivalent HERMeS life qualification test of 23,000 hours that would have consumed nearly 4 years of chamber time >\$3M LN<sub>2</sub> usage and >\$4M Xe (using the 2017 market rate of \$14/liter). This accelerated test expended only about \$150k in consumables, saving both significant amounts of time as well as funding.

**Table 6. Propellant throughput, total energy, and total impulse of conducted ACDC test as well as equivalent 23,000 h life qualification test for the HERMeS thruster.**

Test Condition	Total discharge time (hours)	Total Xenon Throughput (kg)	Total Energy (MWh)	Total Impulse (MN)
ACDC testing	413.1	28.3	2.48	0.57
Equivalent non-accelerated test	23,000*	1771*	288*	50.0*

\*Equivalent values for life qualification testing of the AEPS HERMeS thruster at 12.5 kW in VF-5

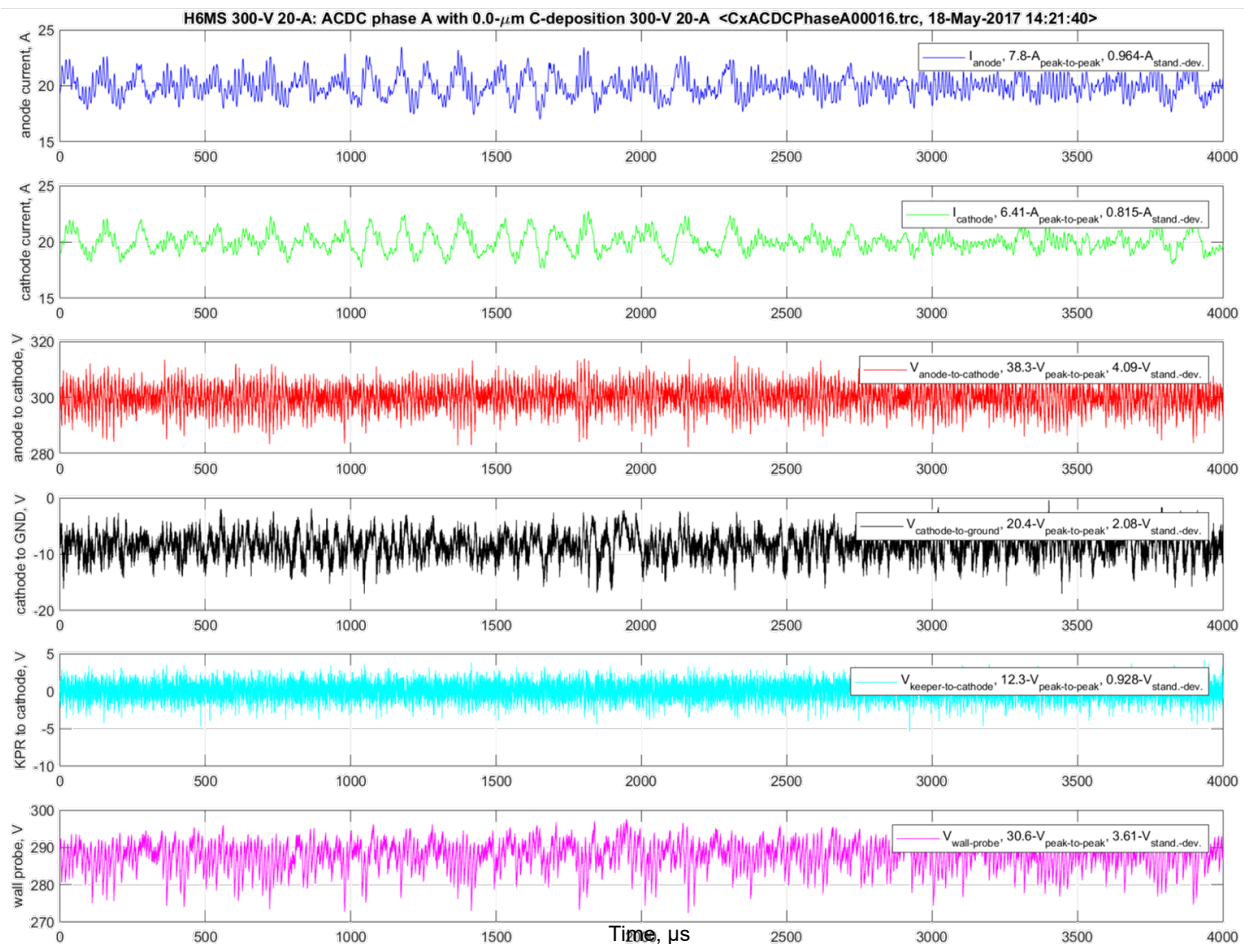


**Figure 58. Time-domain plots of all high-speed scope telemetry collected during Phase A H6MS baseline test at 300 V 20 A. Data taken in nominal Owens configuration (no graphite blast panel) before the 40  $\mu\text{m}$  carbon deposition.**

## B. Discharge Fluctuations: 0- $\mu\text{m}$ & 40- $\mu\text{m}$ (23,000 h Equiv.) Carbon Deposition

The baseline configuration tested (Phases A and C) H6MS discharge fluctuations showed an increase of about 50% with the presence of 40- $\mu\text{m}$  carbon deposition. However, as seen in the time-domain traces in Figure 58 and Figure 59, the qualitative discharge waveform characteristics remained unchanged.

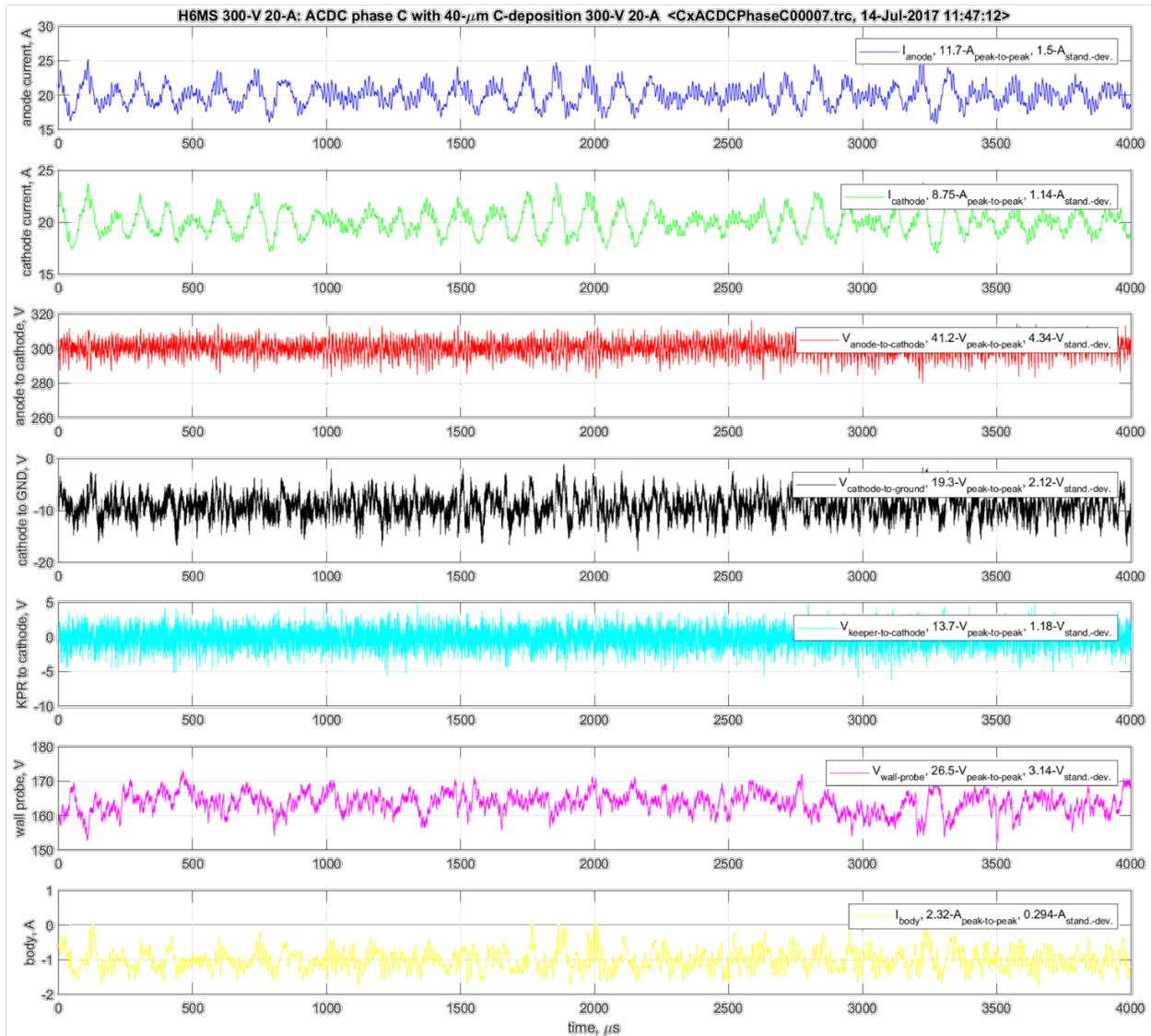


**Figure 59. Time-domain plots of all high-speed scope telemetry collected during Phase C H6MS re-baseline test at 300 V 20 A. Data taken in nominal Owens configuration (no graphite blast panel) after the 40  $\mu\text{m}$  carbon deposition.**

The anode, cathode, and body discharge current signals peak-to-peak and standard deviation variations are collected in Table 7 for Phases A, B (start), and C. The peak-to-peak fluctuation metrics are important from a system standpoint because they bound the magnitudes of the signals. However the peak-to-peak is computed as simply peak-to-peak  $\equiv$  maximum[ $signal(t)$ ] – minimum[ $signal(t)$ ], where  $signal(t)$  is a scope trace with 10 million samples. Thus, the peak-to-peak variation has poor statistical accuracy since it is based on just 2 points out of 10 million. The standard deviation ( $\sigma$ ), on the other hand, is based on all sample points and provides a more accurate statistical metric since 98% of all the data is within  $\pm 2\sigma$ . The anode current peak-to-peak and standard deviation amplitudes increase from 0- $\mu\text{m}$  (Phase A) to 40- $\mu\text{m}$  (Phase C) by +49% and +56% respectively. H6MS data from Ref. [8] is also included in Table 7 which was obtained in the body grounded configuration. Prior experiments comparing body grounded and

body tied to cathode configurations show minimal oscillation standard deviation amplitude changes <1% [35], thus warranting inclusion in the table.

**Table 7. H6MS anode, cathode, and body discharge current peak-to-peak and standard deviation variations throughout all test phases.**

ACDC phase	thruster on-time (h)	QCM thickness ( $\mu\text{m}$ )	Discharge Voltage (V)	Discharge Current (A)	$I_{\text{anode}}$ ( $A_{\text{pk2pk}}$ )	$I_{\text{cathode}}$ ( $A_{\text{pk2pk}}$ )	$I_{\text{body}}$ ( $A_{\text{pk2pk}}$ )	$I_{\text{anode}}$ ( $A_{\text{stand.dev.}}$ )	$I_{\text{cathode}}$ ( $A_{\text{stand.dev.}}$ )	$I_{\text{body}}$ ( $A_{\text{stand.dev.}}$ )
AIAA 2012-3788	0	0	300	20	NA	NA	NA	1	NA	NA
A	0	0	300	20	7.92	6.93	NA	0.98	0.83	NA
B	2.3	0.2	300	20	12.9	10.38	2.38	1.68	1.35	0.28
C	411	40.1	300	20	11.9	8.97	2.47	1.51	1.14	0.30
A	0	0	300	30	13	11.6	NA	1.62	1.48	NA
C	413	40.1	300	30	19.1	14.6	3.92	2.56	2.02	0.48
Percent increase of current oscillations phase A to C:					49%	28%		56%	37%	
Percent increase of current oscillations phase A to B:					63%	50%		71%	63%	

Phase B data—obtained during the accelerated deposition with the graphite panel 0.5 m downstream from the thruster—is also included to demonstrate the perturbing effect this panel had on the thruster dynamics. The close proximity of the graphite panel effected +63% and +71% increases in the anode current peak-to-peak and standard deviation amplitudes respectively. As was discussed already, the discharge oscillation signals remained relatively invariant throughout the entire 0- $\mu\text{m}$  to 40- $\mu\text{m}$  deposition process of Phase B showing, +3% and -6% changes in the anode current peak-to-peak and standard deviation amplitudes respectively.

### C. Discharge Oscillation Spectra: 0- $\mu\text{m}$ & 40- $\mu\text{m}$ (23,000 h Equiv.) Carbon Deposition

Approximately 274 full sets of scope traces were acquired throughout the ACDC testing (>30 GB)—too many to present in this report. However, the crucial question on whether the baseline configuration discharge oscillation spectra changed in any systematic way due to the 40  $\mu\text{m}$  of carbon deposition is addressed in Figure 60 (anode and cathode currents) and Figure 61 (anode-to-cathode, cathode-to-ground, and keeper-to-cathode voltages).

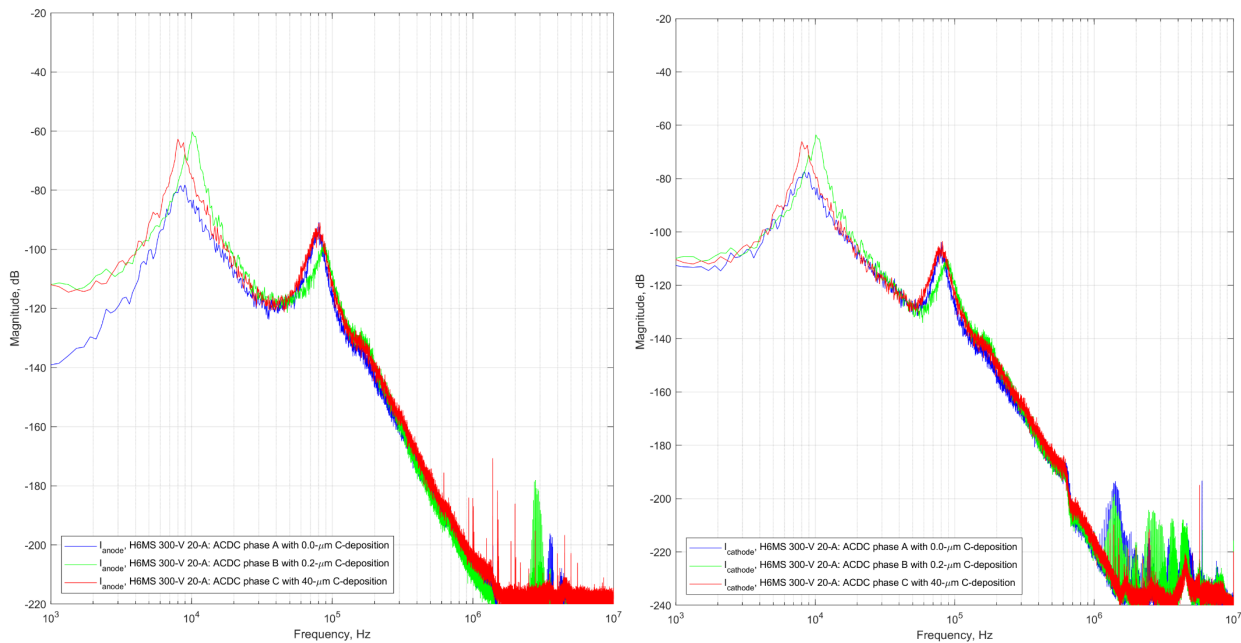


**Figure 60. Power spectral density plots of the (left) anode current,  $I_a$ , and (right) cathode current,  $I_c$ , before (Phase A baseline in “blue”) and after (Phase C baseline in “red”) the 40  $\mu\text{m}$  carbon deposition. The off-nominal Phase B setup with the graphite blast panel 0.5 m downstream is also included (in “green”).**

While amplitude differences do exist in these data, the major spectral features including dominant mode frequencies and widths are invariant for nominal Phase A (“blue” traces) and C (“red” traces) H6MS operation with 0  $\mu\text{m}$  and 40  $\mu\text{m}$  of back-sputtered carbon. The spectra at the beginning (only 0.2  $\mu\text{m}$ ) of Phase B (“green” traces, with the graphite panel 0.5 m downstream) are also included since the increased oscillation amplitudes are curiously similar to that observed in the Phase C baseline test with 40  $\mu\text{m}$  of carbon. These Phase B data are known to be highly perturbed by the presence of the graphite plate, and were not expected to match the nominal chamber configuration data without the plate. Yet current oscillation amplitudes of the dominant low-frequency mode at the start of Phase B is closely matched to the Phase C baseline test with 40  $\mu\text{m}$  of carbon. While the frequencies of the dominant two modes of 8.4 kHz and 80.1 kHz are invariant from Phase A (0  $\mu\text{m}$ ) to C (40  $\mu\text{m}$ ), the early Phase B (0.2  $\mu\text{m}$ ) data with the graphite panel show shifts to 10.3 kHz and 87.9 kHz (+16% average increase).

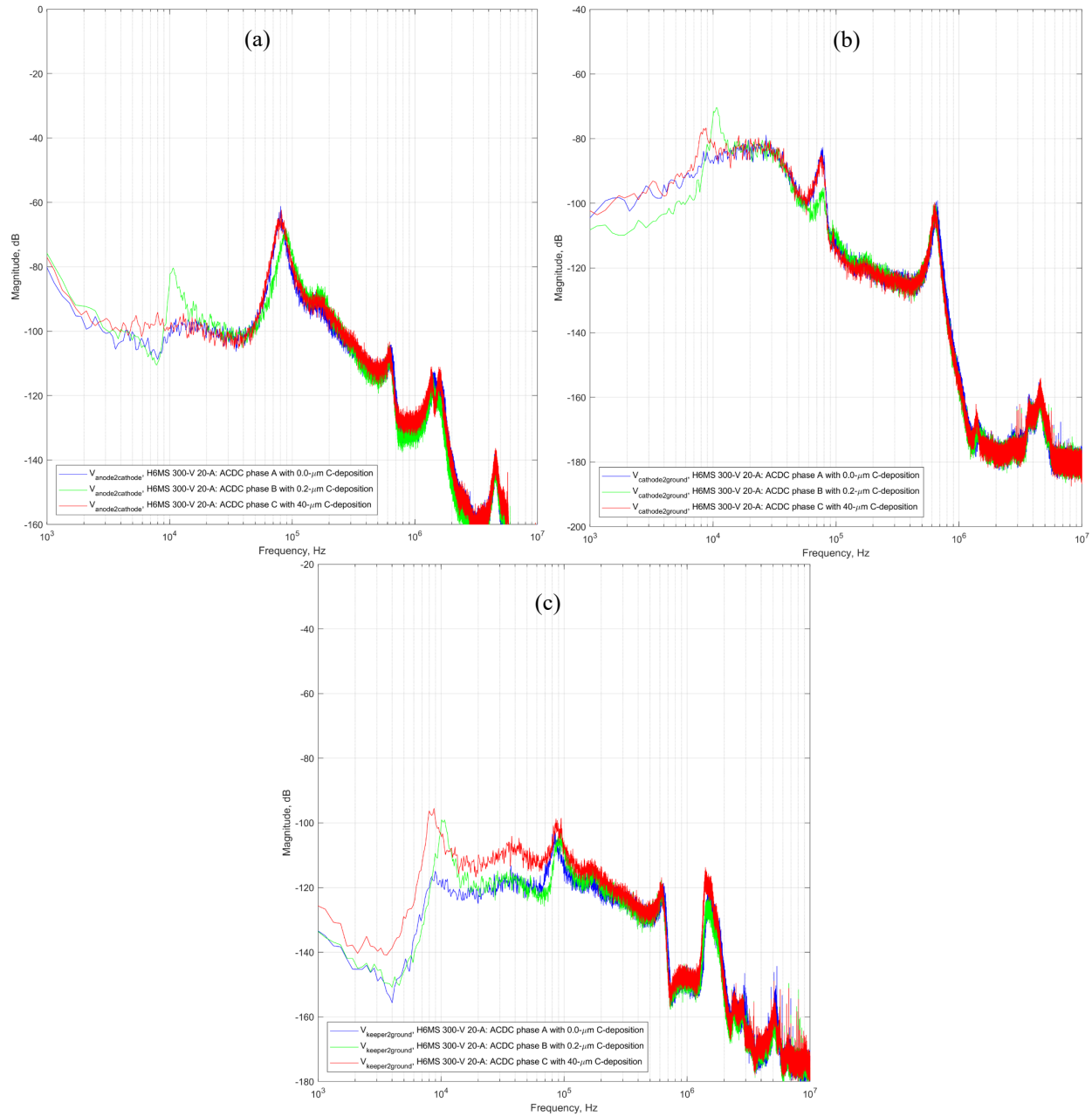


**Figure 61. Power spectral density plots of the (a) anode to cathode voltage,  $V_{a2c}$ , (b) cathode to ground voltage,  $V_{c2g}$ , and (c) keeper to cathode voltage,  $V_{k2c}$ , before (Phase A baseline in “blue”) and after (Phase C baseline in “red”) the 40  $\mu\text{m}$  carbon deposition. The off-nominal Phase B setup with the graphite blast panel 0.5 m downstream is also included (in “green”).**

In an effort to validate the Phase A oscillation data (since the low-frequency mode amplitude is out-of-family with the Phase B and C data), previously published H6MS data [8] is plotted along with ACDC data from Phases A, B, and C in Figure 62. While the power spectral density plots in Figure 62 are normalized differently (vertical axes units do not match), the scales are both linear (not log-scaled as the prior figures) and the frequencies of the two dominant modes are the same in Ref. [8], Phase A, and Phase B. Returning to Table 7 briefly shows that the standard deviation of the anode discharge current is also the same between Ref. [8] and Phase A. Thus, the Phase A oscillation data are fully consistent with the beginning of life (BOL) H6MS.

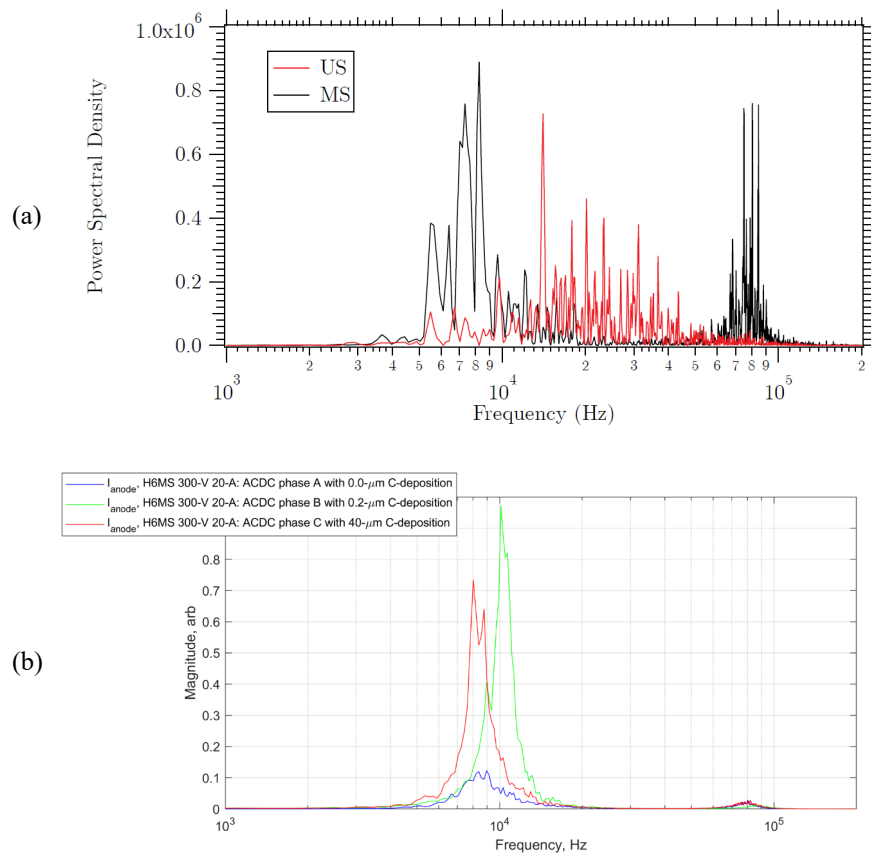


**Figure 62. Non-log scaled power spectral density plots of the anode current,  $I_a$ , for the (a) H6MS 300-V 20-A (“black” trace labeled “MS” taken from Ref. [8]) and for the (b) ACDC test before (Phase A baseline in “blue”) and after (Phase C baseline in “red”) the 40  $\mu\text{m}$  carbon deposition. Note: while the vertical axes are both linearly scaled, the units are both arbitrary and do not match.**

deposition process shows negligible peak temperature changes. Figure 63 presents a zoomed view of these data. Ignoring the startup and shutdown transient thermal features, the steady state temperatures for the TS-A, TS-B, TS-C, and TS-D thermocouples are  $349^\circ\text{C} \pm 1.5^\circ\text{C}$ ,  $226.5^\circ\text{C} \pm 1^\circ\text{C}$ ,  $328^\circ\text{C} \pm 0.5^\circ\text{C}$ , and  $249^\circ\text{C} \pm 1.5^\circ\text{C}$  respectively. Given that the thermocouple accuracy is  $\pm 3^\circ\text{C}$ , the observed peak temperatures are thus invariant (within the uncertainty). Other tests with magnetically shielded Hall thrusters have shown temperature decreases (up to  $20^\circ\text{C}$ ) as carbon coated the thruster surfaces (increased emissivity) [5]. However, the ACDC testing began with a small amount of pre-existing carbon deposition ( $<1 \mu\text{m}$ ) that likely had already significantly changed the beginning-of-test emissivity with future carbon deposition effecting negligible additional emissivity changes.

#### D. Oscillation Mode Locking During Operation with Graphite Target (Phase B)

The presence of the graphite blast target in Phase B was fully expected to affect thrust and other operational parameters. However, the increased oscillations during Phase B deposition remained approximately invariant (see Figure 28 - Figure 31) from 0.2  $\mu\text{m}$  to 40  $\mu\text{m}$ , thus it was unexpected that upon removal of the graphite panel, the oscillation amplitudes remained “locked” at this higher amplitude. In this manner, the presence of the graphite panel has by some unknown means permanently “conditioned” the thruster dynamics to oscillate at the higher amplitudes with or without the panel.

#### E. H6MS Thermal Variations with 0- $\mu\text{m}$ & 40- $\mu\text{m}$ (23,000 h Equiv.) Carbon Deposition

Throughout all phases, only four thruster mounted thermocouples were installed and monitored and a closer look at these data throughout the carbon

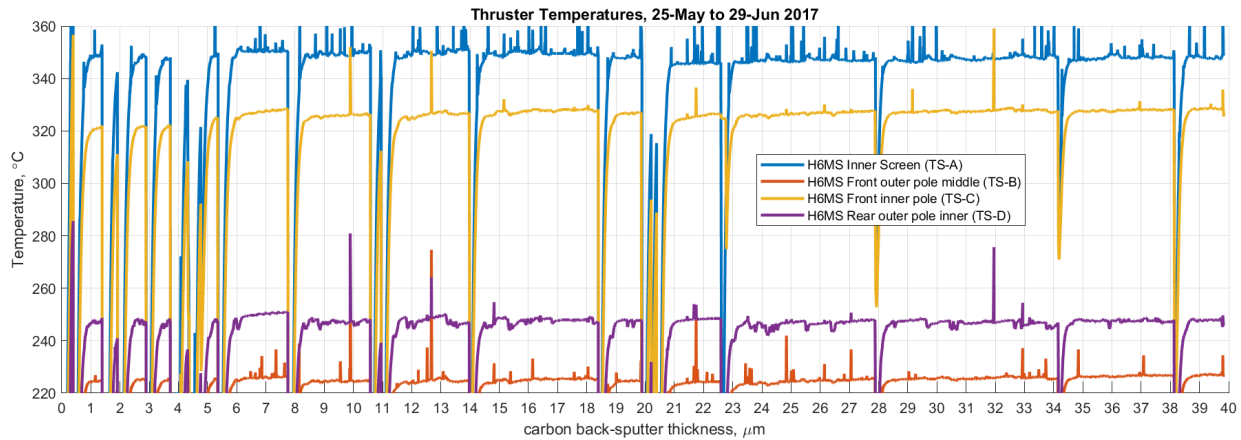


**Figure 63. Invariance in peak thruster temperatures throughout the carbon deposition process.**

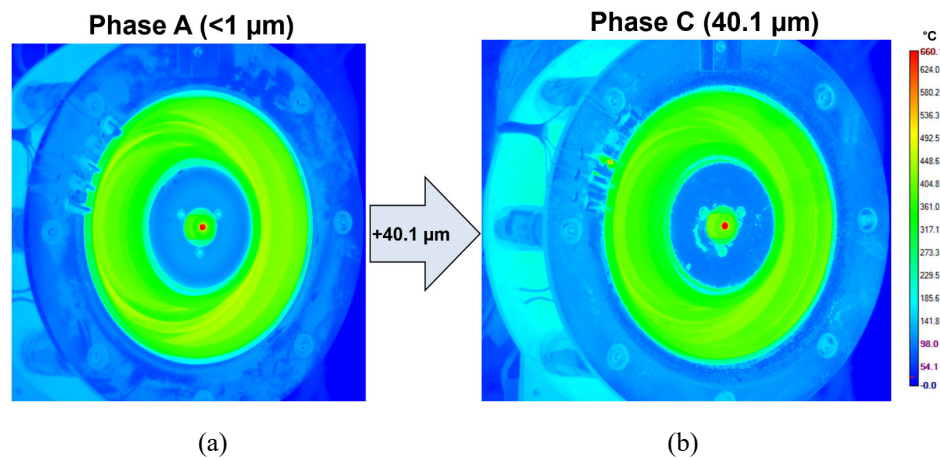
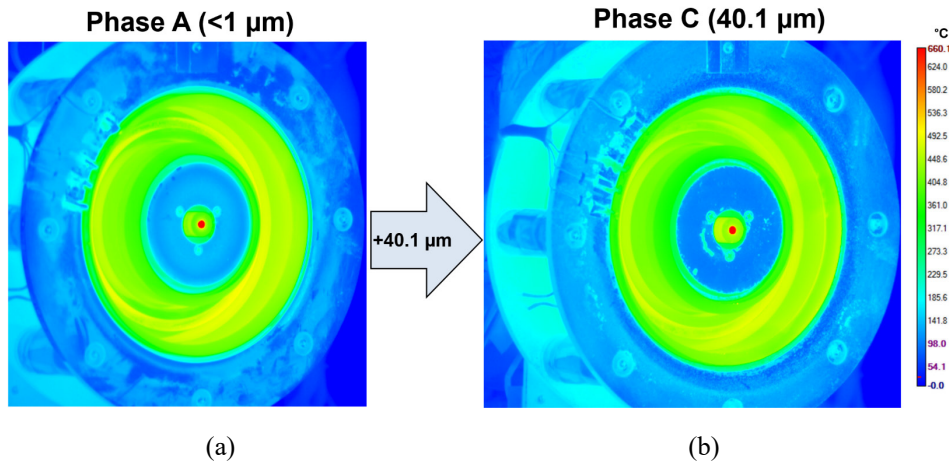


**Figure 64. Thermal camera images for H6MS at 300 V 6 kW with (a) <1 μm and with (b) 40.1 μm carbon deposition. Color scales matched and default emissivity of 0.95 is assumed for all surfaces but thruster not at complete thermal equilibrium.**

During the baseline testing in Phases A and C, thermal camera images were acquired and these images are compared in Figure 64 for 300 V 6 kW and in Figure 65 for 300 V 9 kW operation. These data were collected in a consistent manner after 2-3 hours of thruster operation in each case, but complete thermal equilibrium (which takes > 3 hours to establish) was not obtained. Even so, it is expected that the discharge channel walls

and anode were at (or near) their thermal equilibrium temperatures. These surfaces show a subtle decrease in temperature (e.g. slightly “greener”), but it is likely within the uncertainty of the thermal imaging data which has significant uncertainty due to the unknown surface emittances. Given this large overall uncertainty, it is remarkable that the temperatures are virtually unchanged before and after the 40 μm of carbon deposition.



### F. Thrust Vector Startup Profiles: 0- $\mu\text{m}$ & 40- $\mu\text{m}$ (23,000 h Equiv.) Carbon Deposition

During the phase A and C baseline performance testing thrust vector data were collected that show minimal  $\pm 0.2^\circ$  angle deviations for both cases (Figure 66). These thrust vector data are plotted with respect to the initial thrust vector angle since absolute alignment of the thruster to the thruster vector probe was not performed. The

**Figure 65. Thermal camera images for H6MS at 300 V 9 kW with (a)  $<1 \mu\text{m}$  and with (b)  $40.1 \mu\text{m}$  carbon deposition. Color scales matched and default emissivity of 0.95 is assumed for all surfaces but thruster not at complete thermal equilibrium.**

observed variations are significantly more stable than the NSTAR [28] and T6 [23] ion thrusters which both exhibit excursions just over  $1^\circ$  while throttling up to full power and approaching thermal equilibrium. The observed H6MS thrust vector variations are also less than the STP-140 flight system requirement of  $\pm 0.75^\circ$  [33].

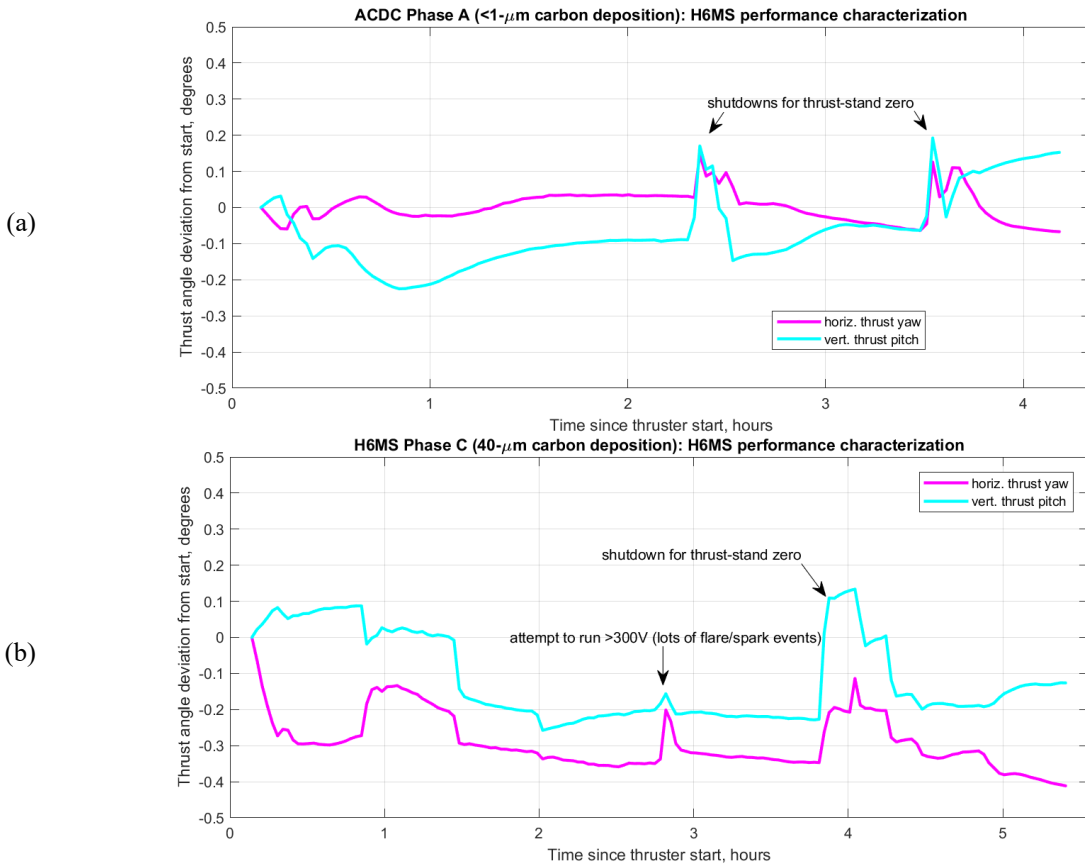


**Figure 66. Thrust vector variation during (a) Phase A pre-deposition and (b) Phase C post-deposition testing of the H6MS. Data presented as difference from initial thrust vector angle for each case (absolute alignment was not performed).**

Overall, the 40  $\mu\text{m}$  of back-sputtered carbon appears to have no effect on the range of thrust vector angle variance since  $\pm 0.2^\circ$  is observed in both pre-deposition and post-deposition operation. Some testing notes have been added to the traces in Figure 66, but in both the pre- and post-deposition cases, the first few hours of thruster operation are a throttled set of bakeout conditions that lead to the various small thrust vector angle jumps early on.

### G. Visual H6MS Changes: 0- $\mu\text{m}$ & 40- $\mu\text{m}$ (23,000 h Equivalent) Carbon Deposition

While a progression of photographs has already been presented, a side-by-side comparison of the H6MS thruster prior to the start of the ACDC Phase A baseline test is compared to the post Phase C baseline test in Figure 67. The once smooth iron front poles became visually roughened by multitudes of small spalled features and the light grey discharge channel (with  $<1 \mu\text{m}$  carbon) became pitch black with  $>40 \mu\text{m}$  of back sputtered carbon. All exposed Kapton surfaces have changed from amber to shiny grey and thousands of flakes of spalled carbon littered the base of the thruster mount and facility floor.

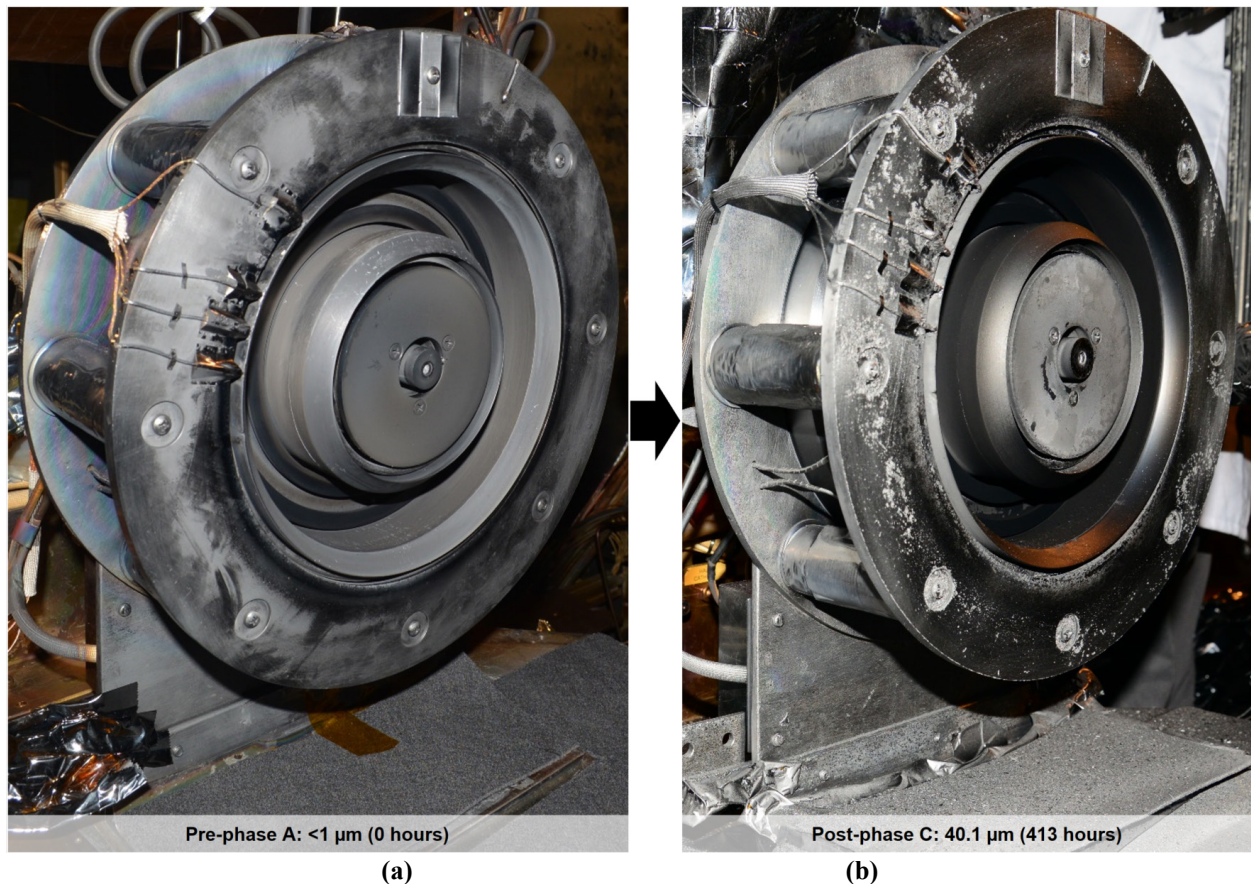


**Figure 67. (a) Photograph of H6MS prior to start to ACDC Phase A testing compared to (b) photograph of H6MS after the successful completion of all ACDC test phases with  $>40 \mu\text{m}$  of carbon deposition.**

## V. Conclusion

The H6MS thruster successfully endured  $>40 \mu\text{m}$  of accelerated carbon back-sputter deposition—equivalent to a 23,000 hour life qualification test—and maintained nominal operational characteristics. Thrust and specific impulse remained invariant throughout the 0 to  $40 \mu\text{m}$  of carbon deposition as did many other operational parameters including thruster steady state temperatures. The boron nitride discharge channel walls became effectively conductive with  $36 \Omega$  average surface resistance after the  $40 \mu\text{m}$  of carbon deposition. Thruster body high-voltage isolation resistances underwent dramatic drops from  $\text{G}\Omega$  values to  $\text{k}\Omega$  values with no measurable loss in performance. While a +46% increase in the amplitude of high-speed discharge current oscillations was observed between the 0 and  $40 \mu\text{m}$  carbon back-sputter conditions, the overall features of the oscillation spectra (peak locations and widths) remained invariant.

Numerous carbon flare and spark events were observed that led to unexpected thruster shutdowns at an approximate rate of 5.9 hours<sub>ACDC</sub>/shutdown which corresponds to 14 days/shutdown in a non-accelerated life qualification test. After the first dozen unexpected shutdowns, the cathode keeper was activated at all times to keep the thruster lit throughout these spark events. Evaluation of the time-resolved discharge signals showed that these spark events were sufficiently energetic (400 A<sub>peak</sub> or 173 kW<sub>peak</sub>) to fully vaporize  $\leq 4\text{r}0\ \mu\text{m}$  to 575  $\mu\text{m}$  thick carbon flakes. Analysis of carbon flakes collected at the conclusion of the testing revealed a wide distribution of flake thicknesses ranging from 50  $\mu\text{m}$  to 500  $\mu\text{m}$ . Large scale spalling events were also observed while the thruster underwent large thermal transients (e.g. after shutdown), suggesting that the mismatch in the coefficients of thermal expansion for the carbon and iron pole pieces are the main carbon spalling mechanism. The success of this test campaign suggests that a magnetically shielded thruster—such as the HERMeS thruster—may undergo a full life qualification test of 23,000 hours in a ground test facility with no significant negative impacts from facility back-sputtered carbon expected to coat the thruster throughout the test.

## VI. Acknowledgments

The research described in this paper was carried out at the Jet Propulsion Laboratory, California Institute of Technology, under a contract with the National Aeronautics and Space Administration.

## VII. References

- [1] Brophy, J. R., Polk, J. E., Randolph, T. M., and Dankanich, J. W., “Lifetime Qualification of Electric Thrusters for Deep-Space Missions,” AIAA 2008-5184, 44th AIAA/ASME/SAE/ASEE Joint Propulsion Conference, Hartford, CT, July 2008.
- [2] Sengupta, A., Brophy, J., Anderson, J., Garner, C., Banks, B., and Groh, K., “An Overview of the Results from the 30,000 Hr Life Test of Deep Space 1 Flight Spare Ion Engine,” AIAA 2004-3608, 40th AIAA/ASME/SAE/ASEE Joint Propulsion Conference and Exhibit, July 11, 2004.
- [3] de Groh, K., Banks, B., and Karniotis, C., “NSTAR Extended Life Test Discharge Chamber Flake Analyses,” AIAA 2004-3612, 40th AIAA/ASME/SAE/ASEE Joint Propulsion Conference and Exhibit, July 11, 2004.
- [4] Williams, J., Johnson, M., and Williams, D., “Differential Sputtering Behavior of Pyrolytic Graphite and Carbon-Carbon Composite Under Xenon Bombardment,” AIAA 2004-3788, 40th AIAA/ASME/SAE/ASEE Joint Propulsion Conference and Exhibit, July 11, 2004.
- [5] Hofer, R. R., Jorns, B. A., Polk, J. E., Mikellides, I. G., and Snyder, J. S., “Wear test of a magnetically shielded Hall thruster at 3000 seconds specific impulse,” IEPC-2013-033, Presented at the 33rd International Electric Propulsion Conference, The George Washington University, Washington, D. C., October 6, 2013.
- [6] Yim, J., “A survey of xenon ion sputter yield data and fits relevant to electric propulsion spacecraft integration,” IEPC-2017-060, The 35th International Electric Propulsion Conference, Georgia Institute of Technology, Atlanta, Georgia, USA, October 8, 2017.
- [7] Yim, J. T., “Computational Modeling of Hall Thruster Channel Wall Erosion,” Ph.D. Dissertation, The University of Michigan, 2008.
- [8] Hofer, R., Goebel, D., Mikellides, I., and Katz, I., “Design of a Laboratory Hall Thruster with Magnetically Shielded Channel Walls, Phase II: Experiments,” AIAA 2012-3788, 48th AIAA/ASME/SAE/ASEE Joint Propulsion Conference & Exhibit, Atlanta, GA, August 30, 2012.
- [9] Haas, J. M., Hofer, R. R., Brown, D. L., Reid, B. M., and Gallimore, A. D., “Design of the H6 Hall Thruster for High Thrust/Power Investigation,” Presented at the 54th JANNAF Propulsion Meeting, Denver, Colorado, May 14, 2007.
- [10] Mikellides, I., Katz, I., Hofer, R., and Goebel, D., “Design of a Laboratory Hall Thruster with Magnetically Shielded Channel Walls, Phase III: Comparison of Theory with Experiment,” AIAA 2012-3789, 48th AIAA/ASME/SAE/ASEE Joint Propulsion Conference & Exhibit, Atlanta, GA, August 30, 2012.
- [11] Goebel, D. M., Watkins, R. M., and Jameson, K. K., “LaB6 Hollow Cathodes for Ion and Hall Thrusters,” *Journal of Propulsion and Power*, vol. 23, May 2007, pp. 552–558.
- [12] Polk, J. E., Lobbia, R. B., Barriault, A., Chaplin, V. H., Lopez-Ortega, A., and Mikellides, I. G., “Inner Front Pole Erosion in the 12.5 kW HERMeS Hall Thruster Over a Range of Operating Conditions,” IEPC-2017-409, 35th International Electric Propulsion Conference, Atlanta, Georgia, October 8, 2017.
- [13] Goebel, D. M., Hofer, R. R., Mikellides, I. G., Katz, I., Polk, J. E., and Dotson, B. N., “Conducting Wall Hall Thrusters,” *IEEE Transactions on Plasma Science*, vol. 43, Jan. 2015, pp. 118–126.

- [14] Gascon, N., Dudeck, M., and Barral, S., "Wall material effects in stationary plasma thrusters. I. Parametric studies of an SPT-100," *Physics of Plasmas*, vol. 10, Oct. 2003, pp. 4123–4136.
- [15] Grimaud, L., and Mazouffre, S., "Conducting wall Hall thrusters in magnetic shielding and standard configurations," *Journal of Applied Physics*, vol. 122, Jul. 2017, p. 033305.
- [16] Shastry, R., Huang, W., and Kamhawi, H., "Near-Surface Plasma Characterization of the 12.5-kW NASA TDU1 Hall Thruster," AIAA 2015-3919, 51st AIAA/SAE/ASEE Joint Propulsion Conference, July 23, 2015.
- [17] Sengupta, A., Brophy, J., and Goodfellow, K., "Status of the Extended Life Test of the Deep Space 1 Flight Spare Ion Engine After 30,000 Hours of Operation," AIAA 2003-4558, 39th AIAA/ASME/SAE/ASEE Joint Propulsion Conference and Exhibit, July 20, 2003.
- [18] Garner, C., Polk, J., Brophy, J., and Goodfellow, K., "Methods for cryopumping xenon," AIAA 96-3206, 32nd Joint Propulsion Conference and Exhibit, Buena Vista, FL, July 1, 1996.
- [19] Dankanich, J. W., Walker, M., Swiatek, M. W., and Yim, J. T., "Recommended Practice for Pressure Measurement and Calculation of Effective Pumping Speed in Electric Propulsion Testing," *Journal of Propulsion and Power*, vol. 33, Aug. 2016, pp. 668–680.
- [20] Chaplin, V. H., Conversano, R. W., Lobbia, R. B., Lopez-Ortega, A., Mikellides, I. G., Hofer, R. R., and Jorns, B. A., "Laser-Induced Fluorescence Measurements of the Acceleration Zone in the 12.5 kW HERMeS Hall Thruster," IEPC-2017-229, 35th International Electric Propulsion Conference, Atlanta, Georgia, October 8, 2017.
- [21] Nakamura, S., Miyafuji, D., Fujii, T., Matsui, T., and Fukuyama, H., "Low temperature transport properties of pyrolytic graphite sheet," *Cryogenics*, vol. 86, Sep. 2017, pp. 118–122.
- [22] Conversano, R. W., Hofer, R. R., Sekerak, M. J., Kamhawi, H., and Peterson, P. Y., "Performance Comparison of the 12.5 kW HERMeS Hall Thruster Technology Demonstration Units," AIAA 2016-4827, 52nd AIAA/SAE/ASEE Joint Propulsion Conference, Salt Lake City, UT, July 25, 2016.
- [23] Snyder, J., Goebel, D., Hofer, R., Polk, J., Wallace, N., and Simpson, H., "Performance Evaluation of the T6 Ion Engine," AIAA-2010-7114, 46th AIAA/ASME/SAE/ASEE Joint Propulsion Conference & Exhibit, Nashville, TN, July 25, 2010.
- [24] Hofer, R., "High-Specific Impulse Operation of the BPT-4000 Hall Thruster for NASA Science Missions," AIAA 2010-6623, 46th AIAA/ASME/SAE/ASEE Joint Propulsion Conference & Exhibit.
- [25] Polk, J. E., Pancotti, A., Haag, T., King, S., Walker, M., Blakely, J., and Ziemer, J., "Recommended Practice for Thrust Measurement in Electric Propulsion Testing," *Journal of Propulsion and Power*, vol. 33, Apr. 2017, pp. 539–555.
- [26] Sekerak, M. J., Hofer, R. R., Polk, J. E., Jorns, B. A., and Mikellides, I. G., "Wear Testing of a Magnetically Shielded Hall Thruster at 2000 s Specific Impulse," IEPC-2015-155, 34th International Electric Propulsion Conference, Kobe, Japan, July 6, 2015.
- [27] Snyder, J. S., Anderson, J. R., Noord, J. L. V., and Soulas, G. C., "Environmental Testing of NASA's Evolutionary Xenon Thruster Prototype Model 1 Reworked Ion Engine," *Journal of Propulsion and Power*, vol. 25, 2009, pp. 94–104.
- [28] Polk, J., Anderson, J., and Brophy, J., "Behavior of the thrust vector in the NSTAR ion thruster," AIAA-1998-3940, 34th AIAA/ASME/SAE/ASEE Joint Propulsion Conference and Exhibit, Cleveland, OH, July 13, 1998.
- [29] Lobbia, R. B., Conversano, R. W., Reilly, S., Hofer, R. R., and Sorensen, R., "Environmental Testing of the HERMeS TDU-2 Hall Thruster," AIAA-2018-4646, AIAA Joint Propulsion Conference, July 8, 2018.
- [30] Gilland, J. H., Williams, G., Burt, J. M., and Yim, J., "Carbon Back Sputter Modeling for Hall Thruster Testing," AIAA 2016-4941, 52nd AIAA/SAE/ASEE Joint Propulsion Conference, Salt Lake City, UT, July 25, 2016.
- [31] Lide, D. R., *CRC Handbook of Chemistry and Physics, 84th Edition*.
- [32] Garner, C. E., Polk, J. E., Pless, L. C., Goodfellow, K. D., and Brophy, John R., "Performance Evaluation and Life Testing of the SPT-100," International Electric Propulsion Conf., Paper IEPC-93-091, Seattle, WA, USA, September 1993.
- [33] Delgado, J. J., "Qualification of the SPT-140 for use on Western Spacecraft," AIAA 2014-3606, 50th AIAA/ASME/SAE/ASEE Joint Propulsion Conference, Cleveland, OH, July 28, 2014.
- [34] Grys, K. de, Mathers, A., Welander, B., and Khayms, V., "Demonstration of 10,400 Hours of Operation on 4.5 kW Qualification Model Hall Thruster," AIAA 2010-6698, 46th AIAA/ASME/SAE/ASEE Joint Propulsion Conference & Exhibit.
- [35] Peterson, P. Y., Kamhawi, H., Huang, W., Williams, G., Gilland, J. H., Yim, J., Hofer, R. R., and Herman, D. A., "NASA's HERMeS Hall Thruster Electrical Configuration Characterization," AIAA 2016-5027, 52nd AIAA/SAE/ASEE Joint Propulsion Conference, July 22, 2016.